Continental Water storage trends derived Storage Trends and Budgets from the GRACE/-FO global gravity-based groundwater product Global Gravity-based Groundwater Product (G3P)

Roland Hohensinn[a,e,*], Junyang Gou[b,c], Ulrich Meyer[d], Laura Jensen[e], Vincent Humphrey[f], Wouter Dorigo[g], Eva Boergens[e], Benedikt Soja[b], Alexander Gruber[g], Annette Eicker[e,i], Michael Rast[a], Andreas Güntner[e,h]

[a]*International Space Science Institute, Hallerstrasse 6, Bern, 3012, Switzerland*
[b]*Institute of Geodesy and Photogrammetry, ETH Zurich, Robert-Gnehm-Weg 15, Zurich, 8093, Switzerland*
[c]*Department of Earth, Atmospheric and Planetary Sciences, Massachusetts Institute of Technology, 77 Massachusetts Avenue, Cambridge, 02139, USA*
[d]*Astronomical Institute, University of Bern, Sidlerstrasse 5, Bern, 3012, Switzerland*
[e]*GFZ Helmholtz Centre for Geosciences, Telegrafenberg, Potsdam, 14473, Germany*
[f]*Federal Office of Meteorology and Climatology MeteoSwiss , Operation Center 1, Zürich-Flughafen, 8058, Switzerland*
[g]*Department of Geodesy and Geoinformation, TU Wien , Wiedner Hauptstrasse 8-10, Wien, 1040, Austria*
[h]*University of Potsdam, Institute of Environmental Science and Geography , Karl-Liebknecht-Strasse 24-25, Potsdam, 14476, Germany*
[i]*HafenCity University Henning-Voscherau-Platz 1, Hamburg, 20457, Germany*

Abstract

The Global Gravity-based Groundwater Product (G3P) provides observations of global groundwater storage (GWS) variations , calculated derived from GRACE/-FO-derived GRACE-FO terrestrial water storage (TWS) by subtracting the contributions of root zone change by subtracting root-zone soil moisture, glaciersglacier mass change, surface water storage, and snow water equivalent. As such, G3P thus provides the first globally consistent, publicly available groundwater dataset from satellite gravimetry for continental-scale trend assessment. Such data are a crucial observational constraint for assessing global groundwater depletion, recharge, and water storage trends related to climate change and human activitieswater resources assessment. Here, we use G3P to assess global GWS trends over the extended GRACE/GRACE-FO record, jointly with TWS and the subtracted storage components.

A challenge is the reliable separation and quantification of central challenge is that apparent long-term trends from stochastic signals attributable to in GRACE/GRACE-FO water storage records can reflect persistent storage change, natural climate variability("climate noise") and observational system errors. To address this , we introduce a , hydrological memory, and observational errors, complicating trend detection and continental-scale storage-change budgets. We address this using a calibrated trend-analysis framework that uses calibrated time-series models to account for trendsjointly accounts for trend, seasonal, and stochastic variations . The approach requires minimal assumptions about underlying processes and enables the separation of significant long-term trends of in each grid-cell time series. Statistically significant trends are then aggregated to quantify volumetric GWS and TWS from stochastic variabilitygains, losses, and net changes at continental and global scales.

Applying this framework to 21.5 years of data , our results show (1)(04/2002–09/2023), we find that groundwater depletion dominates is a major contributor to freshwater decline at continental scales– , most prominently in Asia (-55 km^3 yr^{-1})– whereas ice mass loss remains the largest global contributor by component, and (2) reveal previously unobserved trends, including -55 km^3 yr^{-1}), while cryospheric mass loss dominates the strongest TWS declines in high-latitude and glacierized regions. Pronounced regional contrasts include increasing groundwater storage in across large parts of Africa ($+37$ km^3 yr^{-1})and declining trends attributed to droughts, e.g., in Southern Africa, Asia, and parts of Europe. Our global

*Correspondence to: Roland Hohensinn (roland.hohensinn@gfz.de)

aggregation of statistically significant trends indicates net volumetric GWS changes of -27 km^3 yr^{-1} $+37$ km^3 yr^{-1}), negative trends in drought-affected regions, and widespread negative or near-threshold GWS tendencies across the Northern Hemisphere. Globally, significance-filtered net GWS and TWS changes of -145 km^3 yr^{-1} (excluding Antarctica and Greenland). We also find that many regions in the Northern Hemisphere are prone to climate-induced drying, with parts of Europe close to persistent long-term groundwater declineare approximately -27 and -183 km^3 yr^{-1}, respectively. The corresponding gross negative GWS change of approximately 103 km^3 yr^{-1} is of the same order as model-based estimates of global groundwater depletion. Sensitivity tests show robust results: at 95%, detected area increases by 30% for TWS and 36% for GWS, while net-loss magnitudes rise by only 9% and 18%. Across much of the seasonal-to-interannual spectral range, GWS is the dominant individual storage-component signal within TWS, underscoring the importance of groundwater for continental freshwater availability.

Keywords: GRACE/-FO hydrology GRACE-FO , Global Gravity-based Groundwater Product (G3P) , terrestrial water storage (TWS), groundwater storage (GWS), freshwater resources groundwater depletion , climate change water-storage budgets , hydrological signal decomposition water resources , trend analysis, stochastic modelling

1. Introduction

1.1. *Water storageas an* : An *Essential Climate Variable and its observation with* observed by *satellite gravimetry*

Quantifying trends in terrestrial water storage (TWS) is central for assessing changes in global freshwater availability and its coupling to the climate system (Rodell et al., 2018; Pokhrel et al., 2021; Huggins et al., 2022; Riva et al., 2010; Frederikse et al., 2020; Gou et al., 2025; Seo et al., 2025; Humphrey et al., 2023)(Rodell et al., 2018; Pokhrel et al., 2021). TWS integrates changes in groundwater storage (GWS), soil moisture, surface water, snow water equivalent, and glaciers(Tapley et al., 2019). To reflect their importance, TWS and GWS have been endorsed as Essential Climate Variables by the Global Climate Observing System (GCOS) (World Meteorological Organization, 2022).

Since 2002, the GRACE (2002–2017) and GRACE Follow-On (since 2018) missions provide global observations of time-variable mass change (Tapley et al., 2004; Landerer et al., 2020), yielding an almost continuous over-two-decade record that substantially improves trend detectability compared to earlier GRACE-only studies. Within the Global Gravity-based Groundwater Product (G3P), consistent global GWS estimates (v1.11–v1.12) are derived from GRACE/-FO TWS by subtracting filtered contributions of other storage compartments (Güntner et al., 2026). GRACE/-FO observations capture the combined effects of climate-driven ice and glacier climate variability, cryospheric mass loss, and anthropogenic water use(e.g., , including groundwater extraction for irrigation), and natural variability in precipitation and recharge (e.g., Rodell et al. 2018; Li and Rodell 2024)(e.g., Li and Rodell, 2024). For global trend assessment, GRACE/-FO observations are particularly valuable because hydrological and land-surface models can exhibit divergent trend signs and magnitudes, which complicates trend inference (e.g., soil moisture; Albergel et al. 2012), which complicates trend inference (Scanlon et al., 2018), Scanlon et al. 2018 or Albergel et al. 2012).

1.2. *Observed global and continental-scale patterns in TWS and GWS*

GRACE-based assessments reveal spatially heterogeneous TWS trends. For 2002–2016, global land water storage losses of approximately -154 ± 22 km^3/yr can be deduced from Rodell et al. 2018 (excluding Antarctica and Greenland), largely driven by ice mass loss 2002–2016, Rodell et al. (2018) quantified 34 major regional TWS trends and attributed them to natural interannual variability, unsustainable groundwater consumption, climate change, or combinations thereof. Their analysis highlighted strong cryospheric losses in North America . Continental patterns include strong negative trends in Asia (exceeding -50 km^3/yr) and

comparable magnitudes in North America, where cryospheric processes dominate (Rodell et al., 2018)as well as major drying regions in Asia and other continents. In contrast, Africa shows positive anomalies for Africa positive TWS tendencies in parts of the Sahel and East Africa are reported, attributed to precipitation variability and enhanced groundwater recharge – the so-called Sahelian Paradox (Werth et al., 2017; Springer et al., 2023; Boergens et al., 2024a)(Werth et al., 2017; Springer et al., 2023). South America exhibits moderate losses dominated by Patagonian glacier retreat, while strong variability driven by El Niño Southern Oscillation (ENSO) is a complicating factor for detection in the Amazon Basin (Tapley et al., 2019; Satizábal-Alarcón et al., 2024)(Satizábal-Alarcón et al., 2024). Regarding recent synthesis efforts, Chandanpurkar et al. 2025 reported a continental TWS loss (excluding Greenland and Antarctica) exceeding 300Chandanpurkar et al. (2025) report a global land TWS loss equivalent to 324 ± 55 km^3 yr^{-1} , representing (excluding Greenland and Antarctica), using a different spatial and methodological framework; this is one of the largest published global land TWS loss estimates to date.

GWS represents a critical and regionally heterogeneous component of TWS change. Global anthropogenic groundwater depletion has been estimated at approximately 100–150 km^3/yr during the early 21st century, with some model-based estimates reaching up to about 200 km^3/yr (Döll et al., 2014; de Graaf et al., 2017; Bierkens and Wada, 2019). However, regional groundwater gains partly offset these losses, resulting in substantially smaller net global groundwater storage declines. While groundwater represents roughly 15For 2002–25% of total 2014, Wada et al. 2017 partition global land water mass losseswhen ice-sheet contributions are included, it dominates TWS decline across storage change by process. Summing the loss terms in their budget – groundwater depletion, endorheic and wetland losses, and deforestation – groundwater accounts for about half of the total, making it the largest single loss term. In contrast, for the GRACE/GRACE-FO era, Chandanpurkar et al. (2025) report that groundwater depletion accounts for about 68% of TWS loss over non-glaciated continental regionsat a contribution of about 65% (Chandanpurkar et al., 2025). Large-scale syntheses analyses based on groundwater well observations confirm widespread groundwater decline, along with localized recovery resulting from policy interventions (Jasechko et al., 2024). Major depletion hotspots are the Indo-Gangetic Plain, North China Plain, and the Middle East (Rodell et al., 2009; ?; Joodaki et al., 2014; Gou and Soja, 2024)(Rodell et al., 2009; Feng et al., 2013; Joodaki et al., 2014), as well as the High Plains Aquifer and California's Central Valley in North America (Scanlon et al., 2012; Famiglietti et al., 2011). In Africa, positive GWS anomalies in parts of the Niger Basin and the East African Rift are in contrast to depletion in North African fossil aquifer systems, notably the North Western Sahara Aquifer System (NWSAS) and the Nubian Sandstone Aquifer System (NSAS)(Werth et al., 2017; Springer et al., 2023).

1.3. Physical drivers, attribution, and limits of interpretability

Attribution of TWS and GWS trends to climate-related versus and anthropogenic drivers is important, but a challengingtaskyet challenging. Cryospheric mass loss is the a dominant component of global TWS land-mass decline, with Greenland (∼–279±23 km^3/yr) and Antarctica (∼–128±40 km^3/yr), together with mountain glaciers, which drives an accelerated mass loss under climate warming (Rodell et al., 2018; Chen et al., 2006; Otosaka et al., 2023)and Antarctica losing approximately 169 ± 9 and 92 ± 18 Gt yr^{-1}, respectively, over 1992–2020, while glaciers outside the Greenland and Antarctic ice sheets lost approximately 199 ± 32 Gt yr^{-1} over 2002–2016 (Wouters et al., 2019; Otosaka et al., 2023). Outside glaciated regions, irrigation-driven groundwater extraction is the dominant contributor to negative trends, and is reported to exceed natural recharge by factors of 2–10 groundwater abstraction for irrigation is a major driver of persistent groundwater-storage decline in intensively managed aquifers. In many systems under stress, groundwater extraction exceeds renewable groundwater availability, which results in continued depletion of groundwater storage (Wada et al., 2012; Richey et al., 2015).

Climate variability is linked to large-scale modes such as ENSO, the North Atlantic Oscillation(NAO), and the Indian Ocean Dipole (IOD) and is known to modulate precipitation,

soil moisture, surface water, and groundwater recharge on interannual to decadal time scales (Anyah et al., 2018; Boergens et al., 2024b). Assessments indicate that, when integrating across storage compartments, climate forcing may exceed anthropogenic contributions to decadal land water storage change, although this is reported to strongly depend on the region (Scanlon et al., 2018). TWS trends also propagate into sea-level budgets and Earth-system mass closure, providing constraints on coupled hydrosphere–cryosphere processes (Riva et al., 2010; Frederikse et al., 2020; Gou et al., 2025; Seo et al., 2025)(Riva et al., 2010; Frederikse et al., 2020), however uncertainties across storage components remain substantial (Dorigo et al., 2021)and yet unsolved (e.g., Dorigo et al. 2021).

Hydrological memory is a limiting factor for trend interpretation: groundwater and glaciers integrate multi-year climate signals, whereas soil moisture and surface water respond more rapidly. These memory effects – often underrepresented in models – can generate long-period-transient-type apparent-secular trends apparent secular trends caused by long-period transient variability in records of limited duration (Lu et al., 2025; Humphrey and Gudmundsson, 2019; Vishwakarma et al., 2021). This (Humphrey and Gudmundsson, 2019; Vishwakarma et al., 2021). This provides a strong motivation for the use of statistical frameworks that explicitly account for persistence and stochastic variability (Franzke, 2012; Humphrey et al., 2017), as we present in this study.

1.4. Detectability limits and the role of natural variability and observational errors

GRACE/-FO trend magnitudes are typically small relative to seasonal and interannual variability, motivating additive decompositions into trends, periodic signals, and residual variability from climate and observational noise (Steffen et al., 2009; Humphrey et al., 2016; Scanlon et al., 2016)(Humphrey et al., 2016). Representative global studies combining such decompositions with trend-significance testing show that, although basin-scale trends are often within ± 20 mm/yr compared to seasonal amplitudes of up to ~ 250 mm, statistically significant trends are nevertheless widespread (Scanlon et al., 2016). The trend-to-variability ratio (TVR) further highlights that trend magnitude alone can misidentify water-stress hotspots when natural variability is large (Vishwakarma et al., 2021).

Persistent stochastic variability and long-range memory can inflate trend uncertainties and produce apparent trends over finite records (Mandelbrot and Wallis, 1969; Franzke, 2012; Mudelsee, 2010; Humphrey et al., 2017)(Mandelbrot and Wallis, 1969; Mudelsee, 2010; Humphrey et al., 2017). Long-memory behavior ("Hurst effect") motivates the use of parametric noise models such as ARFIMA or simpler processes, while short-term memory can be described by AR(1) processes (Koutsoyiannis, 2003; Franzke and O'Kane, 2017; Orth et al., 2013)models (Koutsoyiannis, 2003; Orth et al., 2013). Colored noise has been identified in GRACE-derived TWS time series, resulting in underestimated uncertainties if autocorrelation is ignored (Gunes and Aydin, 2024). Generalized least squares (GLS) approaches that explicitly model the covariance structure are therefore very well suited under the presence of stochastic memory (Mudelsee, 2019), while least-squares regression remains robust even under moderate departures from normal distribution properties (Knief and Forstmeier, 2021)departures from required distribution properties (e.g., Knief and Forstmeier 2021).

1.5. Research gap and study objectives

Accurate and reliable global trend inference and water storage change quantification The G3P dataset now enables a globally consistent assessment of GWS variations from satellite gravimetry. This opens the possibility to quantify not only regional groundwater trends, but also continental and global groundwater gains, losses, and net storage changes over the extended GRACE/GRACE-FO record.

However, reliable trend inference from GRACE/-FO remains challenging by the presence of persistence and long-range memory, which can yield underestimated uncertainties and false-positive detections when not modeled explicitly (Mandelbrot and Wallis, 1969; Franzke, 2012; Humphrey et al., 2017; Mudelsee, 2010). These limitations are critical for water-storage time series remains challenging. Monthly TWS and GWS records contain persistence, hydrological memory, and correlated observation errors. If this temporal dependence is not considered, trend uncertainties can be underestimated and apparent trends may be incorrectly classified as significant (Franzke, 2012; Humphrey et al., 2017; Mudelsee, 2010). This also limits detection and attribution (D&A) studiesaiming to separate studies, because internally generated water-storage variability can be difficult to separate from externally forced change from internal variability (Bindoff et al., 2014). While optimal fingerprinting is well established for temperature and precipitation (Hasselmann, 1997; Allen and Tett, 1999), its application to TWS and GWS is hindered by uncertainties in modeled storage variability remains difficult because modeled water-storage variability and individual storage components remain uncertain (Humphrey et al., 2017; Scanlon et al., 2018; Jensen et al., 2019).

Here, we introduce a statistically traceable trend-detection framework for Previous GRACE/-FO studies have provided important evidence for large-scale TWS change and regional groundwater depletion, e.g., well-studied groundwater and water-storage losses in California and other intensively managed or drought-affected regions (Thomas et al., 2017; Argus et al., 2022). Yet global groundwater trend assessments still differ strongly in data products, study periods, component separation, spatial masks, and uncertainty treatment. In particular, a globally consistent assessment of statistically significant GWS trends from GRACE and G3P, together with continental and global groundwater gain, loss, and net storage-change budgets, forms a core novelty.

Here, we address this gap by applying a calibrated time-series framework to 21.5 years of GRACE/-FO-derived water storage time series that explicitly accounts for short- and TWS and G3P-based GWS variations. The framework estimates trends and seasonal signals while accounting for short- and long-range memory using GLS with autocovariance modeling.Leveraging the G3P data , we provide a consistent, uncertainty-aware assessment , quantification and attribution of groundwater storage trends by temporal dependence in the residuals. This allows us to separate statistically significant long-term storage changes from stochastic variability and to aggregate significant grid-cell trends into volumetric storage-change budgets. By jointly analysing GWSand TWS, as well as its contributing , TWS, and the subtracted storage compartments – root-zone soil moisture, glacier mass, snow water equivalent, and surface water storage (Güntner et al., 2024). While for earlier GRACE studies trend interference and change quantification has often been limited due to the limited dataset lengths, we now can access 20+ years of GRACE/-FO time series data, and a globally available GRACE-derived GWS dataset. By applying the same framework to TWS and other storage time series, we demonstrate scalability to other essential climate variables (Bindoff et al., 2014)– we assess where groundwater dominates freshwater loss or gain, where other storage components control the TWS signal, and where interpretation remains uncertain.

Section 2 describes the G3P data products and the mathematic-statistical statistical trend detection framework. Section 3 analyses spatio-temporal and spectral characteristics of TWS and GWS datathe storage time series, and presents the principal results: statistically significant global and regional significant trends, attributes drivers, and quantifies volumetric groundwater trends, their interpretation based on the literature, and the resulting volumetric storage changes. Section 4 summarizes the added value main findings of this study and outlines future research. Supplementary sections, figures, tables, and equations are indicated by the prefix "S".

2. Data and Methods

2.1. G3P Data

For G3P, TWS is based on the level-2 spherical harmonics solution of the COST-G combination product (Jäggi et al., 2020; Meyer et al., 2024). For obtaining gridded, spherical-harmonics-

based time series of TWS and GWSvariations, the GFZ and G3P data processing workflow for the GRACE and GRACE-FO missions follows a hierarchical approachsequential processing chain. First, raw satellite observations are transformed into global gravity field solutions (level-0 to level-2), followed by the generation of gridded level-3 time series of TWS variations. Subsequently, the gridded level-4 GWS variations are generated using the other compartments' storage databy subtracting the storage variations of the other continental water-storage compartments. The gridded data products are publicly available at GFZ's data portal GravIS (Gravity Information Service, `https://gravis.gfz.de`)[1].

All necessary Detailed information explaining the processing and the generation of the G3P data product are is provided by Dahle et al. (2025) and Güntner et al. (2026). A more detailed explanation of level-0 to level-4 processing stages is also provided in Section S1 of the supplementary material to this paper. In the following, we highlight the most important aspects of level-4 processing, relevant to this study. GWS variations are derived from level-3 GRACE/GRACE-FO TWS anomalies using a water balance water-balance approach in which storage variations of other continental water compartments are subtracted from TWS(see, e.g., Frappart and Ramillien 2018 for an overview):

$$\mathrm{GWS} = \mathrm{TWS} - (\mathrm{RZSM} + \mathrm{SWE} + \mathrm{GM} + \mathrm{SWS}) \tag{1}$$

This approach is implemented in the G3P data product(Güntner et al., 2024, `https://www.g3p.eu/`), which we use in this study . For G3P, TWS is based on the level-2 spherical harmonics solution of the COST-G combination product (Jäggi et al., 2020; Meyer et al., 2024). The water storage (Güntner et al. 2024, `https://www.g3p.eu/`, see, e.g., Frappart and Ramillien 2018 for a general overview). The water-storage compartments subtracted to estimate G3P GWS variations are:

i) **Root-zone soil moisture (RZSM):** Derived from a multi-satellite surface soil moisture product of the Copernicus Climate Change Service (C3S) with spatial-temporal gap filling and an infiltration approach to 2 m soil depth (Pasik et al., 2023; Preimesberger et al., 2025).

ii) **Snow water equivalent (SWE):** Satellite-based data from the GlobSnow product (Luojus et al., 2021) combined with the Copernicus Global Land Service (CGLS) operational SWE product and extended to global coverage for G3P.

iii) **Glacier mass change (GM):** Based on global gridded data from C3S (Dussaillant et al., 2023), further developed for G3P to monthly resolution (Zemp and Welty, 2023).

iv) **Surface water storage (SWS):** Storage in lakes, rivers, wetlands, and reservoirs from the OS LISFLOOD hydrological model as implemented in the Global Flood Awareness System (GloFAS) of the Copernicus Emergency Management Service (Choulga et al., 2024; Van Der Knijff et al., 2010).

To ensure consistency with the effective spatial resolution of GRACE-derived TWS (approximately 300–500 km), all monthly compartmental storage time series are spatially smoothed with a Gaussian filter of 250 km filter width prior to subtraction (Sharifi et al., 2025). The filtered storage data are then subtracted from TWS to obtain time series GWS variations(anomalies w.r.t. reference period)GWS variations. All storage variables are treated as anomalies with respect to their temporal mean over the reference period. Measurement-type uncertainties are provided

[1]GravIS is an online data portal that provides access to gravity-field–related gravity-field-related data products, services, and visualizations derived from satellite gravimetry.

based on Merchant et al. (2017). For In this study, uncertainties are the stochastic uncertainty relevant for trend detection is calibrated from the data to optimally time series themselves to represent the combined effects of measurement noise and natural climate variability (cf. Section 2.2).

For each cell of the global grid, G3P delivers a time series of monthly water storage with units of equivalent water heightas anomalies with respect to the reference period. The G3P V.1v1.12 dataset (Güntner et al., 2024), which we use in this study, is provided on a $0.5° \times 0.5°$ latitude-longitude grid (nominal resolution), though although the effective resolution of GRACE/-FO observations is coarser (∼300–500km due to filtering; Dahle et al., 2025). Thus, to (∼300–500 km due to filtering; Dahle et al., 2025). To reduce computational load while preserving spatial coverage and important hydrological signals relative to the effective GRACE/-FO resolution, we downsampled the data by selecting every second grid cell, resulting in $1° \times 1°$ spacing. This yields 14,766 time series over the continents continental time series for each variable, ranging excluding Antarctica and Greenland. The analysed period ranges from April 2002 to September 2023 (except Antarctica and Greenland). With gaps, such as between end of GRACE and beginning of 2023. Because of missing monthly solutions, including the gap between the GRACE and GRACE-FO , we have – for each grid cell – a time series of monthly resolution with missions, each grid-cell time series contains 225 data pointsmonthly observations. Besides the focus variables TWS and GWS, we also processed the other compartmental storage variables. Certain compartments contain grid points with no contributions, as no effect is measurable in certain regions (e. g. , glaciers, or SWE near the equator).

Since GWS is derived residually, uncertainties, systematic errors, or missing signals in any of the subtracted storage compartments can propagate into the resulting GWS estimate. This is particularly relevant where local or human-managed water-storage changes are not fully represented by the component products. For example, irrigation-related surface wetting may only be partly captured in the RZSM product where it is detectable by satellite surface-soil-moisture observations and may be attenuated during root-zone propagation. Similarly, while human-managed surface-water processes, such as reservoir operation and regulated river or lake storage, are represented in SWS through the OS LISFLOOD/GloFAS model setup, their quality depends on the available model input and process simulation, which are certainly not perfect for all water bodies. Such effects may therefore alias into residual GWS estimates, especially in strongly irrigated or regulated basins. Regarding spatial resolution, a common problem of satellite gravimetry as realized by GRACE and GRACE-FO is the leakage effect (e.g., Dahle et al. 2025). Leakage describes the inability to localise localize signals in the GRACE-derived data sets exactly. The first One cause of leakage is signal attenuation due to the distance between the signal source on, or close to, the Earth's surface and the observing satellites. Further data processing steps towards TWS data, foremost filtering, are further reducing spatial filtering, further reduce the spatial resolution of TWS. Together, leakage leads to apparent signal loss (leakage out) or gain (leakage in) inside a given integration region. In our data analysis, we will refer to this when appropriateeffect where relevant for interpretation.

2.2. Methods

Each of the

2.2.1. Time Series Models

The time series method below is applied independently to each grid-cell time series: We estimate a linear trend and periodic signals, model the temporal correlation of the residuals, derive trend uncertainties from the calibrated stochastic model, and test whether the trend differs significantly from zero. The principal advantage of calibrating the stochastic model is a realistic assessment of trend uncertainty under temporal correlation. The corresponding GLS trend estimates may also differ from ordinary least squares (OLS) estimates when the residual covariance structure is taken into account (cf. Sect. S2.6).

Each G3P time series analyzed analysed is represented by $\mathbf{y}^T = [y(t_0), y(t_1), .., y(t_k), .., y(t_{n-1})]$, where the index $\mathbf{y}^T = [y(t_0), y(t_1), ..., y(t_k), ..., y(t_{n-1})]$, where $k = 0, 1, ..., n-1$ refers to the $k-$th of n samples in total, and t is the time (in days)indexes the monthly samples and t_k is time in days. Although GRACE/-FO monthly solutions are not exactly evenly spaced due to irregular mission operations (e.g., see `https://grace.jpl.nasa.gov/data/grace-months/`, last accessed January 20, 2026), we follow common practice and take on-average monthly sampling (use an average monthly sampling interval of $\Delta t = 30.4375$days) days, consistent with the average length of a Gregorian month. Observations refer are assigned to the middle of each month, and gaps are left as they are (e. g, GRACE to . Missing monthly solutions, including the gap between the GRACE and GRACE-FO). The following additive time series missions, are retained as missing epochs and are not interpolated. Trends estimated on the daily time axis in mm day^{-1} are converted to mm yr^{-1}.

For each grid cell, the following additive time-series model is consideredto explain each time series:

$$y(t_k) = a + b \cdot t_k + \sum_{j=1}^{m} (U_{j,1} \cos(2\pi f_j t_k) + U_{j,2} \sin(2\pi f_j t_k)) + z(t_k) \tag{2}$$

a and b are represent the intercept and slope of the linear trend function, $U_{j,1} = \bar{U}_j \cos(\varphi_j)$, $U_{j,2} = -\bar{U}_j \sin(\varphi_j)$. The periodic terms are described by $U_{j,1} = \bar{U}_j \cos(\varphi_j)$ and $U_{j,2} = -\bar{U}_j \sin(\varphi_j)$, with $\bar{U}_j$ and φ_j being denoting the amplitude and phase of a number of m constant-amplitude periodic signals (at given frequencies the j-th periodic signal at frequency f_j). Based on our pre-analysis of variables' power spectral densities (PSD) (Section3.1)the exploratory spectral analysis and spatio-temporal analysis in Section 3.1, we choose $m = 6$, comprising the annual periodic signal (365.25 days), and the first five harmonics. These parameters represent signal and its first five overtones (i.e. the second to sixth harmonics), with frequencies $f_j = j/365.25$ d^{-1} for $j = 1, \ldots, 6$. These terms define the functional model.

The residuals $z(t_k)$ are represented by the stochastic processes under consideration, and reflect contain remaining inter- and intra-annual geophysical signals (as "climate noise") and sensor noise, represented by a combination of autocorrelated (persistent) and uncorrelated processes. For each time series and each variable, with an individual fit of Eq. (2), we estimate the functional modelvariability, here referred to as "climate noise", as well as the stochastic processes as a combination of long/short-range memory and a white noiseprocess. The observation covariance matrix $\mathbf{C_{yy}}$ is considered to be a combination of two different models to represent the stochastic variability of the time series (e.g., Montillet and Bos, 2019): Based on the findings of a literature review and the explorative data analysis (Section 3.1)measurement and processing noise. We model these residuals as combinations of autocorrelated and uncorrelated stochastic processes. Motivated by the exploratory power spectral density (PSD) analysis in Section 3.1, we consider two different combinations of stochastic modelsstochastic model combinations (e.g., Montillet and Bos 2019):

$$\mathbf{C}_{\mathbf{yy}}^{(1)} = \sigma_{PL}^2 \cdot \mathbf{J}_{PL}(\kappa) + \sigma_{WN}^2 \cdot \mathbf{I} \tag{3}$$

$$\mathbf{C}_{\mathbf{yy}}^{(2)} = \sigma_{AR1}^2 \cdot \mathbf{J}_{AR1}(\phi) + \sigma_{WN}^2 \cdot \mathbf{I} \tag{4}$$

Here, σ^2 is denotes the variance component (amplitude) of the individual stochastic model, with its correlation structure represented by of each stochastic process, $\mathbf{J}$. The matrices in Eqs. (3) and (4) are of dimension the correlation matrix, and $\mathbf{I}$ the identity matrix (both of dimensions $n \times n$. The superscript $^{(1)}$ stands for the). The first model combines power-law plus white noise PL+WN (PLWN) model. Superscript $^{(2)}$ stands for the autoregressive process of order 1 plus white noise AR1+WN (AR1WN) model. $\mathbf{I}$ is the identity matrix. The PLWN model is central and represents noise with white noise and represents long-range memory processes, as observed in TWS and GWS from sustained precipitation or glacial melting, where variability persists over extended timescales. In contrast, the AR1WN model captures temporal dependence. The second combines first-order autoregressive noise with white noise and represents short-range memory processes, such as transient fluctuations in soil moisture or

surface water driven by precipitation. For both colored-noise processes, we added white noise to account for uncorrelated noise effects, such as high-frequency measurement noise. persistence. In both cases, the white-noise term accounts for uncorrelated measurement and processing noise.

The power-law correlation matrix $\mathbf{J}_{PL}$ depends on the spectral index κ(Bos et al., 2020), which represents, in a double-logarithmic plot, the linear slope characteristic to the PL PSD . At this stage, we recall that the random-walk (RW), the flicker-noise (FN), and the WN models , which describes the slope of the power-law PSD in log-log space. Random-walk, flicker, and white noise are special cases of the PL model: κ = -2 is RW noise, κ = -1 is FN, and $\kappa = 0$ represents white noise. AR1 represents the autoregressive model of order power-law model, with $\kappa = -2$, $\kappa = -1$, and $\kappa = 0$, respectively. The AR(1(e.g., Klos et al., 2018), and) correlation matrix $\mathbf{J}_{AR1}$ depends on the lag-1 coefficient ϕ , and flattens out in the spectral domain for long periods (less correlation)and represents short-range temporal correlation.

We exemplarily illustrate the different stochastic processes and noise types in Figure1, left panel 1. These synthetic time series are sampled in a GRACE-like , with 225 samples and gaps as-is. manner. All process realizations were drawn from the same normally distributed white driving noise. The corresponding PSDs (Figure 1, right panel), show that the processes reflect different correlation structures and strengths, particularly at low frequencies. The FN and RW noise realizations exhibit ever-increasing Flicker-noise and random-walk realizations exhibit increasing power at low frequencies, which strongly impacts inflates the estimated trend uncertaintiestowards inflation. These effects diminish are weaker for short-range memory models , such as AR1. The white noise PSD such as AR(1). White noise has constant power along all frequencies and thus shows no correlations, which results in much lower trend uncertainty and, thus, narrower confidence intervals (too optimistic under the presence of colored noise , see, e.g., Mudelsee 2019). The higher the magnitudes in the long periods (low frequencies), the stronger the temporal correlation , and the higher the uncertaintyof the estimated trends isacross frequencies and no temporal correlation, which would lead to overly narrow confidence intervals if coloured noise is present (e.g., Mudelsee, 2019). In general, stronger low-frequency power indicates stronger temporal correlation and larger trend uncertainty.

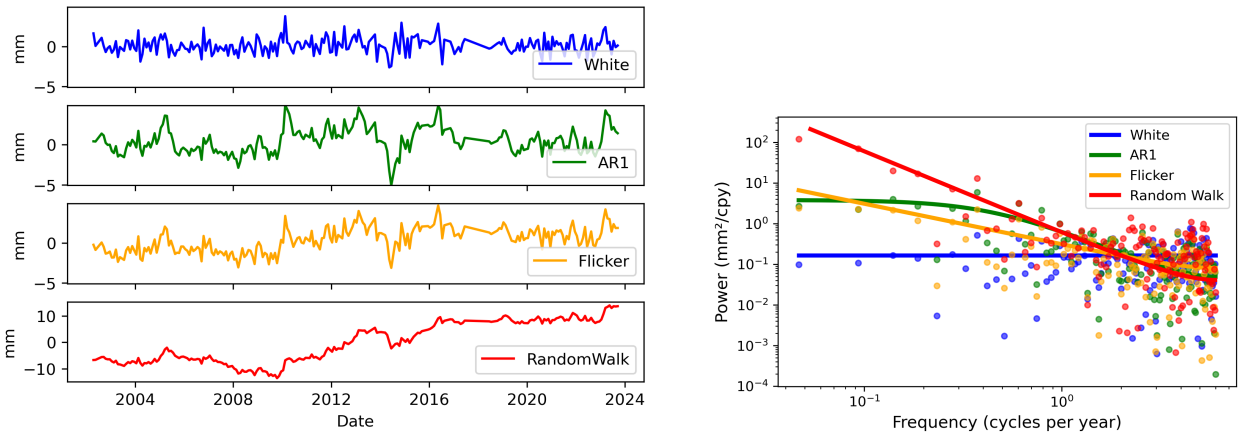


Figure 1: Left panel: synthetic Synthetic GRACE-like time series and corresponding power spectral densities (PSDs) for the stochastic processes under considerationconsidered in this study. Left: synthetic realizations of white noise, AR1 AR(1) noise, flicker noise, and random walk random-walk noise(; note : the different y axis limits y-axis scale for the random walk) (left panel)random-walk noise. Rightpanel: power spectral densities empirical PSD (PSDsdots) for and analytical PSD (lines) of the stochastic processes time series shown in the left panel.Dots represent empirical power spectral densities.

We use the Hector software (Bos et al., 2008, 2021) to estimate the individual parameters of the functional model (Eq.functional parameters of Eq. (2) and the respective stochastic model choice (Eq. 3 or 4), for each time series of the grid. The model of Eq. 2 is linear and the parameter vector is defined by $\mathbf{x} = [a,\ b,\ \bar{U}_1 \cos(\varphi_1),\ -\bar{U}_1 \sin(\varphi_1), \ldots,\ \bar{U}_j \cos(\varphi_2),$ we estimate the parameters using GLS, and the parameters of the stochastic processes are estimated using variance component estimation (e.g., Bos et al. 2020)parameters of the selected stochastic model for each grid-cell time se-

ries. The variance components for each model and the unknown parameters of the $\mathbf{J}_i$ matrices (Eqs. (3) and (4)) and stochastic-model parameters are estimated from the residuals of the parametric fit of Eq. (2) using Restricted Maximum Likelihood Estimation (RMLE) using restricted maximum likelihood estimation (Patterson and Thompson, 1971), which has, compared to conventional MLE, the ability to provide more realistic variance component estimates since it accounts for the loss of variance by the parameter fit (e.g., Gobron et al. 2022; Hohensinn et al. 2024). The degrees of freedom due to the fitted functional model (e.g., Gobron et al., 2022). The stochastic-model parameters include the spectral indices and coefficients of the PL and AR1 models. The result, for each time series of the global grid, we estimate the 14 parameters in $\hat{\mathbf{x}}$, and the corresponding covariance matrix components $\mathbf{C}_{\hat{\mathbf{x}}\hat{\mathbf{x}}}$index of the power-law model or the lag-1 coefficient of the AR(1) model. For each grid-cell time series, main quantities are estimated trend $\hat{b}$ and its uncertainty, represented by the standard deviation $\sigma_{\hat{b}}$, which are used for the significance test and volumetric aggregation.

We use the following statistical

2.2.2. Significance Testing

We apply the significance test under the assumption of normally distributedresiduals and parameters, and a two-sided confidence interval of 99%. We chose 99% to derive conservative change rates, under limited effect of false positivesthat the estimated trend is approximately normally distributed. Residual-distribution diagnostics for TWS and GWS, combined over all grid cells, are provided in Fig. S3. To test if whether the estimated trend $\hat{b}$ from each TWS and GWS time series is significant, we define the null and alternative hypothesis by hypotheses as

$$H_0: \quad \mathrm{E}(\hat{b}) = 0 \tag{5}$$

$$H_A: \quad \mathrm{E}(\hat{b}) \neq 0. \tag{6}$$

For each time series and each variable, the test quantity can then be formed by is then formed as (Amiri-Simkooei et al., 2019; Hohensinn et al., 2024)

$$T_b = \hat{b}/\sigma_{\hat{b}}, \tag{7}$$

where $\sigma_{\hat{b}}$ is the 1-sigma standard deviation , reflecting the trend uncertainty, estimated through the parameter adjustment by $\sigma_{\hat{b}} = \sqrt{\mathbf{C}_{\hat{b}\hat{b}}}$, taken from the diagonal of $\mathbf{C}_{\hat{\mathbf{x}}\hat{\mathbf{x}}}$, which reflects the parameter variances. We use a of the estimated trend, obtained from the corresponding diagonal element of the parameter covariance matrix $\mathbf{C}_{\hat{\mathbf{x}}\hat{\mathbf{x}}}$. Our main results rely on two-sided confidence interval of 99% , which confidence levels to reduce false-positive trend detections in the global grid-cell analysis. This results in a threshold T_b=2.58significance threshold of $|T_b| = 2.58$.

2.2.3. Clustering and Volumetric Aggregation

For our explorative data the exploratory spatio-temporal analysis in Section 3.1, we further apply K-means clustering. K-means clustering is an unsupervised machine learning machine-learning algorithm that partitions data into a predefined number of clusters by minimizing within-cluster variance. Applied to a time-series-populated feature matrix, it iteratively assigns the each time series to the nearest cluster . It was introduced by MacQueen (1967) to develop a simple and efficient method for partitioning multivariate data into homogeneous groups. (MacQueen, 1967). For the first application, the clustering is used to globally identify dominant TWS and GWS time series patterns. From this result we also use a GWS clustering class as an input for the illustration of significant and non-significant GWS time series. Therefore, we subsequently use another clustering to highlight differences between significant and non-significant time series classes, lying in adjacent regions. The clustering is not used for trend-significance testing or physical attribution.

To reliably quantify volumetric changes, the tables of continental water storage trends (TWS and GWS) in Section 3.2 were derived from G3P grid-cell time seriesand exhibit *statistically significant* trends only, which differs from earlier approaches. Each

significant trend of a grid cell is assigned to a continent, and its surface area is computed geodetically (area-aware weighting). Continental water storage changes are computed by direct physical integration of Significant grid-cell trends are converted to volumetric rates and aggregated into continental and global gain, loss, and net storage-change budgets, as explained in the following: Input are the estimated grid-cell trends and trend uncertainties on the downsampled 1° integration grid. Grid centres are assigned to continents using the Natural Earth Admin-0 Countries 1:110m shapefile (`ne_110m_admin_0_countries.shp`). Grid centres not covered by a country polygon are assigned to the nearest valid land-country polygon; grid-cell areas are computed separately and geodetically on the WGS84 ellipsoid. All non-Russian country-to-continent assignments follow the Natural Earth `CONTINENT` attribute. For Russia, grid cells west of 60°E are assigned to Europe and those at or east of 60°E to Asia. A grid cell is classified as significant when $|\hat{b}|/\sigma_{\hat{b}} \geq 2.58$, corresponding to the two-sided 99% confidence level used above. Only statistically significant grid-cell trends over continental areas, where b_i denotes the grid-cell trend (are included in the significant-trend budgets. Greenland and Antarctica are excluded from both TWS and GWS aggregation. The defined Canadian Arctic Archipelago mask, detailed in Section S1.1, is additionally excluded from the GWS aggregation because residual GWS signals there are especially sensitive to cryospheric leakage and GIA uncertainty; the same cells are retained in the TWS aggregation, where cryospheric mass change is physically part of TWS. For comparison, we additionally compute all-cell aggregates from all retained grid cells with finite trend estimates, without significance filtering, and assess GWS-to-TWS ratios under treatment of the Canadian Arctic Archipelago mask (Sect. S1.1).

Grid-cell trends in $\mathrm{mm\,yr^{-1}}$ equivalent water height) are converted to volumetric rates by multiplying with the corresponding grid-cell area:

$$\Delta V = \sum_i A_i \cdot \hat{b}_i \cdot 10^{-6}, \tag{8}$$

where $\hat{b}_i$ denotes the estimated grid-cell trend and A_i the corresponding grid-cell area (in $\mathrm{km^2}$). The factor 10^{-6} converts $\mathrm{mm\,km^2}$ to $\mathrm{km^3}$, yielding volume change rates in $\mathrm{km^3\,yr^{-1}}$ $\mathrm{mm\,km^2}$ to $\mathrm{km^3}$, yielding volume-change rates in $\mathrm{km^3\,yr^{-1}}$, numerically equivalent to $\mathrm{Gt\,yr^{-1}}$ $\mathrm{Gt\,yr^{-1}}$ for freshwater. This approach preserves physical additivity and mass conservation, and allows separation of positive (gain) and negative (loss) contributions , whose

Positive and negative significant grid-cell contributions are summed separately to obtain gross gains and gross losses; their algebraic sum defines the net balance. At the global level, global mean trends (storage-change rate. Continental values are obtained by aggregating the significant grid-cell contributions within each continent. Global gain, loss, and net storage-change rates are obtained by summing the corresponding continental contributions. Global mean trends in $\mathrm{mm\,yr^{-1}}$) are reported as significant-area-weighted averages of continental values, while global volume changes are then obtained by summing continental volume contributionsmeans. The procedure is described in more detail in Section S2S1.1.

3. Results

We first use exploratory spatio-temporal and spectral analyses to characterize the dominant variability patterns in the G3P storage time series (Sect. 3.1). We then present the core results, statistically significant TWS and GWS trends and their regional interpretation (Sect. 3.2), followed by the continental and global storage-change budgets and the 95% threshold assessment (Sect. 3.3). We conclude this part with a discussion on trend significance, model validation and regression sensitivity (Sect. 3.4).

3.1. Analysis of Spatio-Temporal and Spectral Data Features

3.1. Exploratory Analysis: Spatio-Temporal and Spectral Data Features

3.1.1. Time Domain Analysis

3.1.1. Time-domain Clustering

We first explore the spatio-temporal characteristics of TWS and GWS with respect to their trends and patterns at the global scale.Figure **??**a shows dominant properties of the G3P TWS data, obtained from the

We first use K-means clustering , with the time series dataas features, and by using 6 clusters. This grouping is solely as an exploratory tool to summarize dominant time-series patterns present in the G3P data, and to motivate the choice of the models presented in the previous section. Clustering is based on the structural similarity of the time series, temporal structure of the grid-cell time series and does not yet include any information on trend estimates or their significance . A visual inspection reveals that globally most areas (covering large parts of North America, Asia, Africa, and Oceania) do not show long-term trends (cluster 0, purple, top-left time series), but are dominated by seasonalvariations and interannual signals. Second to this, the blue cluster shows more pronounced seasonal variations, but also slightly negative trends (cluster 1, blue, top-middle time series), covering large regions of Western, Central, and South-Eastern Europe, the southwest of Asia and North America. This group also covers areas with considerable groundwater depletion due to agricultural activities (High Plains Aquifers and Central Valley in California, the Arab and Persian region, and North and East China). Regarding cluster 2 (turquoise, top-right time series), we observe further pronounced seasonal variations, but no strong trends, with regions located around the Tropical zone (e.g., West African Sudanian zone, northern South America, Central America, Central and South India). The strongest seasonal variations can be found in the Amazon Basin and the Zambesi in cluster 3 (green, bottom-left time series). Pronounced negative TWS trends as seen in cluster 4 (orange, middle-left time series) arise from surface water decline (Caspian Sea), groundwater depletion in northern India and around glacier and ice melting hotspots (e.g., Patagonia ice fields, the Canadian Arctic), while the hotspots of global TWS decline are the melting glaciers in the Gulf of Alaska and in the northern parts of Canadian Arctic Archipelago shown in cluster 5 (red, bottom-right time series panel).

use the subsequently estimated trend magnitudes, uncertainties, or significance information. Clusters should not be interpreted as hydrological process classes, but as groups of regions with similar temporal behaviour.

The corresponding TWS clustering mainly separates background seasonal/interannual variability, tropical seasonal regimes with different phase and amplitude, moderate depletion-like behaviour, and strong cryosphere-dominated mass loss. The full TWS clustering result is shown and discussed in Section S2.1.

Overview on global trends in terrestrial water storage (TWS, panel a) and groundwater storage (GWS, panel b) variations, as seen from the G3P data. Grouping of similar time series using K-means clustering. The time series of the individual clusters are shown in six panels below the map using color-coded cluster IDs. The black curve represents the mean time series for each cluster. Units in millimeters of equivalent water height.

Figure**??**b shows important spatio-temporal features of the Figure 2 shows the exploratory clustering of GWS time series. Compared with TWS, GWS seasonality is generally less pronounced because root-zone soil moisture is removed in the G3P GWS data. Again, seasonal and interannual variations dominate most of the time series (clusters 0 and 1, purple and blue, top-left groundwater estimate. Most regions are characterized by background GWS variability or high-latitude seasonal/interannual variability (purple and blue clusters). Moderate GWS drying occurs mainly across mid-latitudes, including large parts of North America and Eastern Europe, and top-middle time series), especially in the Northern hemisphere at high latitudes (blue cluster, top middle panel). The strongest seasonal variations are found in the center of the Amazon Basin, represented by cluster 5 (red, bottom-right time series), with peak-to-peak amplitude variations in equivalent water height of about 1000 millimeters. However, for GWS seasonal variations are less pronounced than for TWS because for the latter, RZSM is the dominant driver of seasonality. As a consequence, we can observe more subtle GWS trends: the turquoise cluster (cluster 2, top right)represents regions with moderate negtive GWS trends, covering large areas of Canada, the western and Southwestern U.S., central and eastern Europeextends into Central and Southern Asia, as well as, to a lesser extent, South America(Brazil), and several regions in Asia (including Arab Asia). The most pronounced negative GWS trends

are found in the Canadian Arctic and Northern India (cluster4, orange, bottom-middle time series panel). While the Indian GWS decline can clearly be attributed to groundwater pumping, the Arctic decline is questionable as it may be attributed to spurious leakage from Greenland ice mass loss , and potential modelling artefacts(see discussion further below). Several regions are characterized by positive GWS trends (cluster 3, green, bottom-left panel), e.g., around , Southern Africa, and Oceania. The strongest negative behaviour is grouped in the strong GWS decline / cryosphere-adjacent cluster, including northern India and parts of the Canadian Arctic. The northern Indian pattern is consistent with known groundwater depletion from intensive groundwater use, whereas high-latitude signals near the Canadian Arctic require cautious interpretation because they may include leakage from nearby cryospheric mass loss or component-separation artefacts. Positive GWS tendencies occur in parts of Central Africa, South America, the U.S. Midwest and Great Lakes region, parts of Southern America (e.g., Upper La Plata Basin), Russia, Central ChinaRussia, and most clearly large parts of Central Africa. We further discuss the detectability and significance of trends in Section and Central China. The Amazon high-amplitude seasonality cluster remains distinct, reflecting large seasonal groundwater-storage variations.

Overall, the clustering reveals distinct GWS variability regimes, ranging from widespread background and seasonal/interannual variability to broad mid-latitude drying, localized strong depletion, and regional storage gains, while high-latitude residual signals require cautious interpretation. Formal detection, uncertainty assessment, and volumetric quantification of trends are based on the grid-cell trend and budget analysis presented in Sect. 3.2.

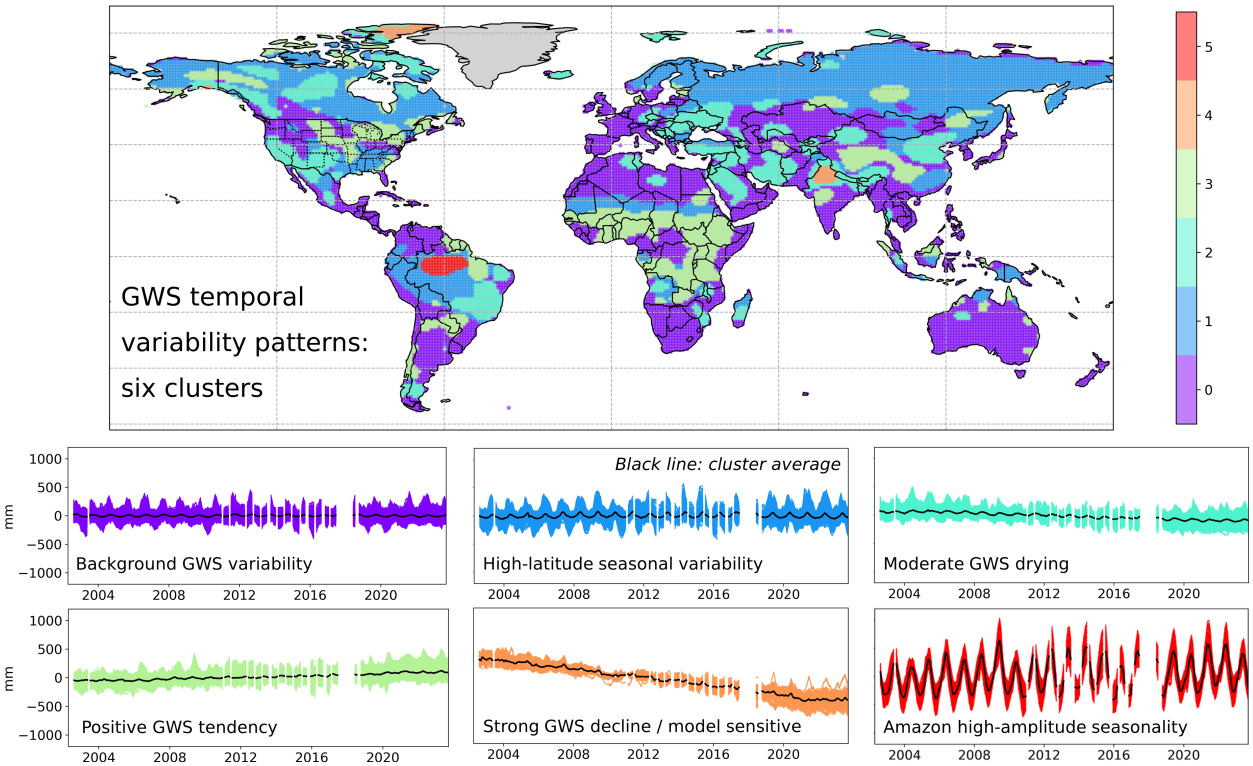


Figure 2: Exploratory K-means clustering of groundwater storage (GWS) time-series from the G3P data. The map shows the spatial distribution of six clusters, and the sub-panels show the corresponding cluster time series with descriptive cluster names. The black line represents the cluster-mean time series. Units are millimetres of equivalent water height.

3.1.2. Spectral Analysis

To assess data characteristics in the spectral domain and to identify stochastic processesmotivate the stochastic models used for trend uncertainty estimation, we compute Lomb-Scargle periodograms for all time series and for each storage compartment. The resulting globally averaged PSDs(per-frequency) , averaged per frequency, are shown in Figure Fig. 3, left panel. We

observe significant pronounced peaks at the annual and semi-annual periodperiods, indicating the substantial contribution of seasons seasonal variability to water storage variations. Furthermore, peaks are , particularly of RZSM and SWS to contribute to TWS. Further peaks occur at 3 and 4 cycles per year (cpy), i.e., at 4 to 3 month corresponding to 4- to 3-month intervals, and additionally at 5 and 6cpy (compartment variables) cpy for some compartment variables, i.e. , every 2nd approximately every second month. When comparing to compared with the synthetic examples presented in Figure Fig. 1, all variables show the presence of pronounced contributions of colored (correlated) noise (both of long coloured, i.e. correlated, noise of both long- and short-range type), following clear tendencies towards . This is indicated by higher PSD magnitudes at low frequencies(long periods) and towards , i.e. long periods, and lower magnitudes at high frequencies(short periods). Note that , i.e. short periods. The presence of trends still slightly affects the PSDs at long periods.

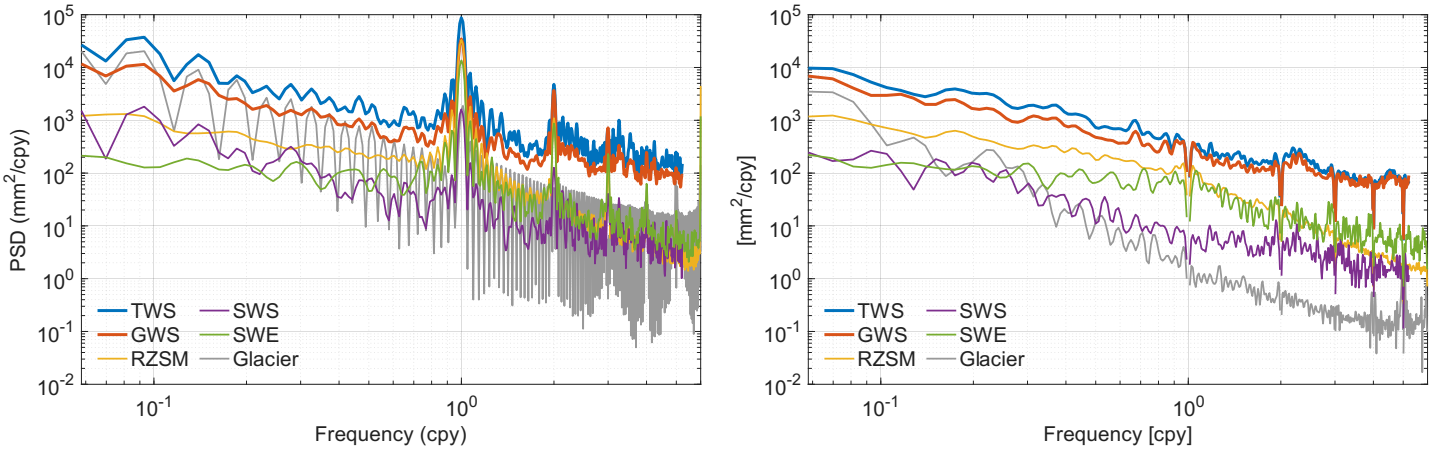


Figure 3: Averaged global power spectral densities (PSDs) of the G3P variables(left) and . Left: PSDs of the same variables original time series. Right: PSDs after removal of linear trend and periodic terms by ordinary least squares (OLS) (least-squares regression. TWS: Terrestrial Water Storage, terrestrial water storage; GWS: Ground Water Storage, groundwater storage; RZSM: Root Zone Soil Moisture, root-zone soil moisture; SWS: Surface Water Storage, surface water storage; SWE: Snow Water Equivalent, Glaciers)snow water equivalent; glaciers: glacier mass.

To better assess this influence the influence of trends and seasonal signals, and to reveal the stochastic character of the data, we remove identified periodic seasonal signals (1-6 1–6 cpy) and a linear trend using ordinary least squares (OLS) OLS regression. The resulting PSDs of the residuals (Figure Fig. 3, right panel) mostly reflect interannual variations and measurement system inter and intraannual variations and observation-system noise. For TWS, GWS, SWS, and glaciersglacier mass, we observe spectra close to constant negative slopes (in log-log space, indicating power-law behavior), indicating behaviour and long-range dependence. Broad interannual (~2–7 yr) power in TWS and GWS variations, approximately over 2–7 yr periods, is largely explained by superposed climate modes: combinations of ENSO-/, PDO-/, and AMO-related effects account for up 20% to 70% of interannual TWS variability in global basins, with interannual amplitudes of ~10 cm equivalent water height (Pfeffer et al., 2022). The observed power-law spectra of GWS reflect are consistent with long-memory GWS dynamicsas confirmed by groundwater dynamics, as also found in multi-decadal groundwater level records which exhibit fractal(groundwater-level records that exhibit fractal, power-law) scaling and long-range persistence (Li and Zhang, 2007; Little and Bloomfield, 2010)(Li and Zhang, 2007; Little and Bloomfield, 2010).

The spectra of SWE and RZSM tend to flatten out at long periods, indicating AR1-type (AR(1)-type, i.e. short-range memory) , behaviour. RZSM residuals are well described by AR1-type AR(1)-type exponential memory, with slightly stronger persistence in drier regimes (Orth and Seneviratne, 2012). SWE anomalies exhibit strong within-season persistence, consistent with short-range memory behavior behaviour (Sospedra-Alfonso et al., 2016), which

is also identifyable identifiable from our SWE spectrum, following a correlation structure of an AR1 process. In contrast, PSDs of glacier mass and SWS variations also indicate power-law behaviour. In line with SWS variations, long-range Long-range dependence with power-law behaviour was also has also been shown for global river runoff (Koscielny-Bunde et al., 2006), as it also relates to which is consistent with the influence of storage components with longer memory, such as groundwater and glaciers. Glacier mass anomalies can show power-law behaviour over the analysis band(e.g., 0.05–0.5 cpy) analysed frequency band, because multiple slow response times make glaciers a multi-timescale low-pass system . "A glacier can be thought of as acting as a low-pass spectral filter characterized by a red-noise-type power spectrum" (Roe, 2011), i.e., with stronger low-frequency correlation than an AR1 but still finite memory on very long timescales(Roe, 2011).

Remaining side lobes in the residual PSDs can be attributed to signals with indicate that a fixed set of sinusoidal terms does not fully capture time-variable amplitude. Furthermore, periods of seasonal variations are not exactly the same each year, and this variability could also introduce leakage-type behaviour, i.e., the broadened side lobes for RZSM, SWE, and also GWS around 1 cpy. Residual inter-harmonic power in GRACE/GRACE-FO TWS/GWS (e.g., 2-3 and 3-4 cpy) arises from cyclostationary seasonal amplitude and phasemodulation – this mechanism has been explained in GRACE TWS through spectral characteristics of cyclostationary signals, where amplitude modulation of the annual cycle creates detectable sideband energy (Hamlington et al., 2019; Chandanpurkar et al., 2021). ENSO-driven interannual variability can also cause frequency modulation that affects these sidebands (Cheon et al., 2021). In addition, seasonal variability is not universally well represented by a small set of sinusoidal harmonics: in regions such as monsoon-dominated India, strongly asymmetric recharge–discharge cyclesproduce sawtooth-like seasonal signals, while parts of central Africa exhibit . Such residual spectral structures are expected for hydrological time series with seasonally modulated storage dynamics, resulting from asymmetric recharge–discharge cycles, secondary seasonal peaks, both of which introduce higher-harmonic and inter-harmonic spectral power that cannot be fully captured by harmonic models. However, remaining effects can be considered to have little effect on the trend determinationonly, and are largely captured by data gaps. They are particularly visible around the annual and semi-annual periods and in the 2–4 cpy band. As predominantly the intra-annual band is affected, their remaining effect on trend determination, particularly on uncertainty, is expected to be limited and is partially accounted for through the stochastic model calibration. In data records with gaps, spectral leakage further broadens lobes in these sidebands (Thomson, 1982). These patterns in TWS variability were identified as key targets for future satellite gravity missions (Jensen et al., 2020). From about 3-4 cycles-per-year (cpy) onwards, a white noise type contribution to the variables is seen, being identifiable as a flattening of the spectra.

A further inspection of globally averaged A more detailed discussion of the component-wise spectral behaviour, including representative GWS and RZSM PSDs before and after removal of trends and seasonal components shows that periodic and trend terms, is provided in Sect. S2.2.

Our exploratory spectral analysis yields three key findings:

- *Trend-related low-frequency power:* Differences between the PSDs of the original time series and the post-fit residuals show that trend-related low-frequency power is strongly influenced by trends in glaciers and , to a smaller extent, in SWSand TWSstrongest for glacier mass and is also evident for TWS, SWS, and GWS, whereas RZSM and SWE exhibit comparatively weak trend contributions. After detrending and de-seasonalization, the residual spectra reveal distinct stochastic characteristics across compartments, with long-memory behavior dominating TWS, GWS , SWS, and glacier mass, and short-range persistence prevailing in RZSM and SWE. Representative PSDs of GWS and RZSM (cf. Figure S1 in Section S3.1) further highlight this contrast, with RZSM dominated by seasonal to interannual variability (as dominant seasonal contributor) and GWS showing stronger low-frequency trend influence, as it is also inferred from the clustering time-domain analysis. While low-frequency power associated with trends is strongest in glaciers, SWS, and TWS , the interannual band lower than 1 cpy is largely dominated by GWS contributions to TWS (followed by RZSM), except

- *Frequency-dependent component dominance:* Across most of the analysed frequency range, GWS exhibits the largest spectral amplitudes among the individual storage components and

therefore constitutes the dominant storage-component signal within TWS. Because GWS is obtained residually, these amplitudes may also include TWS observation errors and variability not represented in the subtracted components. Glacier mass dominates only at the very lowest frequencieswhere glacier signals prevail, and GWS remains the dominant contributor to TWS across most of the spectrum. In addition, the residual spectra reveal structured seasonal and cyclostationary behavior, particularly in GWS, with distinct spectral signatures persisting in the 2–4 cpy band after trend and periodic removal. More details of the spectral analyses are provided in Section S3.1.

3.1.3. *Summary of Time- and Spectral-Domain Analysis*

The time-domain clustering identifies spatially highly coherent regions of groundwater depletion and glacial mass loss (e.g., North America, India, Arctic regions), as well as emerging positive groundwater trends across parts of Africa and mid-latitude aquifers. TWS variations show high amplitudes of seasonal variations, which is less emphasized for GWS spectral characteristics, which are dominated by seasonal and interannual variability with pronounced low-frequency power. The literature-review-based analysis also underpins the advanced quality of G3P COST-G solutions, characterized by high signal-to-noise ratios and stable noise characteristics (Meyer et al., 2024)Among the modelled non-groundwater components, RZSM has the largest spectral amplitudes across much of the seasonal-to-interannual frequency range.

Our spectral pre-analysis yields two key findings:

- *Low-frequency behavior* Variability *and memory structure*regimes*:* Globally averaged PSDs show that TWS low-frequency power is primarily controlled by trends (glaciers, SWS) and interannual effects (mostly driven by GWS variations), whereas RZSM and SWE exhibit comparatively weak trend contributions. Residual The residual spectra indicate long-memory behavior behaviour for TWS, GWS, SWS, and Glacierglacier mass, and short-range persistence for RZSM and SWE.

- *Contrasting variability regimes:* Representative PSDs The detailed comparison of GWS and RZSM (Figure S1) highlight distinct variability regimes, with RZSM Sect. S2.2) further shows that RZSM is dominated by seasonal fluctuations and GWS showing a pronounced reduction of low-frequency power after detrending and strong long-memory persistence, which indicates sustained groundwater dynamicsvariability, whereas GWS exhibits a pronounced persistent inter-annual variability after removal of the functional signals.

Based on this pre-analysis, we select PLWN these spectral characteristics, we use power-law-plus-white-noise models for TWS, GWS, SWS, and Glacier, and AR1WN glacier mass, and first-order-autoregressive-plus-white-noise models for RZSM and SWE regarding our trend quantificationwhen estimating trend uncertainties.

3.2. *Global Trends in TWS and GWS, and their Significance*

Significant G3P TWS (panel a) and GWS trends (panel b) under consideration of the calibrated time series models introduced in Section 2, and the statistical test. Shading with "X" represents data with insignificant trends, while all non-shaded trends represent statistically significant trends.

As explained in Section 2, we fit trends (alongside the other parameters) and trend uncertainties to each TWS and GWS grid-cell time series. For the stochastic component, we use PLWN power-law-white-noise models as identified in Section 3.1. Figure 4 represents the core results: Along with the estimated trends, Figure 4 it highlights the significant trends at the 99% confidence level in TWS (top) and GWS (bottom), and represents our main results; trends in . Trends in the other G3P storage components (glacier mass, RZSM, SWS, SWE) are shown in Figure 5, for which also the identified stochastic processes have been fitted. Maps of estimated trends without shading TWS and GWS trends without significance-shading can be found in Figures S3 and S4 and S5,

Sect. S2.4. The same figures , as well as Figure S5, also discuss stochastic properties and trend distributions (power-law coefficients and trend uncertainties) of the TWS and GWS data.

Normality diagnostics are carried out , which further support the choice of our models. Figure S6 compares histograms of the parameters shown in Figs. S4 and S5, for TWS and GWS(Figure S2), which constitute the primary targets of trend analysis in this study.This normality check is performed to show the reliability of our trends and trend uncertainties estimated from these data, when using the GLS estimator under serial autocorrelation. [2] .

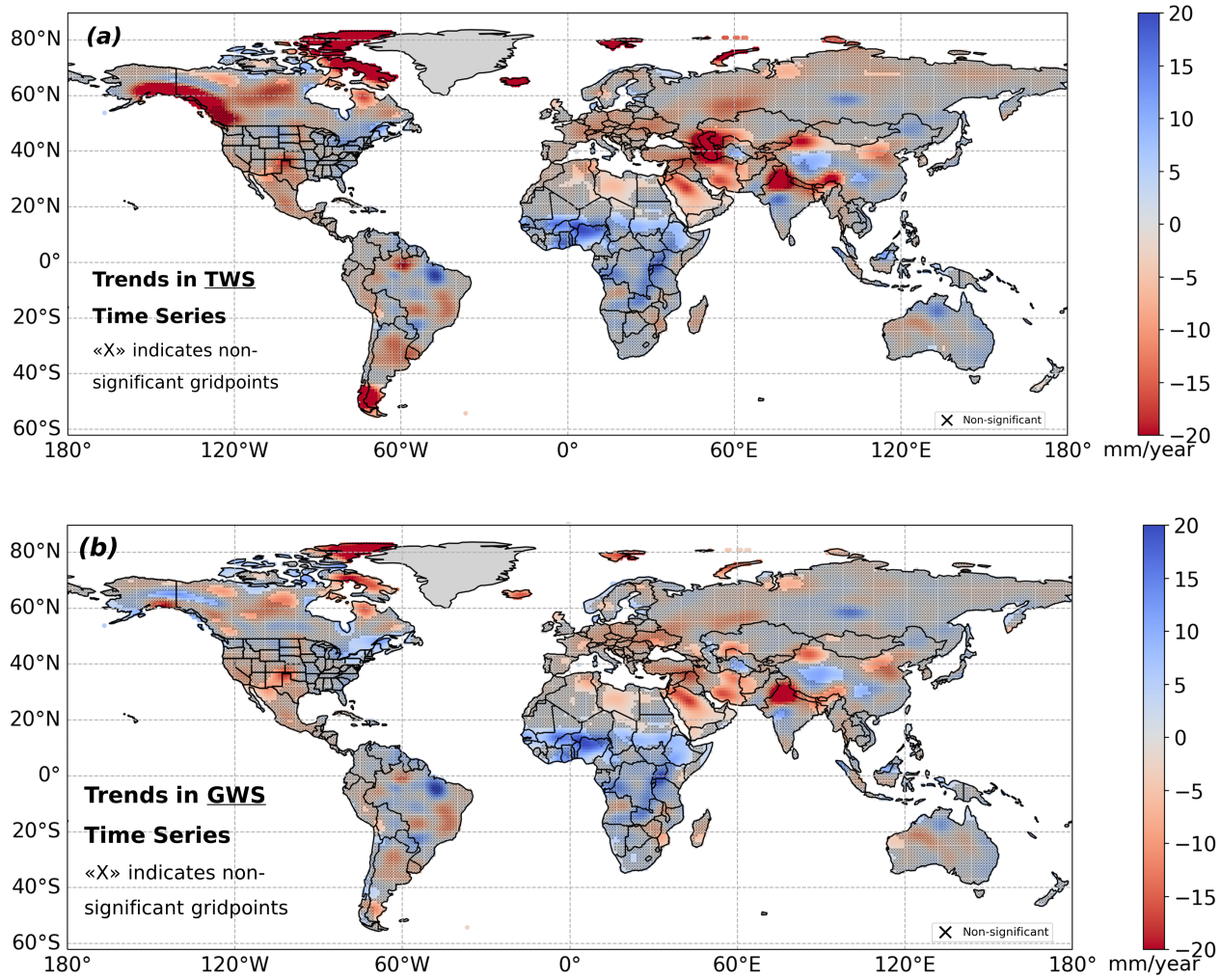


Figure 4: Central result of the global trend analysis: significant G3P TWS (panel a) and GWS trends (panel b) under consideration of the calibrated time series models introduced in Section 2, and the statistical test. Shading with "X" represents data with insignificant trends, while all non-shaded trends represent statistically significant trends.

In the following, we discuss the main TWS and GWS trend patterns shown in Fig. 4, ordered by continent and region. Where relevant, we relate these patterns to the component trends in RZSM, glacier mass, SWS, and SWE shown in Fig. 5, and to the auxiliary fitting parameters presented in the supplement.

[2] For individual storage components, deviations from normality are expected (e.g., RZSM and SWE); however, when propagated into TWS and GWS, these deviations are not expected to strongly impact the interpretation of trends.

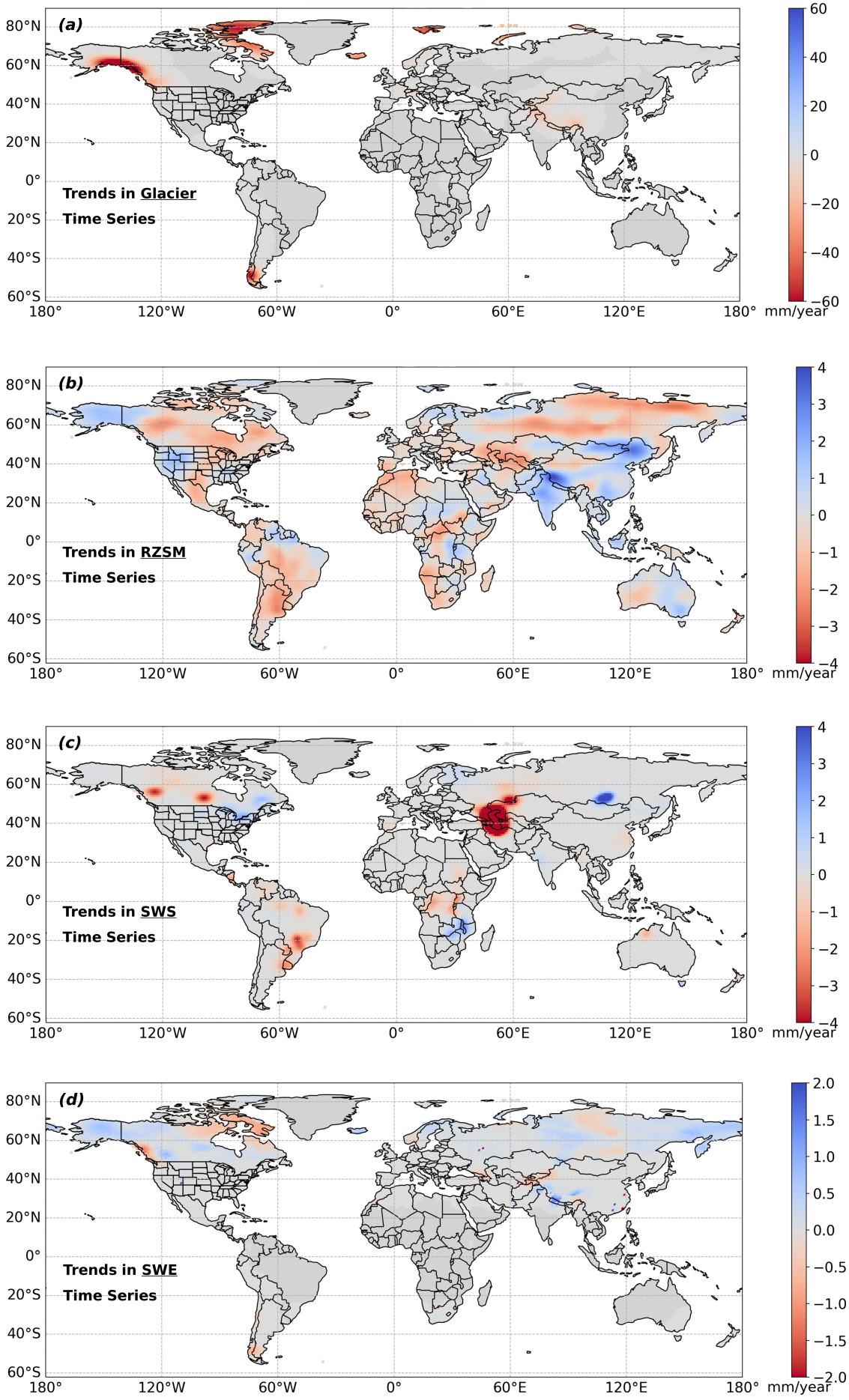


Figure 5: Global trends in Glacier glacier mass (panel a), RZSM (panel b), SWS (panel c) and SWE (panel d).

Major significant continental TWS trends At the global scale, the strongest significant TWS declines coincide with regions of strong ice loss (and glacier mass loss, including Patagonia/Southern Andes, Alaska, Arctic islands) and are and Arctic islands, consistent with earlier work (Velicogna, 2009; Jacob et al., 2012; Wouters et al., 2019; Braun et al., 2019; Ciracì et al., 2020). In the G3P glacier component (FigureFig. 5a), glacier retreat dominates low-frequency TWS decline in Canada, Alaska, the Arctic, Patagonia, and the Himalaya, reaching magnitudes up to ∼–100 mm/yr yr^{-1}. GRACE-derived glacier mass budgets similarly show strongly negative trends, e.g., in Alaska, Patagonia, Arctic Canada, Svalbard , and the Russian Arctic, and sum up in total summing to ∼199 km^3/yr yr^{-1} over 2002–2016(Wouters et al., 2019) (also , excluding Greenland and Antarctica)(Wouters et al., 2019). Additional prominent negative TWS trends are associated with drought and water depletion, including regions with possible or partial direct human impact (Rodell et al., 2018), and with long-term declines in the Aral and Caspian basins driven by irrigation diversion (Aral) or in the Aral region and regional aridification and enhanced evaporation (Caspian). In the following, we analyze the TWS and GWS trends (Figure 4) for each continent individually, accompanied by a discussion of drivers and auxiliary parameters from the fitting process. More detailed discussions can be found in Section S3.2, which especially addresses the rather complex trend situation in Northern Americain the Caspian region. In contrast, the significant GWS trends highlight non-cryospheric freshwater-storage changes, dominating other TWS declines. Major negative GWS patterns occur in intensively managed or semi-arid aquifer regions, including northern India, the North China Plain, Southwest/Central Asia, the High Plains Aquifer, parts of the southwestern US and northern Mexico, and North African fossil aquifer systems. Notably, positive GWS tendencies are most prominent in parts of the Sahel, the Niger Basin, Central/East Africa, and selected mid-latitude regions. Apparent GWS declines in Arctic and ice-adjacent regions require careful interpretation because residual leakage from cryospheric mass loss, GIA uncertainty, and imperfections in the subtracted storage components can propagate into the residual GWS estimate.

3.2.1. North America

Strong TWS declines For North America, our analysis separates four main regimes: cryosphere-dominated TWS decline in Alaska and Arctic Canada; significant non-cryospheric GWS losses in semi-arid and intensively managed aquifer regions; positive or weakly positive storage tendencies around the Great Lakes and eastern Canada; and regions where apparent TWS trends remain non-significant because of strong interannual variability and large trend uncertainty.

Alaska, Yukon, and the Canadian Arctic: The strongest significant TWS declines in North America occur near the Gulf of Alaska and the Canadian Arctic Archipelago, where they primarily reflect glacier /ice mass and ice-mass loss (Rodell et al., 2018; Wouters et al., 2019). Beside the Outside the strongly glaciated regions, significant TWS /GWS declines negative TWS and locally significant GWS trends in parts of the Mackenzie and Yukon basins are identified, consistent with permafrost-thaw-related hydrological change, indicating towards groundwater connectivity /including increased groundwater connectivity and discharge and associated shifts changes in soil moisture, surface water, and evapotranspiration (Lin et al., 2022; Wright et al., 2022). In the Alaska–Yukon region, GWS patterns should be interpreted cautiously because signal separation is challenging in glaciated and permafrost-dominated settings – coastal

The GWS pattern across Alaska and Yukon is spatially heterogeneous. Coastal negative anomalies may reflect residual leakage from glacier mass loss, and differences to earlier GRACE-period results (Muskett and Romanovsky, 2011; Lin et al., 2022) may reflect time-period dependence and/or the strong glacier-mass signal, whereas localized positive GWS tendencies of approximately +5 to +10 mm yr^{-1} extend across parts of central Alaska, Yukon, and the Yukon–Kuskokwim lowlands. Their contrast with groundwater losses reported for earlier periods may reflect temporal changes, product and processing differences, or limitations of the storage-component separation in glaciated and permafrost-dominated regions (Muskett and Romanovsky, 2011; Lin et al., 2022). Localized posi-

tive TWS and GWS tendencies also occur across parts of the western Canadian Arctic Archipelago, largely outside the regions of strongest glacier mass loss (Noël et al., 2018; Gardner et al., 2011). Because these areas are nevertheless affected by active permafrost degradation and thermokarst processes (Lewkowicz and Way, 2019; Fraser et al., 2018), the mechanisms underlying the positive trends remain uncertain.

In the Canadian Prairies (Alberta; eastern Canadian Arctic Archipelago, particularly the Queen Elizabeth Islands, significant apparent GWS declines of approximately -5 to -20 mm yr^{-1} require particular careful interpretation. They may be influenced by leakage from Greenland and local ice-mass loss, errors in the GIA correction, or imperfections in the modelled storage components. These high-latitude regions therefore represent a residual-GWS sensitivity zone in which robust TWS ice-mass loss cannot necessarily be interpreted as groundwater depletion. These map-level GWS tendencies are retained in the spatial figures for diagnostic interpretation, but all grid cells falling inside the defined mask (Sect. 2) are excluded from the volumetric GWS aggregation.

Western and central Canada: In the Canadian Prairies, particularly Alberta and the Saskatchewan River Basin), TWS declines , negative TWS tendencies are often not significant due to strong interannual variability, and are accompanied by large trend uncertainty statistically significant because of strong interannual and persistent low-frequency variability and the resulting large trend uncertainties (cf. Section S3.3, Figure S3), whereas GWSshows more robust significant declinesin parts of the basin, Sect. S2.4, Fig. S4). GWS, in contrast, shows more spatially coherent and locally significant declines. The shift of power-law κ values of the GWS series relative to TWS (Fig. S6) indicates reduced low-frequency variability after the component-separation step. This TWS–GWS contrast is one of the main regional findings for North America: groundwater-related drying can be detected more robustly than total-storage decline where TWS is dominated by interannual variability. The GWS pattern is broadly consistent with groundwater extraction abstraction under semi-arid conditions and recurrent drought (Hamdi and Goïta, 2023; Wang et al., 2025). Western/central Canadian drying patterns are broadly consistent with independent GRACE-based assessments (Wang et al., 2025; Li and Rodell, 2024). In northern Quebec and

Similar drying patterns occur around Great Slave Lake and towards the Hudson Bay region. In discontinuous-permafrost regions, thaw can enhance groundwater connectivity, subsurface drainage, and river discharge (Wright et al., 2022; Huang et al., 2025). Northern Quebec and adjacent regions also show a transition from previously reported wetting toward widespread drying, our analysis indicates drying, which is consistent with recent evidence for a transition toward widespread northern Canadian dryingand permafrost-driven storage losses (Li et al., 2016; Chandanpurkar et al., 2025; Huang et al., 2025; Wang et al., 2025), noting that Glacial Isostatic Adjustment (GIA) model uncertainty consistent with recent continental assessments (Li et al., 2016; Wang et al., 2025). However, GIA-model uncertainty is substantial around Hudson Bay and can affect both TWS and residual GWS trend magnitudes and, locally, their signs (cf. Section 3.2.7)can affect trend magnitudesSect. 3.2.7).

Great Lakes and eastern Canada: In the Great Lakes Basin, positive TWS tendencies are consistent with the observed 2013–2017 transition from record lows transition from record-low water levels in 2013 to record highs (Gronewold and Rood, 2019), while corresponding GWS trends are weak in our data, and differences to earlier shorter-period analyses (Huang et al., 2012) may reflect the longer time span available for this analysis. In eastern Canada, localized by 2017 (Gronewold and Rood, 2019). The corresponding GWS tendencies are positive but not statistically significant. This differs from the GWS decline reported for 2002–2009 by Huang et al. (2012), plausibly because the longer study period includes the pronounced post-2013 lake-level recovery.

Localized significant positive TWS /GWS trends likely and GWS trends also occur across parts of eastern Canada, including southern Quebec and the Ottawa Valley, and may reflect increased precipitation and recharge (Dubois et al., 2022), while differences to other products or groundwater recharge under cold and humid climatic conditions (Dubois et al., 2022). Their contrast with negative

trends reported for some eastern Canadian regions over shorter periods (Fatolazadeh and Goïta, 2021) may reflect resolution, end year, or GIA/signal-processing choices. Apparent GWS declines in the High Arctic (Queen Elizabeth Islands) require caution due to potential leakage from Greenland, GIA model errors or imperfections in the compartment componentsarise from differences in study period, spatial resolution, GIA correction, or signal processing.

Southwestern US, High Plains Aquifer, and northern Mexico: The clearest non-cryospheric GWS-depletion regime in North America extends across the southwestern US, the High Plains Aquifer, northern Mexico, and the Mexico City region. Significant TWS and GWS declines across New Mexico, Arizona, and the High Plains are consistent with groundwater abstraction for irrigation combined with recurrent drought (Scanlon et al., 2012; Konikow, 2015; Jasechko et al., 2024). In the High Plains Aquifer, local GWS trends exceed -20 mm yr^{-1}, consistent with the documented long-term depletion of the aquifer (Haacker et al., 2016).

Component trends support our interpretations: SWE shows negative trends in **Component-level interpretation:** The component trends help distinguish groundwater-related change from snow, surface-water, and soil-moisture contributions. SWE decreases across southwestern Canada and the Pacific Northwest (Figure 5d); SWS exhibits Canadian Pacific Northwest and also in parts of the eastern and northern Hudson Bay drainage regions (Fig. 5, panel d). In contrast, slightly positive SWE tendencies occur in parts of the Yukon and Mackenzie basins, indicating that their negative TWS tendencies are not explained by declining snow storage alone. SWS exhibits distinct basin-scale anomalies (e.g., Williston Lake; Lake Winnipeg; Great Lakes) which shows to be consistent with regulation and changes, including negative tendencies around Williston Lake and Lake Winnipeg, weaker negative tendencies around Great Slave and Great Bear Lakes, and positive tendencies in the Great Lakes and southern Quebec. These patterns are consistent with reservoir regulation, changing precipitation and flooding regimes, and observed lake-level variability (Shrestha et al., 2012; Beltaos and Peters, 2024; Kayastha et al., 2022); and RZSM indicates widespread drying in . RZSM decreases across substantial parts of central and western Canada, which is consistent with precipitation-regime changes and permafrost thaw impacts (Rodell et al., 2018; Li et al., 2016; Bonsal et al., 2019; Li and Wang, 2022). supporting the interpretation of regional drying associated with changing precipitation regimes and recurrent drought (Bonsal et al., 2019); in northern regions, these changes may interact with permafrost-thaw-related drainage and enhanced hydrological connectivity (Wright et al., 2022). Thus, the Canadian TWS pattern reflects contributions from several storage components, whereas the more spatially coherent GWS losses identify regions in which groundwater-related drying is particularly pronounced.

Regarding the USA and northern Mexico, significant

3.2.2. South America

Despite locally high-magnitude trend estimates, TWS and GWS declines occur across the southwestern US (including New Mexico and Arizona) andthe High Plains Aquifer, extending into northern Mexico; GWS also declines near Mexico City. These patterns are consistent with groundwater depletion for irrigation, and were intensified during recurrent droughts (Scanlon et al., 2012; Konikow, 2015; Jasechko et al., 2024), with exhibit few statistically significant trends across most of South America. More negative power-law κ values, locally approaching random-walk behaviour, indicate strong persistent low-frequency variability and correspondingly large trend uncertainties (Sect. S2.4, top and middle panels of Figs. S4 and S5). The main exceptions are the cryosphere-dominated TWS decline in Patagonia and localized significant GWS depletion in the High Plains Aquifer exceeding –20 mm/yr in our results (Haacker et al., 2016). Component trends show limited large-scale SWE/SWS contributions over the US, while RZSM trendsconfirm drought impacts across the Midwest and into northern Mexico (Figure 5).

3.2.3. South America

Apart from Patagonia ice-mass loss (Tapley et al., 2019; Rodell et al., 2018), we observe significant TWS/GWS declines in northern Altiplano and adjacent Andean drylands. Our analysis therefore separates these localized groundwater losses from extensive regions where strong interannual and persistent low-frequency variability prevents the robust detection of long-term trends. This contrast is particularly clear when GWS is considered separately from the Altiplano, with negative GWS trends (down to ∼–100 mm/yr) consistent with reports of groundwater decline from agricultural extraction and mining activity (Gonzales et al., 2025; Hernández et al., 2021; Kirshen et al., 2025). In the Andean "Lithium Triangle", brine/groundwater extraction also contribute to declines under limitedrecharge (5–30 mm /yr) (Kirshen et al., 2025). Localized low-magnitude positive GWS trends near the northern Argentina–southern Bolivia–northeastern Chile triangle may reflect recharge variability , while spatially offset Patagonia well-documented cryospheric TWS decline in Patagonia.

Altiplano and Andean drylands: The clearest significant GWS trends (northwestern Chubut positive; declines occur in the northern Altiplano, centred around La Paz and extending westward across the Peru–Bolivia–Chile tri-border region, with local trends reaching approximately -10 mm yr^{-1}. These declines are spatially consistent with regions affected by groundwater stress related to agriculture and mining (Gonzales et al., 2025; Hernández et al., 2021).

Farther south, parts of the Andean "Lithium Triangle" across northern Argentina, southwestern Bolivia, and northeastern Chile show localized low-magnitude positive GWS trends rather than a principal depletion signal. In these internally drained salar basins, freshwater inflow is very limited, with estimated recharge and streamflow of only about 2–33 mm yr^{-1}, while both brine and freshwater are extracted (Kirshen et al., 2025). The positive residual GWS tendencies may reflect spatial and temporal variability in recharge, differences between freshwater and brine-storage signals, or limitations of the storage-component separation. This should therefore not yet be interpreted as evidence that mining-related extraction has no hydrological effect.

Patagonia and the distinction between TWS and GWS: The strong TWS decline in Patagonia is primarily associated with the well-documented loss of glacier and ice mass (Tapley et al., 2019; Rodell et al., 2018). The corresponding GWS pattern is spatially offset, including positive tendencies in northwestern Chubut and negative tendencies in northeastern Santa Cruznegative) show limited correlation . Its limited spatial correspondence with the glacier component , which suggests the presence of non-ice-related hydrologic signalssuggests that these GWS tendencies do not simply reproduce the dominant cryospheric TWS signal. However, their interpretation remains sensitive to leakage and uncertainty in the separation of the storage components.

Across South America, many TWS /GWS trends remain non-significant due to strong interannual variability (PL **Amazon, La Plata, and São Francisco basins:** Across the Amazon, La Plata, and São Francisco basins, most apparent TWS and GWS trends are not statistically significant after accounting for strong interannual and persistent low-frequency variability, with more negative power-law κ values locally approaching random-walk ; Section S3.3). behaviour (Sect. S2.4). Non-significance is therefore an important result: visible regional tendencies cannot generally be distinguished robustly from stochastic storage variability over this study's data period. In the Amazon Basin, trends show the estimated trends form a dipole-like spatial structure (negative pattern, with negative tendencies in the north ; positive near the Delta) but are not significant; and pronounced positive tendencies near the delta, but neither constitutes a robust basin-wide trend. Although a basin-mean tendencies remain broadly consistent with tendency is broadly compatible with previously reported storage gains, while strong it is not statistically significant in our analysis. Strong ENSO events and subsequent recovery periods contribute to variability (Rodell et al., 2018; Chaudhari et al., 2019; Satizábal-Alarcón et al., 2024; Chandanpurkar et al., 2025). In substantially to the observed variability (Chaudhari et al., 2019; Satizábal-Alarcón et al., 2024). Similarly, drought-related storage losses previously reported for the southern La Plata region, drought-related declines reported for Basin, particularly during 2002–2009 (Chen et al., 2010), do not remain significant over 2002–2023, which is consistent with episodic drought and recovery (Naumann et al., 2022) events. Similarly, in the full study period. This can be consistently interpreted with the episodic

character of regional drought and with spatially uneven and partial recovery during subsequent periods (Naumann et al., 2022). In the São Francisco basin, reported depletion rates can still be masked by interannual variability, although there is evidence for streamflow reductions related to reduced groundwater discharge (Lucas et al., 2021; de Melo and Wendland, 2020) Basin, independent evidence for reductions in streamflow and groundwater-supported baseflow (Lucas et al., 2021; de Melo and Wendland, 2020) is likewise not expressed as a spatially extensive significant GWS trend in our analysis.

In sub-components (Figure 5), RZSM shows negative trends **Component-level interpretation:** The component trends support regional hydrological drying without implying widespread significant groundwater depletion. RZSM decreases across central South America(, including Bolivia, northeastern Argentina, Uruguay, Paraguay, southern/southwestern Brazil and southern to southwestern Brazil (Fig. 5). While projections suggest increasing soil moisture future projections indicate possible soil-moisture increases in southeastern South America (Saito et al., 2025; Lai et al., 2023), our results indicate a recent historical decline; partly decreasing RZSM trends have also been reported from satellite and reanalysis products (Hirschi et al., 2025). SWS shows negative trends (Lai et al., 2023), historical multi-product assessments show substantial regional variability and drying tendencies over recent decades (Saito et al., 2025; Hirschi et al., 2025). SWS also decreases in the broader São Francisco regionand around Uruguay/Paraguay , consistent with drought episodes and agricultural intensification (Chen et al., 2010; Naumann et al., 2022). , consistent with recurrent drought and documented reductions in streamflow and baseflow (Lucas et al., 2021; de Melo and Wendland, 2020). Negative SWS tendencies around Uruguay and Paraguay are consistent with recurrent drought conditions in the La Plata Basin (Chen et al., 2010; Naumann et al., 2022). These component trends help explain parts of the TWS signal but do not alter the principal GWS result: significant groundwater losses are concentrated in the northern Altiplano and adjacent Andean drylands, while parts of the Lithium Triangle show localized positive residual GWS tendencies. Significant long-term groundwater trends remain limited across most of the continent.

3.2.3. Europe

Across Europe, TWS trends are generally spatially coherent and Our analysis indicates a broad but mostly moderate GWS drying tendency across Europe. At the primary 99% significance level, negative GWS trends are spatially localized, particularly in eastern France, southern Ukraine, and northeastern Spain, broadly consistent with previously identified Euro-Mediterranean groundwater-depletion regions (Xanke and Liesch, 2022). Europe provides a useful example of moderate negative magnitude, with significant negative trends concentrated trends whose detected spatial extent depends on the significance threshold: At the 95% threshold, the negative GWS pattern becomes substantially more spatially coherent, extending from northeastern Spain across large parts of France into Germany and the Alpine region (to be discussed in Sect. 3.3). The 99%-significant trends are therefore embedded within a broader negative pattern that becomes apparent when the significance threshold is slightly relaxed.

An important feature is that significant GWS trends cover a larger part of Europe than significant TWS trends at both thresholds. At 99%, significant GWS trends cover 1.1 million km^2, compared with 0.8 million km^2 for TWS (Tables 2 and 1). At 95%, the corresponding areas increase to 2.2 and 1.3 million km^2, respectively (Tables S1 and S2). Thus, the broader GWS drying pattern is detected more consistently than the corresponding TWS pattern, despite the generally moderate magnitude of the GWS trends.

Localized positive GWS trends occur in Denmark, coastal southwestern Finland, Estonia, and coastal western Norway. These may reflect regional recharge variability, but direct attribution is beyond the scope of this study. In northern and coastal regions, component-separation errors and uncertainty in the GIA correction may additionally affect the residual GWS signal.

Relation between TWS and GWS: Across many non-glaciated parts of Europe, TWS and GWS trends show broad spatial correspondence, suggesting a substantial groundwater contribution

to regional TWS change. Significant declines in both variables occur particularly in southern Scandinavia and the northern UK, broadly consistent with while the broader GWS drying pattern is consistent with previous GRACE-based continental groundwater assessments (Xanke and Liesch, 2022). A negative trend in southern Scandinavia The central Scandinavian decline may indicate a reversal relative to earlier reported the wetting reported for 2002–2011 wetting (Wang et al., 2013), while northern UK trends are less documented in GRACE syntheses but there is alignment with (Wang et al., 2013). The northern UK signal is less prominent in previous GRACE syntheses and is only partly consistent with reported in-situ groundwater declines(Jackson et al., 2015). For GWS, significant negative trendsoccur in eastern France, southern Ukraine, and northeastern Spain, consistent with Euro-Mediterranean depletion zones (Xanke and Liesch, 2022), while novel positive GWS trends in Denmark, coastal southwestern Finland, Estonia, , which were mainly identified farther south (Jackson et al., 2015). The larger spatial extent of significant GWS trends, despite their smaller magnitude, likely reflects reduced temporal variability after removal of the other storage components. In TWS, seasonal and interannual variability from soil moisture, snow, and surface water increases trend uncertainty and can obscure moderate long-term groundwater-related changes. Because GWS is derived residually, however, this greater statistical detectability should not be interpreted as inherently lower physical uncertainty. The different spatial extent of significant TWS and GWS trends also highlights that trend magnitude and trend significance should not be interpreted interchangeably. At 99%, the significant European TWS cells have an area-weighted mean trend of -17.0 mm yr^{-1} and a net change of -13.1 km^3 yr^{-1}, substantially more negative than the corresponding GWS values of -3.4 mm yr^{-1} and coastal western Norway may reflect increased recharge-3.9 km^3 yr^{-1} (Tables 1 and 2). The strong TWS aggregate is therefore produced by a smaller significant area with comparatively large negative trends (e.g., Iceland), whereas the GWS drying signal is weaker in magnitude but significant over a larger area.

Component trends show weak-to-moderate RZSM **Other storage components and high-latitude sensitivity:** The component trends help explain this contrast. RZSM shows weak-to-moderate drying over Iberiaconsistent with enhanced evapotranspiration (Spinoni et al., 2016), near-neutral SWS , small SWE tendencies (northward positives, southward negatives), and negative , consistent with recurrent drought conditions (Spinoni et al., 2016), while SWS trends are mostly weak. SWE shows small positive tendencies in the north and negative tendencies farther south. Negative glacier trends over Norway and the Alps are consistent with accelerated glacier mass loss (Zemp et al., 2019; Ciracì et al., 2020). In GIA-affected regions(Fennoscandia, Because the adopted European domain also includes high-latitude cryosphere- and GIA-sensitive regions, the strongly negative continent-wide TWS aggregate cannot be interpreted as groundwater dominated without an additional cryosphere-specific diagnostic.

In Fennoscandia and the British Isles, Canada), uncertainty in the GIA correction can affect both TWS and residual GWS trend magnitudes andlocally signs remain sensitive to uncertainty in the GIA correction, locally, their signs. Residual GWS carries the additional uncertainty of the component-separation procedure, while leakage from glacier mass loss may further affect signals in western Norway. Northern Europe should therefore be regarded as an artefact-sensitive region, in the same sense as discussed for northern Canada.

3.2.4. Africa

Earlier studies emphasize natural variability in African TWS (Rodell et al., 2018; Ni et al., 2018). Our 2002–2023 analysis identifies statistically significant , but moderatemagnitude declines across northern Africa (Algeria/Tunisia/Libya/northern Chad/northern Egypt) – depletion of NSAS/NWSASisconsistent with Our analysis reveals one of the clearest continent-scale contrasts in GWS: statistically significant depletion across northern Africa is opposed by widespread positive GWS trends extending from the Sahel and Niger Basin into parts of central and eastern Africa. Localized declines additionally occur in southeastern Africa and Madagascar.

Northern Africa: Statistically significant, predominantly moderate, but large-scale GWS declines extend across Algeria, Tunisia, Libya, northern Chad, and northern Egypt. The spatial pattern is consistent with depletion of the North Western Sahara Aquifer System (NWSAS) and Nubian Sandstone Aquifer System (NSAS) reported in previous modelling and GRACE-based assessments and attribution primarily to groundwater pumping , with mixed atmospheric-flux contributions for NWSAS(Wada et al., 2012; Goncalves et al., 2013; Frappart, 2020; Springer et al., 2023; Shalby et al., 2023). Generally, our patterns are (Wada et al., 2012; Goncalves et al., 2013; Frappart, 2020; Springer et al., 2023; Shalby et al., 2023), now demonstrated to be significant. Groundwater pumping is commonly identified as the principal driver, although atmospheric water-balance variability may also contribute, particularly in the NWSAS. The broader pattern is also consistent with the high-resolution GRACE trend map TWS trend analysis of Kvas et al. (2024). Despite a considerable natural variability previously reported for African TWS (Rodell et al., 2018; Ni et al., 2018), the northern African GWS-depletion signal remains robust under our stochastic significance assessment.

In West Africa, pronounced significant positive TWS/GWS trends(often $> +20$ mm/yr) **West Africa and the Sahel:** Pronounced significant positive GWS trends, locally exceeding $+20$ mm yr^{-1}, are concentrated in the Niger Basin and align with reported Sahelian groundwater increases and the "Sahelian paradox" (recharge enhancement linked to surrounding Sahelian regions. These trends agree with previous reports indicating groundwater increases in the Sahel and are consistent with enhanced recharge associated with rainfall variability, land-use change) (Werth et al., 2017; Leduc et al., 2001; Favreau et al., 2009; Felfelani et al., 2017; Ahmed and Wiese, 2019; Springer et al., 2023). Central Africa shows a higher spatial heterogeneity: non-significant negative tendencies around , and the so-called "Sahelian paradox" (Werth et al., 2017; Leduc et al., 2001; Favreau et al., 2009; Felfelani et al., 2017; Ahmed and Wiese, 2019; Springer et al., 2023). Co-located positive TWS trends support the presence of a net regional water-storage increase, although the partitioning among storage components remains model-dependent. The available data also do not permit attribution of the GWS gains to a single recharge mechanism.

Central and East Africa: Central Africa exhibits greater spatial heterogeneity. Non-significant negative tendencies occur in parts of the Congo River and significant positive trends around Chad/Cameroon are affected from climate-mode influences (IOD/ENSO) and dominant subsurface contributions to basin storage (Felfelani et al., 2017; Jiang et al., 2021; Jarugula and McPhaden, 2023; Moihamette et al., 2024; Ahmed and Wiese, 2019; Springer et al., 2023). In East AfricaBasin, whereas significant positive GWS trends are found around Chad and Sudan (in the Sahelian zone) and Cameroon. These spatial contrasts may reflect the combined influence of subsurface storage variability and large-scale climate modes, including ENSO and the Indian Ocean Dipole (Felfelani et al., 2017; Jiang et al., 2021; Jarugula and McPhaden, 2023).

In the broader northern East African region, significant positive GWS trends are concentrated in the northern Rift region (southern Sudan/Ethiopia/Somalia), while across parts of South Sudan, large parts of Ethiopia, and Somalia. Farther south, strong interannual variability limits robust detection further south (Boergens et al., 2024b; Anyah et al., 2018; MacDonald et al., 2012). trend detection (Boergens et al., 2024b; Anyah et al., 2018), see Section S2.4, Fig. S5. Although pronounced trends characterize this region, the absence of widespread significant trends in these regions is therefore a result of the stochastic behaviour under long memory, as it is the case for Uganda, for example.

Southern Africa and Madagascar: Southern Africa shows general wetting tendencieswith localized GWS declines (e.g., southern Mozambique , Madagascar) consistent with reported drought conditions (Hoell et al., 2017; Spinoni et al., 2014). predominantly weak positive or non-significant GWS tendencies, interrupted by localized declines in southern Mozambique and Madagascar. These negative trends are spatially consistent with regions affected by recurrent drought (Hoell et al., 2017; Spinoni et al., 2014). Drying tendencies over southern Angola and Namibia are more evident in RZSM than in GWS, indicating that regional drying is expressed more clearly in soil moisture than in groundwater storage.

Component-level interpretation: Across Africa, TWS variations are largely governed by GWS fluctuations GWS also explains a substantial part of the large-scale TWS trend pattern, particularly the

contrast between northern depletion and Sahelian and East African gains (cf. Figures S3 and Figs. S4 , panel 1). Component trends show RZSM drying and S5). The component trends nevertheless show important regional differences. RZSM decreases in northwest Africaconsistent with Mediterranean precipitation declines and increased , consistent with declining Mediterranean precipitation and increasing drought frequency (Schilling et al., 2020; Hirschi et al., 2025), and also shows drying over southern Angola and Namibia (Cook et al., 2020; Hirschi et al., 2025). Additional RZSM drying tendencies in parts of central Africa requiring further investigation, and southern Angola/Namibia drying consistent with projections and satellite evidence (Cook et al., 2020; Hirschi et al., 2025). SWS shows negative trends in the Lake Tanganyika /Lake Victoria regions and along the Congo River, while Lake Malawi shows positive tendencies which is in agreement with recent remain uncertain and require validation with independent products.

SWS trends are spatially heterogeneous, with negative tendencies around Lakes Tanganyika and Victoria and positive tendencies around Lake Malawi. The former contrast with documented lake-level increases (Gbetkom et al., 2024). rises during 2019–2021, which could be the result of strong multi-annual variability and sensitivity to the analysed period (Gbetkom et al., 2024). The Lake Malawi tendency is not independently supported here.

3.2.5. Asia

Southwest Asia (Arab–Persian region): Significant GWS losses of ∼–8 to –10 mm/yr(with hotspots < −20 mm/yr) are consistent with Asia contains the largest continental net GWS loss and one of the most extensive significant groundwater-depletion patterns identified in our analysis. Major depletion regimes extend across Southwest and Central Asia, northern India, the North China Plain, and the Tarim Basin. Localized positive trends occur in western India, the Yangtze and Sichuan basins, parts of central China, and locally across the Tibetan Plateau. The observed continental pattern confirms wide-area groundwater losses, primarily caused by depletion, but also reveals regional contrasts related to groundwater recharge, reservoir-related storage effects, and climate variability.

Southwest and Central Asia: Significant GWS declines of approximately -8 to -10 mm yr^{-1}, with localized hotspots below -20 mm yr^{-1}, occur across the Arab–Persian region. Their spatial extent is consistent with previous GRACE-based evidence for groundwater depletion and reservoir regulation (Joodaki et al., 2014; Nikraftar et al., 2024) – losses are primarily linked of groundwater depletion widely attributed to irrigation-driven over-extraction abstraction under limited recharge . (Joodaki et al., 2014; Nikraftar et al., 2024). Countries most affected by negative trends are Saudi Arabia, Iran and Afghanistan. Notably, significant positive TWS and GWS trends occur across large parts of Turkmenistan. Their co-location coincides with the irrigation-induced regional redistribution of water storage (e.g., Gafurov et al. 2024.)

Central Asia (Caspian and Aral Sea basins): Caspian Sea decline is consistent with Farther north, strong TWS and SWS declines dominate the Caspian and Aral Sea basins. Caspian Sea losses result from increased evaporation and aridification (?). Aral losses reflect (Chen et al., 2017), whereas the Aral Sea signal reflects the long-term irrigation effects under drying climate effects of irrigation and increasingly dry climatic conditions (Wang et al., 2018). Significant negative GWS trends around the Aral Sea(to ∼–12 mm/yr) may reflect irrigation-driven depletion and/or artifacts from SWS separation, which requires further investigation, locally reaching approximately -12 mm yr^{-1}, may indicate groundwater depletion associated with irrigation. Although we observe a spatial separation, their attribution remains uncertain as errors in separating the large SWS signal can propagate into GWS.

South Asia(Indian subcontinent): Northern India is a dominant Asian hotspot of TWS/GWS loss (to ∼–40 mm/yr) resulting from forms one of the strongest global GWS-depletion hotspots, with local trends approaching -40 mm yr^{-1}. The spatial pattern is consistent with unsustainable irrigation pumping (Rodell et al., 2009; Dangar et al., 2021). documented by previous GRACE and groundwater studies (Rodell et al., 2009; Dangar et al., 2021). Significant negative GWS tendencies also extend eastward across parts of eastern India and Bangladesh, indicating that the broader depletion pattern is not confined to the northwestern Indo-Gangetic Basin.

In contrast, positive GWS trends (∼+10 mm/yr) near Surat (Gujarat) and eastward align with reported replenishment linked to management of approximately $+10$ mm yr^{-1} occur near Surat in Gujarat and extend eastward. These trends are broadly consistent with previously reported groundwater refilling in parts of western India and with the influence of monsoon-driven recharge variability and water-management interventions (Bhanja et al., 2017; Asoka et al., 2017). South Asia therefore illustrates that significant positive GWS tendencies can occur locally within a region predominantly characterized by depletion.

East Asia(China): Negative trendsover China shows a pronounced spatial contrast in the drivers of significant negative GWS trends. Over the North China Plain /Northeast Chinaare resulting from and parts of northeastern China, the observed negative significant trend pattern coincides with one of the country's best-documented regions of groundwater over-abstractionsupported by wells, modeling, supported by well records, hydrological modelling, and geodetic observations (Feng et al., 2013; Cao et al., 2013; Zhao et al., 2019; Gong et al., 2018; Zhong et al., 2023). The observed reductions in (Cao et al., 2013; Feng et al., 2013; Zhao et al., 2019). Significant GWS losses also extend across Xinjiang and the Tarim Basinare primarily driven by intensive water extractionin this hyper-arid region (Zhao and Li, 2017), while Yunnan/SW China negative trends align with drought linked to climate variability (Tang et al., 2014). Positive trends in the Yangtze/Sichuan Basinand parts of , where extremely arid conditions, limited recharge, and irrigation-dominated water use stress groundwater storage. Zhao and Li (2017) reported a slight basin-wide TWS decline and pronounced spatial heterogeneity, but did not isolate the groundwater contribution or attribute the decline specifically to water extraction. In the neighbouring Hexi Corridor, Tangdamrongsub et al. (2017) similarly found declining TWS and GWS during 2002–2010, with the strongest losses in the Shiyang River Basin linked to agricultural water use. By contrast, the negative GWS trends in Yunnan and southwestern China are more consistent with drought and climate variability than with the intensive pumping regimes farther north (Tang et al., 2014). Our results therefore reveal a spatial contrast between well-documented abstraction-related depletion over the North China Plain, irrigation-associated losses in parts of the arid northwest, and declines in Yunnan and southwestern China that are more consistent with drought and climate variability.

Positive residual GWS trends occur in the Sichuan Basin, parts of central China, and locally across the Tibetan Plateauare consistent with precipitation/recharge and reservoir effects (Yao et al., 2016; Cui et al., 2022; Wang et al., 2011). In Sichuan, these positive tendencies broadly coincide with regions where previous GRACE studies reported increasing TWS (Yao et al., 2016; Cui et al., 2022). However, neither study independently isolated groundwater storage from the other TWS components. Yao et al. 2016 inferred a combined contribution from surface water and groundwater, whereas Cui et al. 2022 identified reservoir storage and climatic factors as major controls. The resulting contrast between depletion in northern and western China and positive trends in parts of central and southern China is a prominent feature of the heterogeneous Asian GWS pattern.

Northern Asia (Russia and Arctic)Russia: Significant negative TWS /GWS trends Localized significant negative TWS and GWS trends occur over Taymyr and adjacent Kara Sea regionsare consistent with permafrost-thaw impacts on subsurface storage (Walvoord et al., 2012). More broadly, northern Russia shows . These signals may reflect hydrological reorganization associated with permafrost degradation, including enhanced groundwater connectivity and discharge. Such responses have been modelled for the Yukon Flats Basin in Alaska (Walvoord et al., 2012), but their applicability to Taymyr remains tentative. High-latitude leakage, uncertainties in the representation of snow and surface water, and permafrost processes not explicitly represented by the component models can all influence the GWS estimate.

Across northern Russia more broadly, weak-to-moderate drying patterns, often not significant, so these localized signals require continued monitoringnegative tendencies are spatially extensive but often not statistically significant. Their non-significance indicates that the apparent drying cannot generally be distinguished robustly from interannual and persistent low-frequency variability over the study

period.

Component trends across Asia show RZSM drying **Component-level interpretation:** The component trends emphasize the strong regional contrasts across Asia. RZSM decreases in the Caspian–Aral region(?Singh et al., 2012; Wang et al., 2018), wetting , whereas positive tendencies in northern India and northeast China (possibly reflecting irrigation return flow and greening) (Piao et al., 2020), and extensive northeastern China may reflect irrigation effects or wetter conditions; these interpretations require further investigation. Extensive RZSM drying across the northern Russian tundra /taiga requiring validationwith independent products (Bring et al., 2016; Chandanpurkar et al., 2025). and taiga requires further validation; Chandanpurkar et al. 2025 identified northern Russia as a mega-drying region. However, it did not yet affect GWS or TWS trends to be large-scale significant, which also holds for the 95% significance case (Figure S7). Also, its interpretation remains uncertain because Arctic soil-moisture is reported to respond regionally heterogeneous and are affected by changing evapotranspiration, permafrost conditions, and surface-water–groundwater connectivity (Bring et al., 2016).

SWS declines around the Caspian and Aral confirm documented losses (?Singh et al., 2012; Wang et al., 2018; Micklin, 2016); SWE shows broad positive Siberian tendencies despite decreasing snow-cover extent (Bulygina et al., 2011a), with negative seas indicate that surface-water loss contributes substantially to the regional TWS decline (Chen et al., 2017; Singh et al., 2012). Broad positive SWE tendencies across Siberia are broadly consistent with station observations showing increasing maximum SWE in parts of western and eastern Siberia, although the observation period and spatial coverage differ from those of the present analysis (Bulygina et al., 2011b). Negative SWE trends in the Caucasus and parts of the Central Asian mountains (Shahgedanova et al., 2020). Section S3.3 (PL κ and trend uncertainties) indicates elevated interannual variability in selected Asian hotspots (e.g., require independent validation. Elevated persistent variability in parts of Central Asia, the Middle East, parts of China). and China increases trend uncertainties and limits the spatial extent of statistically significant trends (Sect. S2.4). These component signals help interpret TWS patterns but do not alter the principal Asian GWS result: widespread groundwater depletion contrasts with significant regional gains and with areas where variability or component-separation uncertainty limits attribution.

3.2.6. Oceania/Australia

GRACE-based analyses show a Australia is characterized by a pronounced wet–dry contrast across Australia, with repeated and strong interannual variability rather than by spatially extensive significant GWS depletion. Previous GRACE-based analyses identify repeated storage gains in the tropical north /and northeast and persistent deficits over across western and southern regions Australia (Yang et al., 2020). Our component analysis indicates identifies a mild but significant GWS decline in central-west Western central-western Australia, consistent with GRACE–model fusion studies showing indicating groundwater-dominated long-term TWS reductions and rainfall deficits (Yang et al., 2020; Tangdamrongsub et al., 2017). Interannual variability, particularly in under persistent rainfall deficits (Yang et al., 2020).

In northern Australia, is strongly strong precipitation-driven ; interannual variability limits the detection of robust long-term trends. GRACE-derived TWS anomalies are tightly linked to vegetation anomalies (Yang et al., 2014). Long-term depletion in semi-arid, recharge-limited regions is consistent with global groundwater assessments (Döll et al., 2014)in this region are closely related to rainfall and vegetation variability (Yang et al., 2014), indicating that episodic wet and dry periods dominate the storage record. The principal finding is therefore not widespread groundwater depletion, but a localized significant GWS decline in central-western Australia embedded within otherwise highly variable and largely non-significant regional patterns.

3.2.7. The Role of Glacial Isostatic Adjustment (GIA)

GIA represents an important source of systematic uncertainty in GRACE/-FO trend analyses, particularly at northern latitudes and in formerly glaciated regions. Using an ensemble-

based framework, Eicker et al. (2024) demonstrate that in parts of North America and Fennoscandia the magnitude – and, in some localized cases, also the sign – of GRACE-derived TWS trends can depend on the adopted GIA realization. The strongest sensitivities occur in the region around Hudson Bay and northern Quebec, where GIA gravity-rate signals are large and rather heterogeneous , spatially heterogeneous and GIA-related uncertainty can locally exceed several $\mathrm{cm\,yr^{-1}}$ equivalent water height.

These regions coincide with areas highlighted in our analysis as requiring cautious interpretation, including northern Canada, parts of the Canadian Arctic Archipelago, Fennoscandia, and the British Isles. Importantly, however, Eicker et al. (2024) also show that At the same time, Eicker et al. (2024) show that hydrological trend estimates over large parts of Europe and other mid-latitude regions , hydrological trend estimates are comparatively robust with respect to GIA uncertainty. This supports the GIA-related stability of most of the continental-scale trends identified in our studyare comparatively less sensitive to the adopted GIA realization. This indicates that GIA uncertainty is particularly important at northern latitudes and in formerly glaciated regions, whereas most mid-latitude continental patterns are expected to be less strongly affected.

As Because G3P GWS is derived from TWSresidually from TWS and the remaining storage components, any residual GIA signal in TWS propagates directly into the estimated GWS trends. As a consequence, in In strongly GIA-affected regions, apparent GWS trends may be biased at the level of therefore be biased locally by several $\mathrm{mm\,yr^{-1}}$locally, which potentially affects trend significance near detection thresholds. For this reason, we recommend to interpret , potentially affecting both trend magnitude and statistical significance near the detection threshold. Residual GWS trends in the principal GIA regions with particular care, however, we emphasize that GIA-affected regions consequently require particular caution because they combine GIA uncertainty with uncertainty from the storage-component separation. Outside these northern-latitude sensitivity regions, the large-scale continental interpretations discussed in this study are plausible and are less likely to be dominated by GIA uncertainty and remain broadly consistent with literatureindependent hydrological evidence.

3.2.8. Rates-of-Change, 95% Threshold and Summary

3.3. Rates of Change and 95% Sensitivity

We Here we present continentally aggregated, area-weighted mean trends and associated volume changes volume-change rates derived from G3P grid-cell time series that exhibit statistically significant trends, as explained in Sectiondescribed in Sect. 2.2. Strong negative GWStrends over the northeastern Unless stated otherwise, continental and global balances in this section refer to the sums of grid-cell volume-change rates passing the specified significance threshold. Gross gains and gross losses are reported as positive magnitudes, and the net volume-change rate is calculated as gain minus loss. Significance is assessed separately for TWS and GWS. Greenland and Antarctica are excluded from both aggregations. The primary TWS aggregation domain retains all eligible grid cells, whereas the primary GWS aggregation domain excludes signals in parts of the Canadian Arctic Archipelago are likely affected by leakageand model limitations ; this region is therefore excluded from the GWS table analysisbecause these strong GWS trends are particularly sensitive to glacier-signal leakage, GIA uncertainty, and limitations in the storage-component models (Sect. 2). Consequently, the areas used for the TWS–GWS ratio analysis differ slightly; we assess this sensitivity separately.

Global 99% aggregates: Tables 1 and 2 summarise the 99%-significance-filtered TWS and GWS trend and volume-change statistics by continent and globally.

For TWS, the global volume balance of all net global volume-change rate over grid cells with significant trends amounts to −145-183.4 $\mathrm{km^3\,yr^{-1}}$(Table 1), . The aggregate is dominated by losses in Asia (−86.5North America (-90.5 $\mathrm{km^3\,yr^{-1}}$) and North America (−52.0Asia (-89.3 $\mathrm{km^3\,yr^{-1}}$), with smaller contributions from Europe (−15.9net losses in South America (-16.8 $\mathrm{km^3\,yr^{-1}}$) and South America (−16.8Europe (-13.1 $\mathrm{km^3\,yr^{-1}}$), while notably affected by gains in Africa (. Africa shows a net TWS gain of $+25.9$ $\mathrm{km^3\,yr^{-1}}$).

The global GWSvolume balance For GWS, the corresponding net global volume-change rate is $-26.5\ \mathrm{km^3\,yr^{-1}}$ (Table driven primarily by losses in Asia (-54.5. This net decline is primarily associated with Asia ($-55.3\ \mathrm{km^3\,yr^{-1}}$), with moderate smaller net losses in Europe (-4.7–$3.9\ \mathrm{km^3\,yr^{-1}}$) and North America [2] , North America ($-3.9\ \mathrm{km^3\,yr^{-1}}$), and gains in Africa ($+37.2$South America ($-0.7\ \mathrm{km^3\,yr^{-1}}$). Global groundwater losses , mostly driven by depletion, exceed -100These losses are partly offset by a substantial net GWS gain in Africa of $+37.2\ \mathrm{km^3\,yr^{-1}}$. The global gross negative GWS change amounts to $103.2\ \mathrm{km^3\,yr^{-1}}$.

Table 1: Significance-filtered TWS trend and water budget statistics by continent. Significant trends computed by $|\mathrm{trend}|/\sigma \geq 2.58$, corresponding to the 99% confidence level. The mean trend is the area-weighted mean over significant grid cells, and Net = Gain − Loss. The global mean trend is weighted by the total significant area.

	Areal coverage			Mean trend	Volume change		
Region	**Area** (10^6 km^2)	**Sig. area** (10^6 km^2)	**Sig. frac.**	**Trend** (mm yr^{-1})	**Gain** (km^3 yr^{-1})	**Loss** (km^3 yr^{-1})	**Net** (km^3 yr^{-1})
Africa	29.9	6.5	0.2	4.0	33.8	8.0	25.9
Asia	44.4	9.1	0.2	−9.8	8.8	98.1	−89.3
Europe	10.0	0.8	0.1	−17.0	0.8	13.9	−13.1
North America	22.2	3.8	0.2	−23.5	4.5	95.0	−90.5
Oceania	8.4	0.3	< 0.05	1.3	0.6	0.2	0.4
South America	17.6	0.8	< 0.05	−19.8	0.1	16.9	−16.8
Global	**132.5**	**21.4**	**0.2**	−8.6	**48.7**	**232.1**	−183.4

Table 2: Significance-filtered GWS trend statistics by continent. Significant trends computed by $|\mathrm{trend}|/\sigma \geq 2.58$, corresponding to the 99% confidence level. The mean trend is the area-weighted mean over significant grid cells, and Net = Gain − Loss.

	Areal coverage			Mean trend	Volume change		
Region	**Area** (10^6 km^2)	**Sig. area** (10^6 km^2)	**Sig. frac.**	**Trend** (mm yr^{-1})	**Gain** (km^3 yr^{-1})	**Loss** (km^3 yr^{-1})	**Net** (km^3 yr^{-1})
Africa	29.9	8.8	0.3	4.2	46.1	8.9	37.2
Asia	44.4	8.8	0.2	−6.3	13.0	68.3	−55.3
Europe	10.0	1.1	0.1	−3.4	1.4	5.3	−3.9
North America	21.2	4.5	0.2	−0.9	14.0	17.8	−3.9
Oceania	8.4	0.6	0.1	0.2	0.9	0.8	0.2
South America	17.6	0.8	< 0.05	−0.9	1.4	2.1	−0.7
Global	**131.5**	**24.7**	**0.2**	−1.1	**76.7**	**103.2**	−26.5

Our analysis of 2002–2023 G3P TWS and GWS trends reveals pronounced regional contrasts in continental water storage dynamics. The global TWS balance of -145**Global GWS-to-TWS ratios:** Using the defined primary aggregation domains, the net negative GWS aggregate of $-26.5\ \mathrm{km^3/\,yr^{-1}}$ is consistent with earlier GRACE-based assessments documenting large-scale intensification of the terrestrial water cycle (e.g., Wouters et al. 2019; Rodell et al. 2018). In contrast, the GWS component shows substantially different continental contributions, with net groundwater changes accounting for about 18approximately 14% of the net negative TWS aggregate of $-183.4\ \mathrm{km^3\,yr^{-1}}$, while the gross negative GWS change of $103.2\ \mathrm{km^3\,yr^{-1}}$ is approximately 44% of the corresponding TWS change of $232.1\ \mathrm{km^3\,yr^{-1}}$. The substantially smaller net than gross GWS-to-TWS ratio reflects compensation between regions of groundwater loss and gain. At the 99% threshold, significant GWS gains of $76.7\ \mathrm{km^3\,yr^{-1}}$ offset approximately 74% of the continental TWS balance, but

[2] The ice-sheet-covered part of the Canadian Arctic Archipelago is excluded due to known GWS artifacts.

exhibiting strong regional variability. Groundwater depletion dominates water losses in (approximately 63gross GWS loss, whereas significant TWS gains offset approximately 21% of the TWS decline there), remains a secondary contributor in North America (∼8%), and shows net gainsin Africa that partly compensate surface-water gross TWS loss. The comparatively small global net GWS decline therefore does not imply uniformly weak groundwater trends, but partly results from compensation between substantial regional losses and gains, particularly the positive GWS aggregate in Africa.

Sensitivity to the aggregation domain: Because the primary TWS and GWS aggregation domains differ slightly, we separately tested the sensitivity of these ratios to the treatment of the Canadian Arctic Archipelago. Applying the same exclusion mask used for GWS to TWS reduces its net and gross negative changes to -144.9 and soil-moisture losses. Greenland and Antarctica are excluded from the analysis. Our net global groundwater storage decline of $-26.5193.6$ $\mathrm{km^3\,yr^{-1}}$corresponds to ∼, respectively, yielding corresponding GWS-to-TWS ratios of approximately 18% of the continental TWS loss ($-145$and 53%. Conversely, retaining the excluded Arctic cells in the GWS aggregation increases its net negative and gross negative changes to -35.8 and 112.9 $\mathrm{km^3\,yr^{-1}}$). However, this net value contains substantial compensating groundwater gains in Africa. The gross groundwater loss (∼105, respectively. Thus, the primary descriptive GWS-to-TWS ratios are approximately 14% for net loss and 44% for gross loss, while the artefact-sensitivity analysis yields ratios of approximately 18–20% and 49–53%, respectively, depending on the treatment of the Canadian Arctic Archipelago.

Comparison with previous estimates and all-cell results: The gross negative significance-filtered GWS change of 103.2 $\mathrm{km^3\,yr^{-1}}$), is comparable to is of the same order of magnitude as earlier model-based estimates (100–150of global groundwater depletion of approximately 100–150 $\mathrm{km^3\,yr^{-1}}$; Döll et al. 2014) of depletion and accounts for approximately 53% of total gross continental water losses (103.2 of 193.6 $\mathrm{km^3\,yr^{-1}}$) – which is consistent with recent findings that groundwater dominates drying trends in non-glaciated continental (Döll et al., 2014). Most of the negative GWS aggregate is concentrated in established groundwater-depletion regions, although about 15% less than reported by (Chandanpurkar et al., 2025). Thus, the relative contribution of groundwater to total TWS changestrongly depends on whether global net budgets or drying-dominated continental regions are considered. climate-driven recharge deficits, drought-related storage changes, permafrost-related processes, and residual component errors contribute locally. Groundwater depletion can itself be intensified by drought through reduced recharge and increased groundwater abstraction, as observed, for example, in the Persian/Iranian region.

In **North America**, the continental TWS decline of about -52As a complementary estimate of storage change, we also integrated all retained grid-cell trends without conditioning on statistical significance (Tables S3 and S4). The resulting global gross negative changes are substantially larger, amounting to 469.4 $\mathrm{km^3\,yr^{-1}}$ for TWS and 262.6 $\mathrm{km^3\,yr^{-1}}$ is dominated by cryospheric losses, particularly in Alaska and Arctic regions. Groundwater depletion is localized, most prominently in the High Plains Aquifer and parts of the southwestern United States and northern Mexico, while California's Central Valley does not exhibit a significant long-term GWS trend over the extended study period. Across Canada, hydrological changes are influenced by permafrost thaw and climate variability, with several Arctic signals requiring cautious interpretation due to known leakage and model limitations. for GWS, corresponding to a gross GWS-to-TWS ratio of approximately 56%. This all-cell ratio is closer to the 68% groundwater contribution to TWS loss reported by Chandanpurkar et al. 2025, although differences in spatial domain and methodology remain.

South America experiences moderate TWS losses of approximately -17**Continental differences:** At the continental scale, the largest GWS contribution to significant TWS loss occurs in Asia: the net GWS loss is approximately 62% of the net TWS loss, and the gross GWS loss approximately 70% of the gross TWS loss. At the 99% threshold, significant trends cover approximately one fifth of the analysed Asian area for both TWS and GWS. Africa shows the opposite behaviour, with a net GWS gain of $+37.2$ $\mathrm{km^3\,yr^{-1}}$, largely driven by Patagonian ice mass loss, while groundwater contributes only marginally to continental totals. Localized GWS depletion associated with mining and irrigation is evident in the Altiplano, whereas much of the Amazon Basin shows strong interannual variability that masks trend significance.

Europe exhibits spatially coherent but moderate TWS declines (∼ −16compared with a net TWS gain of $+25.9\ \mathrm{km^3\,yr^{-1}}$), accompanied by glacier retreat in alpine regions. Groundwater depletion is evident in parts of southern and eastern Europe, while northern regions show mixed signals influenced by precipitation variability and GIA uncertainties in the North. . Significant GWS trends cover approximately 29% of the analysed African area, compared with approximately 22% for TWS.

Africa stands out with positive continental balances for both TWS (+26The relation between TWS and GWS is considerably different on the other continents. In North America, the descriptive net GWS-to-TWS ratio is approximately 4%, rising to about 8% when both variables are aggregated over the same geographic domain ($3.9/52.0$). The comparatively small net GWS loss reflects substantial regional compensation: significant GWS gains of $14.0\ \mathrm{km^3\,yr^{-1}}$) and GWS (+37offset most of the gross loss of $17.8\ \mathrm{km^3\,yr^{-1}}$), reflecting widespread groundwater recharge in the West African Sahel that compensate depletion in North African aquifers. Climate-driven precipitation variability linked to large-scale modes strongly influences East and Central African water storage patterns.

Asia accounts for the largest share of global TWS losses (−87. Thus, the spatially extensive groundwater-drying pattern does not yet translate into a comparably large continental net loss. Significant trends cover approximately 21% of the analysed GWS domain and 17% of the TWS domain. In Europe, significant GWS trends similarly cover a larger fraction of the analysed domain than TWS trends (approximately 11% versus 8%). In South America, in contrast, the significant TWS net loss of $-16.8\ \mathrm{km^3\,yr^{-1}}$), with groundwater depletion (−55is accompanied by only $-0.7\ \mathrm{km^3\,yr^{-1}}$) representing the dominant contribution. Major hotspots are northern India, the Arab–Persian region, and the North China Plain, while positive GWS trends are associated with water management and reservoir operations are evident in parts of western India and the Yangtze Basin. High-latitude regions of northern Asia show emerging negative signals, which are potentially linked to permafrost and evapotranspiration changes.

Oceania shows a strong wetting-drying contrast, driven by ENSO variability, with persistent TWS declines in western Australia and localized groundwater declines consistent with regional water stressof net significant GWS change. Thus, the continental TWS loss is not mirrored by a corresponding continent-wide groundwater-storage decline.

We have also repeated our water change analysis at a **95% sensitivity:** Repeating the analysis at the 95% confidence level (1.96 test threshold , Figure S6) , which essentially leaves the using a test threshold of 1.96 (Fig. S7) preserves the principal large-scale groundwater storage patterns and implications unchanged, but reveals that several significant-trend-adjacent regions (e.g. , over Europe) are exceeding the detection threshold for negative trends, which suggest emerging drying tendencies that are not statistically detectable at TWS and GWS patterns while increasing the spatial extent of trends classified as significant. Globally, the significant TWS area increases from 21.4 to 27.9 million $\mathrm{km^2}$, corresponding to an expansion of approximately 30% relative to the 99% level. Likewise, regarding the volumetric changes, using a 95%significance threshold indicates that the principal conclusions from the 99%analysis basically remain unaffected (see Tablesvalues, while the significant GWS area increases from 24.7 to 33.6 million $\mathrm{km^2}$, corresponding to a relative expansion of approximately 36%.

The corresponding changes in the integrated volume-change rates are more moderate. The net global TWS loss increases from -183.4 to $-199.7\ \mathrm{km^3\,yr^{-1}}$ (approximately 9%), and the gross negative TWS change from 232.1 to $264.5\ \mathrm{km^3\,yr^{-1}}$ (approximately 14%). The net GWS decline increases from -26.5 to $-31.4\ \mathrm{km^3\,yr^{-1}}$ (approximately 18%), and the gross negative GWS change from 103.2 to $128.8\ \mathrm{km^3\,yr^{-1}}$ (approximately 25%; Tables S1 and S2): The global continental TWS net loss increases moderately from -145 to $-161\ \mathrm{km^3\,yr^{-1}}$, while total gross continental TWS losses rise from 194 to 226 $\mathrm{km^3\,yr^{-1}}$. Similarly, net GWS decline goes from -26.5 to $-31.4\ \mathrm{km^3\,yr^{-1}}$, and gross groundwater depletion increases from 103 to 129 $\mathrm{km^3\,yr^{-1}}$. Importantly, the relative contribution of groundwater to total continental water loss changes only marginally: GWS accounts for ∼18% (. At the same time, the magnitude of the global area-weighted mean trend over significant cells decreases from -8.6 to $-7.2\ \mathrm{mm\,yr^{-1}}$ for TWS and from -1.1 to $-0.9\ \mathrm{mm\,yr^{-1}}$ for GWS. Thus, lowering the significance threshold primarily expands the detected

spatial footprint by accepting a broader set of moderate trends rather than substantially altering the storage-change budgets. This increased sensitivity is also accompanied by the expected rise in the nominal false-positive probability from 1% to 5%, while at the same time the risk of missing weaker true trends is reduced.

The relative relationships between the global significance-filtered aggregates also change only moderately. The net GWS-to-TWS ratio increases from approximately 14% to 16%, while the gross ratio increases from approximately 44% to 49%. Compensation between significant gains and losses is likewise stable: at 95%, GWS gains offset approximately 76% of the gross GWS loss, compared with approximately 25% for TWS, similar to the corresponding 74% and 21% values at 99%. This confirms that the comparatively small net global GWS decline is strongly influenced by compensation between regional groundwater losses and gains.

Regional changes at 95%: The increase in spatial coverage is particularly evident in Europe. Significant GWS area doubles from 1.1 to 2.2 million km^2, corresponding to approximately 11% and 22% of the analysed European area, respectively. For TWS, the significant area increases from 0.8 to 1.3 million km^2, or from approximately 8% to 13%. Negative GWS trends become more spatially coherent, extending from northeastern Spain across large parts of France into Germany and the Alpine region. The 99%) versus ∼20% (-significant trends are therefore spatially embedded within a broader moderate negative GWS pattern that becomes apparent when the significance threshold is relaxed.

The main continental contrasts remain remarkably stable under the lower significance threshold. In Asia, the significant area increases to approximately 26% of the analysed continental area for both TWS and GWS. The net GWS-to-TWS ratio changes only from approximately 62% at 99% to 60% at 95%) of the net TWS decline, and for approximately 53% versus 57% of total gross continental water losses.

Overall, while the sign and spatial distribution of continental water storage changes are robust, , while the corresponding gross-loss ratio remains nearly unchanged at approximately 70% and 69%, respectively. Africa retains positive net TWS and GWS changes, while the significant areas increase from 6.5 to 8.3 million km^2 for TWS (approximately 22% to 28% of the analysed area) and from 8.8 to 11.3 million km^2 for GWS (approximately 29% to 38%). In North America, the effect of several mechanisms significant-area fractions increase from approximately 17% to 23% for TWS and from approximately 21% to 30% for GWS. The net significant GWS loss correspondingly increases from -3.9 to -8.6 $km^3\,yr^{-1}$. A similar increase occurs in Europe, from -3.9 to -8.5 $km^3\,yr^{-1}$, whereas the much larger Asian net GWS loss changes only moderately from -55.3 to -60.8 $km^3\,yr^{-1}$. This contrast indicates that the broad moderate drying patterns in North America and Europe are more sensitive to the significance threshold, whereas the major Asian depletion signal is comparatively threshold-stable. In South America, the significant TWS net loss changes only slightly from -16.8 to -17.3 $km^3\,yr^{-1}$, whereas the net significant GWS change remains close to zero.

Taken together, lowering the significance threshold substantially expands the spatial coverage of detected trends, particularly for GWS and most prominently in Europe, while producing more moderate changes in the integrated storage budgets. The principal continental contrasts – particularly in GIA-affected regions strong and threshold-stable groundwater losses in Asia, compensating groundwater gains in Africa, increasingly coherent moderate GWS drying in Europe, and substantial South American TWS losses without a corresponding continent-wide GWS decline – remain uncertain and need further investigation. This includes an improved treatment of GIA and further independent validation with complementary geodetic and hydrological observations. As discussed, we also see a need to further analyze the attribution of driving mechanisms to GWS trends, however, this is beyond the scope of this workare preserved. The first-order spatial and volumetric interpretation is therefore robust to the selected significance threshold, while the absolute global GWS-to-TWS ratios remain moderately sensitive to the treatment of the artefact-prone Canadian Arctic Archipelago.

3.4. Assessment of trend significance and model evaluation

To provide a more detailed assessment of examine how trend magnitude and stochastic variability jointly determine trend significance, Figure 6 shows , for each GWS the estimated GWS trend against its standard deviation for each time-series cluster identified in Figure ??b, the scatter of trend magnitude to trend standard deviation. Gray shaded regions indicate statistically significanttrends; a logarithmic scale is 2. Gray-shaded regions denote trends classified as statistically significant, and logarithmic axes are used for clarity. As already suggested by Figure ??a, the purple and blue

The two globally dominant background-variability clusters (clusters 0 and 1) dominate globally and ; purple and blue) are largely characterized by insignificant trends (Figurenon-significant trends (Fig. 6, top panels). This also applies to The same applies to the Amazon high-amplitude seasonality cluster (cluster 5(; red), covering much of the Amazon Basin, where strong seasonaland interannualvariability leads to , interannual, and persistent low-frequency variability produces large trend uncertainties(bottom right panel). In contrast, the strong-decline/cryosphere-adjacent cluster (cluster 4(orange, bottom middle panel), mainly representing ; orange), which includes Arctic regions and parts of India, is dominated by significant negative trends with comparatively small scatter. Clusterlimited scatter. The positive-GWS-tendency cluster (cluster 3(green, bottom left panel) is characterized by ; green) contains spatially widespread groundwater increases across multiple continents, with approximately half of the trends reaching several continents, of which approximately half reach statistical significance.

Statistical significance does not, however, lead to unique physical interpretation. This is particularly important for significant residual GWS trends in Arctic and cryosphere-adjacent regions, where leakage, GIA uncertainty, and errors in the modelled storage components can affect the estimated signal.

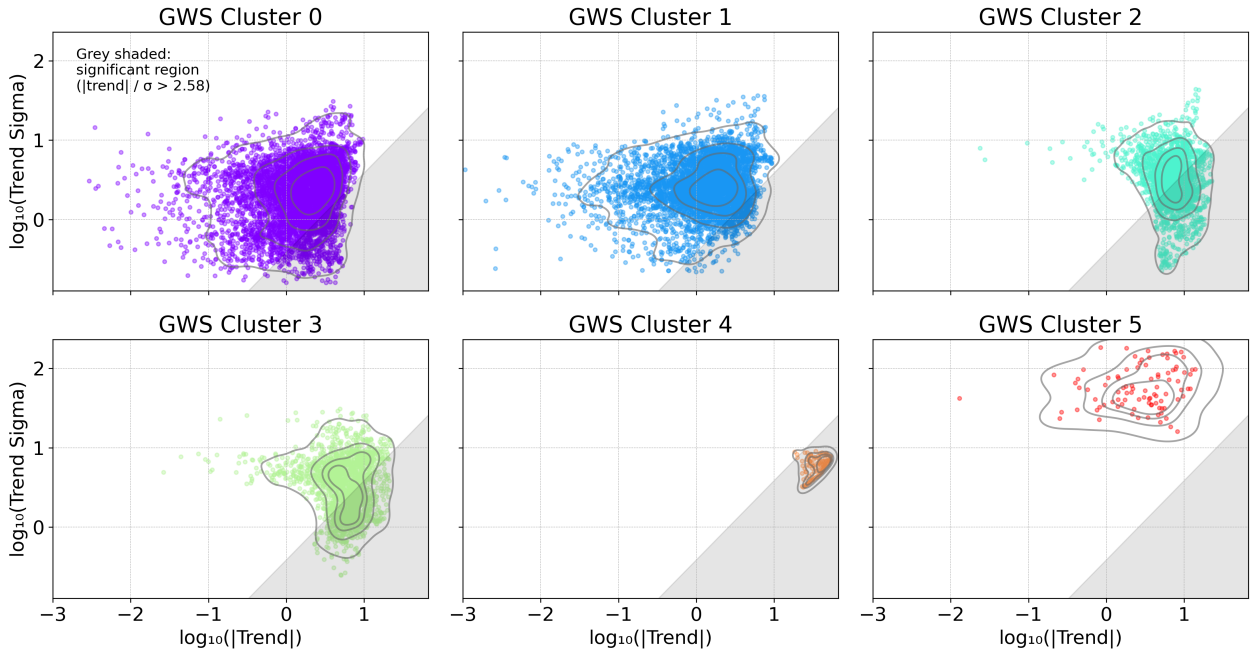


Figure 6: Analysis of GWS trend significance for each cluster of Figure 3. Dots represent trend magnitude versus trend standard deviation for each time-series cluster identified in Figure 2. Each dot represents one grid cell(a logarithmic scale is ; gray-shaded regions denote statistically significant trends. Logarithmic axes are used for clarity).

To further investigate the separation investigate the transition between significant and non-significant trends in more detail, we focus on GWS the moderate-GWS-drying cluster (cluster 2(turquoise; top right panel of Figure; turquoise; top-right panel of Fig. 6), which contains comparable numbers of significant and non-significant time series. Similar to the positive-GWS-tendency cluster, cluster 3, this clusterexhibits structured 2 exhibits a structured distribution of trend magnitudes, but with

larger scatter greater variation in trend uncertainty driven by interannual variability. Figure 7a shows the spatial distribution of cluster 2, with crosses marking time series with non-significant trends. associated with interannual and persistent low-frequency variability. The cluster predominantly comprises small to moderate contains small-to-moderate negative GWS trends , making it and is therefore well suited for evaluating illustrating the sensitivity of the significance detectionsignificance classification to both trend magnitude and residual variability. Figure 7a shows its spatial distribution, with crosses marking grid cells whose trends are not statistically significant.

We further sub-cluster To select spatially coherent examples of significant and non-significant time series, we further group the cluster 2 time series using K-means , based on trend significance (binary), based on binary trend significance and demeaned geographic latitude and longitude(demeaned), with all features standardized. Optimally interpretable results were obtained with We use seven sub-clusters. The resulting spatial separation of significant and non-significant series , which provide a practical balance between spatial coherence and interpretability. Because significance is itself included as a clustering feature, this grouping is intended to support visualization and comparison rather than to provide an independent validation of the significance classification.

The spatial distribution of the resulting sub-clusters is shown in Figure 7b, and the corresponding representative time series are presented in Figure 8. In each panel, the upper time series shows the observations (with, for better after removal of the fitted periodic components for visual clarity, periodic signals removed), while the lower panel shows series shows the residuals from the complete parametric model fit.

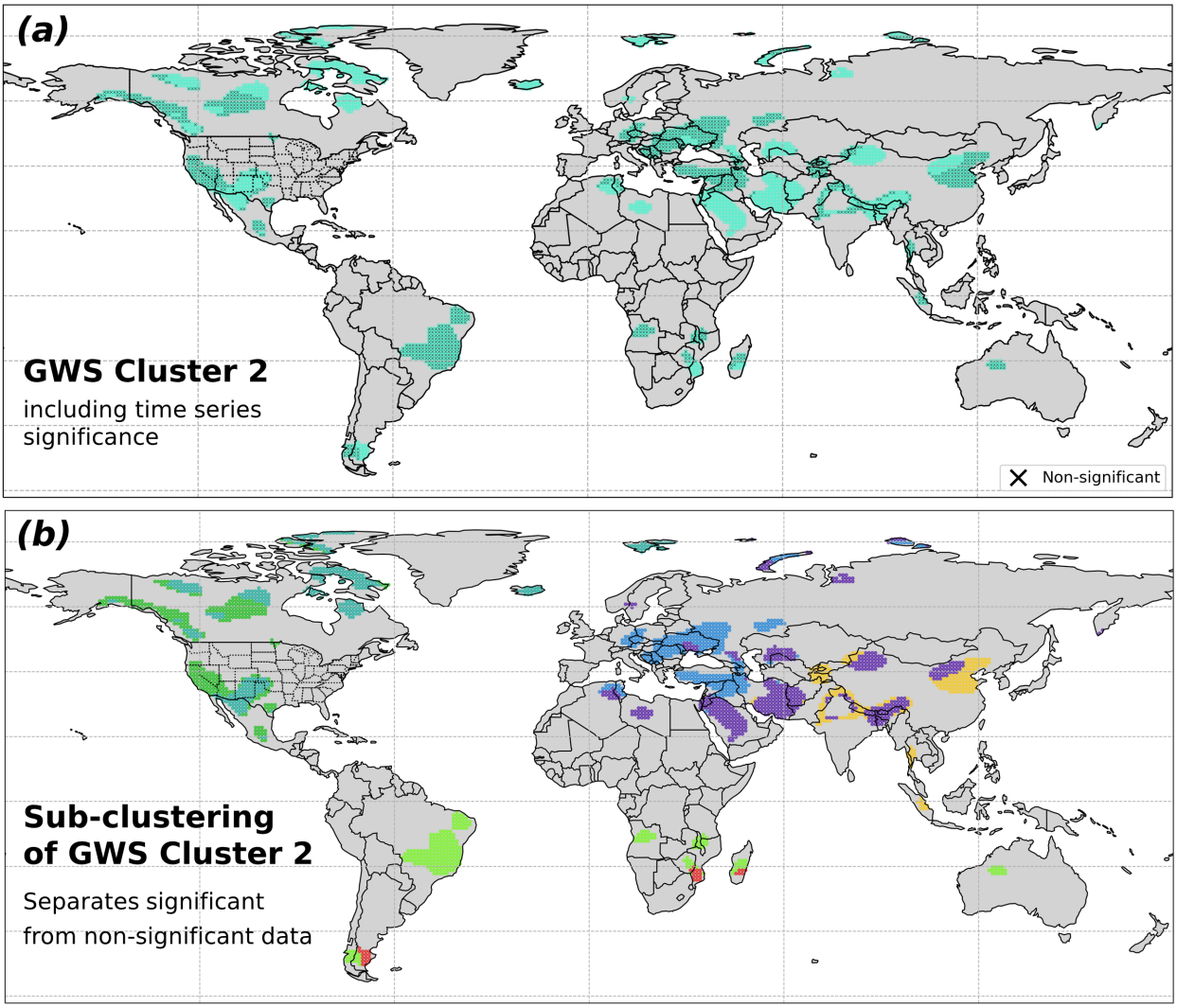


Figure 7: Panel (a): Spatial distribution of GWS cluster 2 from Figure ??2b; crosses indicate time series grid cells with non-significant trends. Panel (b): Sub-clustering results using based on binary trend significance and geographic locationas features, used to select spatially coherent examples of significant and non-significant time series.

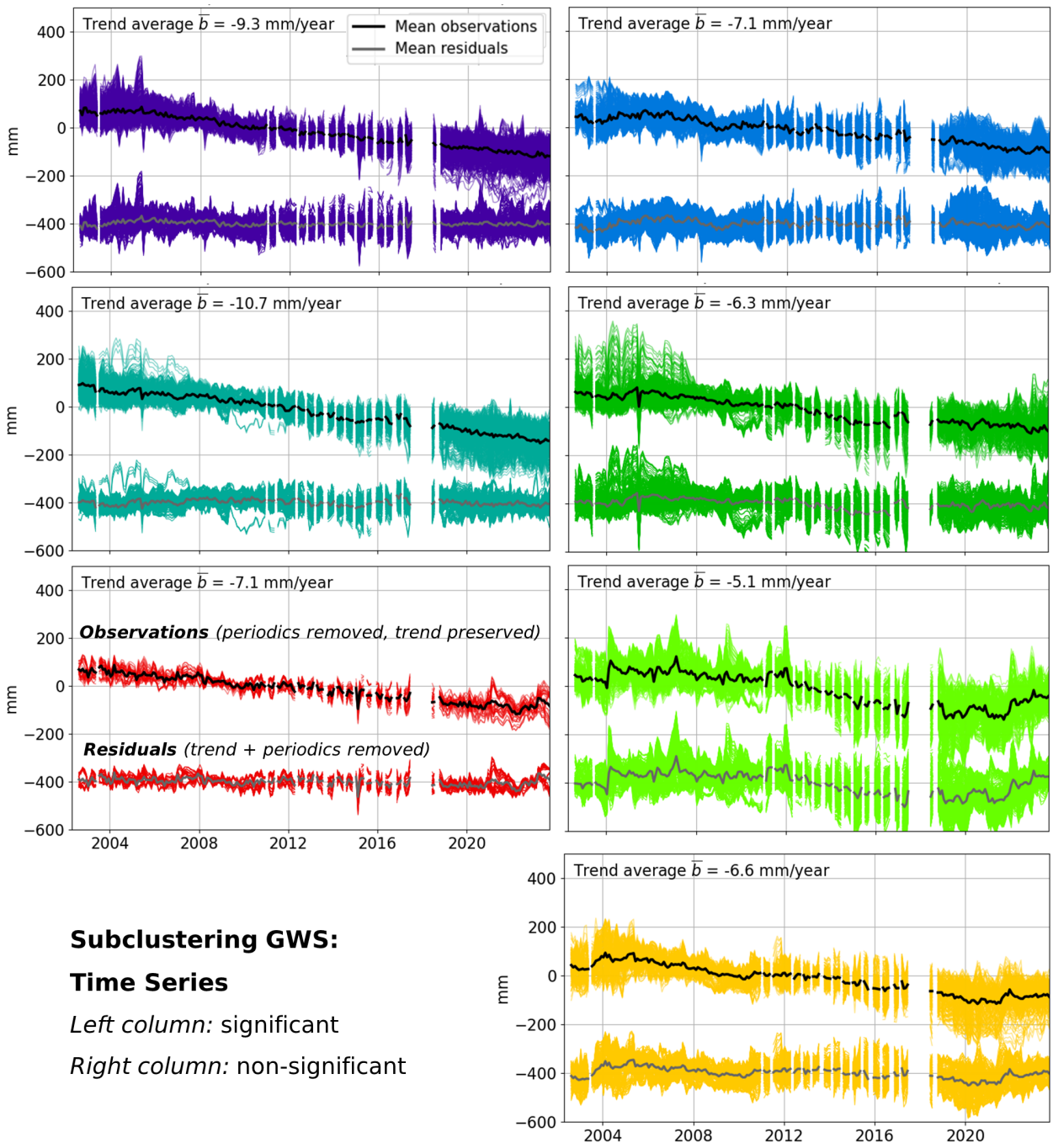


Figure 8: Time Representative time series corresponding to the sub-clustering of GWS cluster 2 (shown in Figure 7b). Left The left panels show significant sub-clusters ; and the right panels show non-significant onessub-clusters. Observations (top) and residuals (bottom) after removal of the fitted periodic components are shown for each caseabove the corresponding model residuals.

Comparison of the significant (left column) representative significant and non-significant (right column) time series in Figure 8 reveals systematic differences illustrates systematic differences in both trend magnitude and residual variability. Significant trends range from approximately -7.1 to -11 mm yr^{-1}, whereas the selected non-significant trends are weaker (generally weaker, ranging from approximately -5.1 to -7.1 mm yr^{-1}). Residuals of significant series exhibit less scatter, while . The significant examples also exhibit less residual variability, while stronger interannual and persistent low-frequency variations obscure the linear component in the non-significant series show stronger interannual variability that obscures linear trends. examples.

In several cases, the mean residual signal dominates over the linear component, and some time series display low-

frequency residual variations are comparable to or larger than the fitted linear change. Some time series additionally exhibit weak non-linear behaviour, such as including slight positive tendencies before approximately 2007. Although such differences are subtle, it demonstrates the feasibility of the applied significance detection framework.

Globally averaged power spectral densities (PSDs) of TWS (blue) and GWS (red) residuals (dashed), together with the corresponding PLWN model fits (solid).

To post-fit validate the trend detection and water storage change quantification approach, we validate the use of power-law white noise (PLWN) models for both TWS and GWS by comparing empirical and modelled PSDs (Figure **??**). The residual spectra show clear power-law behaviour, with reduced amplitudes across all frequencies following the G3P disaggregation. The PLWN fits reproduce the empirical PSDs well at low and intermediate frequencies (up to ∼1 cpy), which dominate long-term trend uncertainty. At higher frequencies , remaining intra-seasonal variability is not fully captured; however, this mismatch has negligible impact on trend uncertaintyestimates, which are governed primarily by the low-frequency spectrum (e.g., Bos et al., 2020).

Latitudinal distribution of groundwater storage (GWS) trends estimated using ordinary least squares (OLS) and generalized least squares (GLS). Each point represents a grid-cell trend plotted as a function of latitude. Horizontal lines indicate zero trend.

3.5. Sensitivity of groundwater storage trends to regression method

These examples illustrate that trend significance depends jointly on the magnitude of the fitted trend and the stochastic properties of the residual time series; relatively large apparent trends may remain non-significant when persistent variability produces correspondingly large trend uncertainties.

A comparison between OLSand GLS trend estimates highlights the influence of noise modelling on derived GWS trends (Figure **??**). When aggregated globally, area-weighted OLS trends yield a near-zero mean (-0.08 mm yr^{-1}) and a slightly positive median (0.22 mm yr^{-1}), whereas GLS estimates produce a more consistently negative signal, with a mean of -0.36 mm yr^{-1} and a median of -0.16 mm Further evaluations include comparison of the empirical residual spectra with the fitted stochastic models and an assessment of the sensitivity of GWS trends to the treatment of temporal covariance using OLS and GLS (Sect. S2.6 "Model evaluation and trend sensitivity"). The fitted models reproduce the low- and intermediate-frequency residual spectra well, including the frequencies most relevant for trend uncertainty. Compared with OLS, GLS yields a slightly narrower and more negative GWS trend distribution and global mean and median shifts of approximately 0.3–0.4 mm yr^{-1}. The latitudinal distribution further shows that GLS-derived trends show a reduced spread relative to OLS, which indicates better stability – this primarily reflects the down-weighting of interannual stochastic variability within the GLS framework. Overall, GLS trends are systematically shifted toward more negative values by approximately 0.3–0.4 mm yr^{-1} relative to OLS, while remaining small in magnitude at the global scale. All estimates shown here are derived from a 1° spatial grid following downsampling of the original data. This change in spatial resolution is not expected to materially affect the results, as spatial gradients in GWS trends are generally smooth between neighbouring grid cells.the sensitivity to proper covariance modelling. By accounting explicitly for temporal covariance, GLS provides more reliable trend estimates in the presence of persistent interannual variability and is less susceptible to such variability influencing the fitted linear trend, as particularly evident in the latitude-dependent comparison of Figure S9), e.g., for South America. The corresponding analyses are presented in Sect. S2.6.

Table 3: Summary of the main findings on G3P GWS and TWS trends for 2002–2023.

Region / scale	Main findings
Global	• At 99%, net and gross negative GWS changes are -26.5 and 103.2 $km^3\,yr^{-1}$, corresponding to approximately 14% and 44% of the primary TWS aggregates. At 95%, the corresponding ratios are approximately 16% and 49%. • Lowering the significance threshold from 99% to 95% expands significant area by approximately 30% for TWS and 36% for GWS, while net-loss magnitudes increase by only approximately 9% and 18%, respectively. • Regional gains offset approximately 74–76% of gross GWS losses, compared with 21–25% for TWS; the relatively small net global GWS decline therefore masks substantial regional gains and losses. • The significance-filtered gross negative GWS change is of the same order as previous model-based groundwater-depletion estimates (Döll et al., 2014).
North America	• Groundwater losses extend across western and central Canada, the High Plains, the southwestern United States, and northern Mexico, whereas positive tendencies occur in eastern Canada and around the Great Lakes. Regional gains offset most gross GWS losses, while cryospheric contributions strongly affect the continental TWS budget.
South America	• Significant GWS losses are concentrated in parts of the northern Altiplano, while persistent interannual variability limits trend detection across much of the continent. The significant continental TWS loss is not accompanied by a corresponding continent-wide GWS decline.
Europe	• Moderate negative GWS tendencies become substantially more spatially coherent at 95%; significant GWS area doubles from 1.1 to 2.2 million km^2. The considerably stronger continental TWS aggregate reflects contributions beyond groundwater.
Africa	• Strong regional contrasts occur between losses in northern Africa and gains across the Sahel, Niger Basin, and parts of central and eastern Africa. Africa exhibits the largest continental net GWS gain; much of the positive storage signal is consistent with increased precipitation and recharge and compensates groundwater losses elsewhere.
Asia	• Asia exhibits the largest continental net GWS loss, with extensive depletion across Southwest and Central Asia, northern India, northern China, Xinjiang, and the Tarim Basin. • China shows pronounced regional contrasts between abstraction-related depletion in the North China Plain, irrigation-associated losses in the arid northwest, climate-related declines in the southwest, and positive trends in parts of central and southern China. • The continental drying signal is robust to the significance threshold: net GWS-to-TWS ratios are approximately 62% and 60%, and gross-loss ratios approximately 70% and 69%, at 99% and 95%, respectively.
Oceania / Australia	• Significant GWS trends remain localized, including losses in central-western Australia; strong precipitation-driven interannual variability limits robust long-term trend detection across much of northern Australia.
General	• GWS is the dominant individual storage-component signal across most of the analysed spectral range, including much of the seasonal-to-interannual variability, whereas glacier mass dominates at the lowest frequencies. Negative GWS tendencies are particularly widespread across the Northern Hemisphere, especially Canada and Europe, with broadly corresponding RZSM drying tendencies. • Separation of non-groundwater components reduces low-frequency persistence and median trend uncertainty from 3.86 to 2.59 $mm\,yr^{-1}$. • Trend significance depends jointly on trend magnitude and persistent variability; substantial apparent trends can therefore remain non-significant in variability-dominated regions such as South America. • The global pattern is heterogeneous, with neighbouring depletion, gain, and variability-dominated regimes.

4. Conclusion and Outlook

In this studywe perform a consistent global assessment of statistically significant linear terrestrial , we present a globally consistent assessment of terrestrial water storage (TWS) and groundwater storage (GWS) trends using the Global Gravity-based Groundwater Product (G3P) and 21.5 years of GRACE/GRACE-FO satellite gravimetry observations (observations from 2002 –2023). Using a calibrated trend-analysis framework that accounts for seasonal and interannual variabilityas well as the memory properties of hydrological time series, we quantify continent-scale volumetric water storage changes from statistically significant trends and so separate persistent signals from stochastic (natural) variability and observation errors.

Our analysis confirms well-documented TWS patterns dominated by global-warming-induced ice and glacier mass loss, as well as groundwater depletion in intensively irrigated regions (e.g., Rodell et al., 2018; Scanlon et al., 2018), and reveals previously unresolved regional groundwater patterns. These include widespread and statistically significant GWS increases across large parts of Africa, newly detected groundwater declines in parts of Canada, Europe, and Russia indicative of emerging high-latitude drying, and spatially coherent GWS reductions in eastern Brazil and other drought-affected regions (e.g., South Africa, Madagascar)to 2023. Trend and periodic signals are estimated for each grid-cell time series together with a calibrated stochastic model of residual temporal covariance, allowing trend uncertainties to account for interannual variability, hydrological memory, and remaining observational noise. This provides significance-filtered continental and global groundwater gain, loss, and net storage-change estimates, complemented by aggregates over all retained grid-cell trends.

At the global continental scale (excluding Greenland and Antarctica), we find significant net TWS losses of approximately -145 km^3 yr^{-1} and net GWS losses of -26.5 km^3 yr^{-1}. Total gross continental TWS losses amount to $\sim$194 km^3

99%confidencelevel, significance – filterednetTWSandGWSchangesamountto

-183.4*and*-26.5 $km^3\,\mathrm{yr}^{-1}$, of which gross groundwater loss – mostly by depletion - contributes $\sim$ 103 km^3 while gross negative changes reach 232.1 and 103.2 km^3 yr^{-1}($\sim$53%). Glacier retreat remains the dominant contributor to the net TWS trend, and net groundwater losses represent only $\sim$18% of the continental net TWS balance due to substantial compensating recharge, particularly across Africa. Spectral analysis further demonstrates that GWS changes dominate the residual interannual TWS variability after removal of other storage compartments. Interannual variability in both TWS and GWS is well described by long-range dependent processes, whereas RZSM primarily governs seasonal variability and exhibits short-range memory. , respectively. Over the primary aggregation domains, these correspond to descriptive GWS-to-TWS ratios of approximately 14% for net change and 44% for gross negative change; artefact-aware sensitivity tests yield approximately 18–20% and 49–53%, respectively. Integrating all retained grid-cell trends increases the gross negative changes to 469.4 km^3 yr^{-1} for TWS and 262.6 km^3 yr^{-1} for GWS, corresponding to a gross GWS-to-TWS ratio of approximately 56%. Net balances additionally conceal substantial compensating groundwater gains, particularly in Africa.

Regionally, Asia exhibits the strongest groundwater declines (mostly from depletion, ~-55 km^3

Theprincipalglobal, regional, andmethodologicalfindingsaresynthesizedinTable 3.AsiaaccountsforthelargestnetGWSloss(

-55.3 $km^3\,\mathrm{yr}^{-1}$), driven by extraction in the Indo-Gangetic Plain, with extensive depletion across Southwest and Central Asia, northern India, the North China Plain, and the Middle East, where groundwater accounts for approximately 63% of the continental TWS decline and thus represents the dominant drying mechanism. In contrast, Africa shows widespread positive GWS trends ($\sim$ +37 km^3 Tarim Basin. Africa exhibits the largest compensating GWS gain (+37.2 km^3 yr^{-1}), particularly across western, central , and eastern regions, which is consistent with sustained recharge linked to changing precipitation regimes. North America shows comparatively small net GWS losses concentrated in agricultural and drought-affected regions, with continental TWS decline largely governed by cryospheric losses in Alaska and Arctic regions. South America is dominated by strong seasonal variability and Patagonian glacier mass loss, so far limiting the detection of potentially-present groundwater trends . Across the Northern Hemisphere, larger areas of Canada and especially of Europe and Russia are tending towards negative groundwater trends, which reflects increasing climate-driven stress and broadly consistent with recent GRACE-based drying assessments (e.g., Chandanpurkar et al., 2025). Apparent negative GWS trends over parts of with positive trends from the Sahel and Niger Basin into parts of central and eastern Africa despite continued depletion in northern Africa.

Broad groundwater drying is also evident across western and central Canada and Europe, whereas persistent variability limits detection of spatially extensive trends across much of South America. Groundwater depletion can additionally be intensified by drought through reduced recharge and increased abstraction, illustrating coupled climatic and anthropogenic controls. Residual GWS trends in GIA-, cryosphere-, surface-water-, reservoir-, and permafrost-affected regions, such as the Canadian Arctic Archipelagowere excluded from continental budgets due to likely influences from leakage, GIA uncertainties, and potential compartment estimation limitations, require particular caution and should not be interpreted as groundwater change from statistical significance alone.

Across most of the analysed spectral range, residual GWS shows the largest spectral amplitudes among the individual storage components, including much of the seasonal-to-interannual range, whereas glacier mass dominates at the lowest frequencies. Because GWS is derived residually, it may also contain TWS errors and variability not represented in the subtracted components. Negative GWS tendencies are particularly widespread across the Northern Hemisphere.

Repeating the analysis at a the 95% significance threshold confirms the robustness of these conclusions. Net continental TWS losses increase moderately from -145 to -161 km^3 yr^{-1}, and net GWSlosses from -26.5 to -31.4 km^3 yr^{-1}. Gross continental TWS losses rise from 194 to 226 km^3 yr^{-1}, and gross groundwater depletion from 103 to 129 km^3 yr^{-1}. Importantly, the relative groundwater contribution changes only marginally (net : $\sim$18% to $\sim$20%; gross : $\sim$53% to $\sim$57%), which indicates on the robustness of the chosen trend analysis approach – the use of a strict confidence level preserves the principal spatial and volumetric conclusions. Relative to 99% significance threshold shows that weak or noise-dominated trends may remain undetected. Importantly, the reduction from TWS to GWS not only isolates groundwater dynamics but also reduces interannual stochastic variability %, significant area expands by approximately 30% for TWS and 36% for GWS, leading to improved detectabilityof persistent groundwater change. Based on our analyses, we also find that global GRACE-derived TWS/GWS change estimates are sensitive to methodological choices. For example, Chandanpurkar et al. 2025 reported continental losses exceeding 300 km^3 whereas net-loss magnitudes increase by only approximately 9% and 18%, respectively. The net GWS-to-TWS ratio changes from approximately 14% to 16%, and the gross ratio from 44% to 49%. Relaxing the threshold therefore primarily expands the spatial extent of detected moderate trends rather than altering first-order storage-change budgets.

The model evaluation shows that trend significance depends jointly on trend magnitude and persistent stochastic variability. Power-law-plus-white-noise models reproduce the low- and intermediate-frequency residual spectra governing long-term trend uncertainty. Separation of modelled non-groundwater components generally reduces low-frequency variability and associated stochastic trend uncertainty, improving GWS detectability, but introduces additional uncertainty from the RZSM, SWS, SWE, and glacier-storage products. Accounting for temporal covariance through GLS yields a slightly narrower global GWS trend distribution shifted by approximately 0.3–0.4 mm yr^{-1} whereas our significance-constrained aggregation yields lower values, which are closer to aggregation of regionally-resolved analyses such as Rodell et al. 2018 and independent toward more negative values relative to OLS, with the largest differences in South America. Global water-storage trend estimates therefore remain sensitive to stochastic modelling, product selection, spatial masking, component separation, and significance criteria.

Compared with approaches based primarily on deterministic trend fitting or direct TWS interpretation, the framework combines component-resolved groundwater estimation, calibrated temporal-covariance modelling, and significance-aware volumetric aggregation. This allows long-term trends to be distinguished more effectively from persistent hydrological variability and provides a clearer distinction between trend magnitude, detectability, and uncertainty.

The significance-filtered gross negative GWS change of 103.2 km^3 yr^{-1} is of the same order of magnitude as previous model-based groundwater depletion estimates (e.g., Döll et al., 2014). consequently, we expect our reported TWS estimates of global groundwater depletion (e.g., Döll et al., 2014). The complementary all-cell integration yields substantially larger gross negative changes and a GWS-

to-TWS ratio of approximately 56%, closer to the 68% groundwater contribution to TWS loss reported by Chandanpurkar et al. (2025). Differences in spatial domain, component definition, and aggregation methodology prevent direct equivalence between these estimates. The significance-filtered and GWS volumetric change rates as conservative, reliable and robust bounds on global continental water storage change all-cell aggregates should therefore be interpreted as complementary measures of detected and spatially integrated storage change rather than universal global mass-balance or uncertainty bounds.

Regarding future work , an improved characterization of storage compartment components– Future work should improve characterization of the non-groundwater storage components, particularly RZSM, SWS, and SWE, whose uncertainties directly affect GWS trend estimates in regions with weak signals or strong interannual variability – should be envisaged. Beside further compartment product analyses, an improved SWE, and glacier storage, whose errors propagate directly into residual GWS trends. A more complete uncertainty assessment should jointly account for the reduced stochastic uncertainty achieved through component separation and the additional uncertainty introduced by the component products. Improved leakage treatment and refined GIA corrections are critical aspects for interpreting trends GIA corrections remain particularly important in high-latitude , and glacier-dominated regions(such as the Canadian Arctic Archipelago). Cross-TWS-product evaluations have documented , while systematic differences between spherical-harmonic-based and mascon-based water storage products in drought recovery, hydrological memory, and precipitation–storage relationships across climate regimes (Akan et al., 2025), which raises the need for further analysis. Regions with GWS trends on the level to significance (e.g., in Europe, more general on the northern hemisphere) need continued monitoring, as persistent trends may intensify with longer observational records. Additional spherical-harmonic and mascon TWS products (Akan et al., 2025) motivate cross-product trend and uncertainty assessments. Spatially correlated uncertainty in aggregated storage-change estimates and field-wide significance across the global grid also warrant further investigation.

Independent constraints from hydrological models, space-geodetic observations(e.g., GNSS, InSAR), and in-situ groundwater measurements will be essential for improved attribution of observed TWS and GWS changes. Extending the framework to longer time series, including upcoming groundwater observations, and complementary geodetic measurements such as GNSS and InSAR will be important for separating climatic, anthropogenic, and model-related contributions. Longer records from GRACE-C and mass change subsequent mass-change missions, together with the integration of measurement stability uncertainty concepts (Gobron et al., 2026) (taking full leverage explicit measurement-stability uncertainty concepts (Gobron et al., 2026; Merchant et al., 2026) and full use of validated G3P formal uncertainties), are expected to further enhance the reliablity of trend detection under the presented approach, should further improve trend detectability and volumetric change estimates.

Data availability

The G3P v1.12 data used in this study are publicly available via the GFZ GravIS portal (https://gravis.gfz.de/gws).

The processed TWS and GWS time series and the resulting GLS parameter estimates are archived at Zenodo: https://doi.org/10.5281/zenodo.18538047.

Code availability

The Hector software (Bos et al., 2008, 2021), used for stochastic time-series modelling and variance component estimation, is publicly available at https://teromovigo.com/product/hector/ . All analyses were performed using this software together with standard scientific Python libraries. The complete statistical framework, including model equations and parameter estimation procedures, is described in Sect. 2.

Author contributions

Roland Hohensinn (RH): Conceptualization; Methodology; Software; Formal analysis; Investigation; Data curation; Visualization; Writing – original draft; Writing – review & editing. Junyang Gou (JG): Conceptualization; Methodology; Software; Formal analysis; Investigation; Data curation; Visualization; Writing – review & editing. Ulrich Meyer (UM): Investigation; Data curation; Writing – original draft; Writing – review & editing. Vincent Humphrey (VH): Investigation; Writing – review & editing. Laura Jensen (LJ): Investigation; Writing – review & editing. Wouter Dorigo (WD): Investigation; Data curation; Writing – review & editing. Eva Boergens (EB): Investigation; Writing – review & editing. Benedikt Soja (BS): Investigation; Writing – review & editing. Alexander Gruber (AGr): Investigation; Writing – review & editing. Laura Jensen (LJ): Investigation; Writing – review & editing. Annette Eicker (AE): Investigation; Writing – review & editing. Michael Rast (MR): Investigation. Andreas Günther ntner (AGü): Investigation; Data curation; Writing – original draft; Writing – review & editing.

Competing Interests

Co-author A. Gruber is member of the editorial board of the HESS journal. In addition to this, the authors declare that they have no competing interests.

Acknowledgments

A part of this study was performed during Roland Hohensinn's scientist visits at Scripps Institution of Oceanography, UCSD, and Junyang Gou's scientific visit at Bodner Lab, MIT.

Financial support

The Global Gravity-based Groundwater Product (G3P) project received funding from the European Union's Horizon 2020 research and innovation programme under grant agreement No. 870353.

References

Ahmed, M., Wiese, D.N., 2019. Short-term trends in Africa's freshwater resources: Rates and drivers. Science of the Total Environment 695, 133843.

Akan, A., Yılmaz, M.T., Dobslaw, H., Ince, E.S., Evrendilek, F., Förste, C., Yagci, A.L., 2025. Evaluation of globally gridded precipitation data and satellite-based terrestrial water storage products using hydrological drought recovery time. Hydrology and Earth System Sciences 29, 3359–3377. doi:10.5194/hess-29-3359-2025.

Albergel, C., De Rosnay, P., Gruhier, C., Muñoz-Sabater, J., Hasenauer, S., Isaksen, L., Kerr, Y., Wagner, W., 2012. Evaluation of remotely sensed and modelled soil moisture products using global ground-based in situ observations. Remote Sensing of Environment 118, 215–226.

Allen, M.R., Tett, S.F., 1999. Checking for model consistency in optimal fingerprinting. Climate Dynamics 15, 419–434.

Amiri-Simkooei, A., Hosseini-Asl, M., Asgari, J., Zangeneh-Nejad, F., 2019. Offset detection in GPS position time series using multivariate analysis. GPS solutions 23, 1–12.

Anyah, R., Forootan, E., Awange, J.L., Khaki, M., 2018. Understanding linkages between global climate indices and terrestrial water storage changes over Africa using GRACE products. Science of The Total Environment 635, 1405–1416.

Argus, D.F., Martens, H.R., Borsa, A.A., Knappe, E., Wiese, D.N., Alam, S., Anderson, M., Khatiwada, A., Lau, N., Peidou, A., Swarr, M., White, A.M., Bos, M.S., Ellmer, M., Landerer, F.W., Gardiner, W.P., 2022. Subsurface water flux in california's central valley and its source watershed from space geodesy. Geophysical Research Letters 49, e2022GL099583. doi:10.1029/2022GL099583.

Asoka, A., Gleeson, T., Wada, Y., Mishra, V., 2017. Relative contribution of monsoon precipitation and pumping to changes in groundwater storage in India. Nature Geoscience 10, 109–117. doi:10.1038/ngeo2869.

Beltaos, S., Peters, D.L., 2024. Effects of regulation on open-water flows in the lower Peace River, Canada, and implications for the recharge of Peace-Athabasca Delta basins. River Research and Applications 40, 151–162.

Bhanja, S.N., Mukherjee, A., Rodell, M., Wada, Y., Chattopadhyay, S., Velicogna, I., Pangaluru, K., Famiglietti, J.S., 2017. Groundwater rejuvenation in parts of India influenced by water-policy change implementation. Scientific reports 7, 7453.

Bierkens, M.F., Wada, Y., 2019. Non-renewable groundwater use and groundwater depletion: a review. Environmental Research Letters 14, 063002. doi:10.1088/1748-9326/ab1a5f.

Bindoff, N.L., Stott, P.A., AchutaRao, K.M., Allen, M.R., Gillett, N., Gutzler, D., Hansingo, K., Hegerl, G., Hu, Y., Jain, S., et al., 2014. Detection and attribution of climate change: from global to regional. Climate change 2013: the physical science basis .

Boergens, E., Güntner, A., Sips, M., Schwatke, C., Dobslaw, H., 2024a. Interannual variations of terrestrial water storage in the East African Rift region. Hydrology and Earth System Sciences 28, 4733–4754. doi:10.5194/hess-28-4733-2024.

Boergens, E., Güntner, A., Sips, M., Schwatke, C., Dobslaw, H., 2024b. Interannual variations of terrestrial water storage in the east african rift region. Hydrology and Earth System Sciences 28, 4733–4754. doi:10.5194/hess-28-4733-2024.

Bonsal, B.R., Peters, D.L., Seglenieks, F., Rivera, A., Berg, A., 2019. Changes in freshwater availability across Canada. Canada's changing climate report , 261–342.

Bos, M., Fernandes, R., Bastos, L., 2021. Hector user manual version 1.9. https://segal.ubi.pt/wp-content/uploads/2021/05/hector_manual_1.9.pdf, last accessed 2024-01-19,.

Bos, M., Fernandes, R., Williams, S., Bastos, L., 2008. Fast error analysis of continuous GPS observations. Journal of Geodesy 82, 157–166.

Bos, M.S., Montillet, J.P., Williams, S.D., Fernandes, R.M., 2020. Introduction to geodetic time series analysis, in: Geodetic Time Series Analysis in Earth Sciences. Springer, pp. 29–52.

Braun, M.H., Malz, P., Sommer, C., Farías-Barahona, D., Sauter, T., Casassa, G., Soruco, A., Skvarca, P., Seehaus, T.C., 2019. Constraining glacier elevation and mass changes in South America. Nature Climate Change 9, 130–136. doi:https://doi.org/10.1038/s41558-018-0375-7.

Bring, A., Fedorova, I., Dibike, Y., Hinzman, L., Mård, J., Mernild, S.H., Prowse, T., Semenova, O., Stuefer, S.L., Woo, M.K., 2016. Arctic terrestrial hydrology: A synthesis of processes, regional effects, and research challenges. Journal of Geophysical Research: Biogeosciences 121, 621–649. doi:10.1002/2015JG003131.

Bulygina, O.N., Groisman, P.Y., Razuvaev, V.N., Korshunova, N.N., 2011a. Changes in snow cover characteristics over Northern Eurasia since 1966. Environmental Research Letters 6, 045204. doi:10.1088/1748-9326/6/4/045204.

Bulygina, O.N., Groisman, P.Y., Razuvaev, V.N., Korshunova, N.N., 2011b. Changes in snow cover characteristics over northern eurasia since 1966. Environmental Research Letters 6, 045204. doi:10.1088/1748-9326/6/4/045204.

Cao, G., Zheng, C., Scanlon, B.R., Liu, J., Li, W., 2013. Use of flow modeling to assess sustainability of groundwater resources in the North China Plain. Water Resources Research 49, 159–175. doi:https://doi.org/10.1029/2012WR011899.

Chandanpurkar, H.A., Famiglietti, J.S., Gopalan, K., Wiese, D.N., Wada, Y., Kakinuma, K., Reager, J.T., Zhang, F., 2025. Unprecedented continental drying, shrinking freshwater availability, and increasing land contributions to sea level rise. Science Advances 11, eadx0298.

Chandanpurkar, H.A., Fasullo, J.T., Reager, J.T., Hamlington, B.D., 2021. A note on spectral representation of cyclostationary GRACE-TWS signals. Geophysical Research Letters 48, e2021GL093278. doi:10.1029/2021GL093278.

Chaudhari, S., Pokhrel, Y., Moran, E., Miguez-Macho, G., 2019. Multi-decadal hydrologic change and variability in the Amazon River basin: understanding terrestrial water storage variations and drought characteristics. Hydrology and Earth System Sciences 23, 2841–2862.

Chen, J., Wilson, C., Tapley, B., 2006. Satellite gravity measurements confirm accelerated melting of Greenland ice sheet. science 313, 1958–1960. doi:https://doi.org/10.1126/science.1129007.

Chen, J., Wilson, C., Tapley, B., Longuevergne, L., Yang, Z., Scanlon, B., 2010. Recent La Plata basin drought conditions observed by satellite gravimetry. Journal of Geophysical Research: Atmospheres 115.

Chen, J.L., Pekker, T., Wilson, C.R., Tapley, B.D., Kostianoy, A.G., Crétaux, J.F., Safarov, E.S., 2017. Long-term Caspian Sea level change. Geophysical Research Letters 44, 6993–7001. doi:10.1002/2017GL073958.

Cheon, S.H., Hamlington, B.D., Reager, J.T., Chandanpurkar, H.A., 2021. Identifying ENSO-related interannual and decadal variability on terrestrial water storage. Scientific Reports 11, 13595. doi:10.1038/s41598-021-92729-4.

Choulga, M., Moschini, F., Mazzetti, C., Grimaldi, S., Disperati, J., Beck, H., Salamon, P., Prudhomme, C., 2024. Technical note: Surface fields for global environmental modelling. Hydrology and Earth System Sciences 28, 2991–3036. doi:10.5194/hess-28-2991-2024.

Ciracì, E., Velicogna, I., Swenson, S., 2020. Continuity of the mass loss of the world's glaciers and ice caps from the GRACE and GRACE follow-on missions. Geophysical Research Letters 47, e2019GL086926.

Cook, B.I., Mankin, J.S., Marvel, K., Williams, A.P., Smerdon, J.E., Anchukaitis, K.J., 2020. Twenty-first century drought projections in the CMIP6 forcing scenarios. Earth's Future 8, e2019EF001461. doi:10.1029/2019EF001461.

Cui, L., Zhu, C., Wu, Y., Yao, C., Wang, X., An, J., Wei, P., 2022. Natural-and human-induced influences on terrestrial water storage change in Sichuan, Southwest China from 2003 to 2020. Remote Sensing 14, 1369.

Dahle, C., Boergens, E., Sasgen, I., Döhne, T., Reißland, S., Dobslaw, H., Klemann, V., Murböck, M., König, R., Dill, R., Sips, M., Sylla, U., Groh, A., Horwath, M., Flechtner, F., 2025. GravIS: Mass anomaly products from satellite gravimetry. Earth System Science Data 17, 611–631. doi:10.5194/essd-17-611-2025.

Dangar, S., Asoka, A., Mishra, V., 2021. Causes and implications of groundwater depletion in India: A review. Journal of Hydrology 596, 126103. doi:https://doi.org/10.1016/j.jhydrol.2021.126103.

Döll, P., Müller Schmied, H., Schuh, C., Portmann, F.T., Eicker, A., 2014. Global-scale assessment of groundwater depletion and related groundwater abstractions: Combining hydrological modeling with information from well observations and GRACE satellites. Water Resources Research 50, 5698–5720. doi:10.1002/2014WR015595.

Dorigo, W., Dietrich, S., Aires, F., Brocca, L., Carter, S., Cretaux, J.F., Dunkerley, D., Enomoto, H., Forsberg, R., Güntner, A., et al., 2021. Closing the water cycle from observations across scales: Where do we stand? Bulletin of the American Meteorological Society 102, E1897–E1935.

Dubois, E., Larocque, M., Gagné, S., Braun, M., 2022. Climate change impacts on groundwater recharge in cold and humid climates: Controlling processes and thresholds. Climate 10, 6.

Dussaillant, I., Bannwart, J., Paul, F., Zemp, M., 2023. Glacier mass change global gridded data from 1976 to present derived from the fluctuations of glaciers database. world glacier monitoring service. doi:10.24381/cds.ba597449.

Eicker, A., Schawohl, L., Middendorf, K., Bagge, M., Jensen, L., Dobslaw, H., 2024. Influence of GIA uncertainty on climate model evaluation with GRACE/GRACE-FO satellite gravimetry data. Journal of Geophysical Research: Solid Earth 129, e2023JB027769.

Famiglietti, J.S., Lo, M., Ho, S.L., Bethune, J., Anderson, K., Syed, T.H., Swenson, S.C., de Linage, C.R., Rodell, M., 2011. Satellites measure recent rates of groundwater depletion in California's Central Valley. Geophysical Research Letters 38. doi:https://doi.org/10.1029/2010GL046442.

Fatolazadeh, F., Goïta, K., 2021. Mapping terrestrial water storage changes in Canada using GRACE and GRACE-FO. Science of The Total Environment 779, 146435. doi:10.1016/j.scitotenv.2021.146435.

Favreau, G., Cappelaere, B., Massuel, S., Leblanc, M., Boucher, M., Boulain, N., Leduc, C., 2009. Land clearing, climate variability, and water resources increase in semiarid southwest Niger: A review. Water Resources Research 45.

Felfelani, F., Wada, Y., Longuevergne, L., Pokhrel, Y.N., 2017. Natural and human-induced terrestrial water storage change: A global analysis using hydrological models and GRACE. Journal of Hydrology 553, 105–118.

Feng, W., Zhong, M., Lemoine, J.M., Biancale, R., Hsu, H.T., Xia, J., 2013. Evaluation of groundwater depletion in North China using the Gravity Recovery and Climate Experiment (GRACE) data and ground-based measurements. Water Resources Research 49, 2110–2118. doi:10.1002/wrcr.20192.

Franzke, C., 2012. Nonlinear trends, long-range dependence, and climate noise properties of surface temperature. Journal of Climate 25, 4172–4183.

Franzke, C.L., O'Kane, T.J., 2017. Nonlinear and stochastic climate dynamics. Cambridge University Press.

Frappart, F., 2020. Groundwater storage changes in the major north african transboundary aquifer systems during the GRACE era (2003–2016). Water 12, 2669.

Frappart, F., Ramillien, G., 2018. Monitoring groundwater storage changes using the gravity recovery and climate experiment (GRACE) satellite mission: A review. Remote Sensing 10. doi:10.3390/rs10060829.

Fraser, R.H., Kokelj, S.V., Lantz, T.C., McFarlane-Winchester, M., Olthof, I., Lacelle, D., 2018. Climate sensitivity of high Arctic permafrost terrain demonstrated by widespread ice-wedge thermokarst on Banks Island. Remote Sensing 10, 954. doi:10.3390/rs10060954.

Frederikse, T., Landerer, F., Caron, L., Adhikari, S., Parkes, D., Humphrey, V.W., Dangendorf, S., Hogarth, P., Zanna, L., Cheng, L., et al., 2020. The causes of sea-level rise since 1900. Nature 584, 393–397. doi:https://doi.org/10.1038/s41586-020-2591-3.

Gafurov, A., Selyuzhenok, V., Latinovic, M., Apel, H., Mamaraimov, A., Salokhiddinov, A., Boergens, E., Güntner, A., 2024. GRACE observes the natural and irrigation-induced regional redistribution of water storage in central asia. Journal of Hydrology: Regional Studies 56, 101994. doi:10.1016/j.ejrh.2024.101994.

Gardner, A.S., Moholdt, G., Wouters, B., Wolken, G.J., Burgess, D.O., Sharp, M.J., Cogley, J.G., Braun, C., Labine, C., 2011. Sharply increased mass loss from glaciers and ice caps in the Canadian Arctic Archipelago. Nature 473, 357–360. doi:10.1038/nature10089.

Gbetkom, P.G., Crétaux, J.F., Biancamaria, S., Blazquez, A., Paris, A., Tchilibou, M., Gal, L., Kitambo, B., Oliveira, R.A.J., Gosset, M., 2024. Lake Tanganyika basin water storage variations from 2003–2021 for water balance and flood monitoring. Remote Sensing Applications: Society and Environment 34, 101182.

Gobron, K., Hohensinn, R., Loizeau, X., Bulgin, C.E., Merchant, C.J., Woolliams, E.R., Cox, M.G., Dorigo, W., Howard, T., Langsdale, M., Povey, A.C., Ablain, M., Bogusz, J., Gruber, A., Klos, A., Mittaz, J., 2026. A unified framework for trend uncertainty assessment in climate data records: Demonstration on global mean sea level. Surveys in Geophysics doi:10.1007/s10712-025-09922-7.

Gobron, K., Rebischung, P., de Viron, O., Demoulin, A., Van Camp, M., 2022. Impact of offsets on assessing the low-frequency stochastic properties of geodetic time series. Journal of Geodesy 96, 46.

Goncalves, J., Petersen, J., Deschamps, P., Hamelin, B., Baba-Sy, O., 2013. Quantifying the modern recharge of the "fossil" Sahara aquifers. Geophysical Research Letters 40, 2673–2678.

Gong, H., Pan, Y., Zheng, L., Li, X., Zhu, L., Zhang, C., Huang, Z., Li, Z., Wang, H., Zhou, C., 2018. Long-term groundwater storage changes and land subsidence development in the North China Plain (1971–2015). Hydrogeology Journal 26, 1417–1427.

Gonzales, L., López, V., Huamán, D., Villalobos, C., Espinoza, R., Vega, M., Ramos, J., 2025. Two decades of groundwater variability in Peru using satellite gravimetry data. Applied Sciences 15, 8071. doi:10.3390/app15148071. published 20 July 2025.

Gou, J., Börger, L., Schindelegger, M., Soja, B., 2025. Downscaling GRACE-derived ocean bottom pressure anomalies using self-supervised data fusion. Journal of Geodesy 99, 19. doi:https://doi.org/10.1007/s00190-025-01943-9.

Gou, J., Soja, B., 2024. Global high-resolution total water storage anomalies from self-supervised data assimilation using deep learning algorithms. Nature Water 2, 139–150. doi:10.1038/s44221-024-00194-w.

de Graaf, I.E., van Beek, R.L., Gleeson, T., Moosdorf, N., Schmitz, O., Sutanudjaja, E.H., Bierkens, M.F., 2017. A global-scale two-layer transient groundwater model: Development and application to groundwater depletion. Advances in water Resources 102, 53–67.

Gronewold, A.D., Rood, R.B., 2019. Recent water level changes across Earth's largest lake system and implications for future variability. Journal of Great Lakes Research 45, 1–3. doi:https://doi.org/10.1016/j.jglr.2018.10.012.

Gunes, O., Aydin, C., 2024. Colored noise in GRACE total water storage time series: Its impact on trend significance in the Türkiye region and major world river basins. Advances in Space Research 74, 1633–1647. doi:https://doi.org/10.1016/j.asr.2024.05.051.

Güntner, A., Sharifi, E., Haas, J., Boergens, E., Cao, F., Dahle, C., Darbeheshti, N., Dobslaw, H., Dussaillant, I., Dorigo, W., Flechtner, F., Jäggi, A., Kosmale, M., Lasser, M., Luojus, K., Meyer, U., Pasik, A., Preimersberger, W., Ruz Vargas, C., Zemp, M., 2026. The global gravity-based groundwater product (G3P). Earth System Science Data Discussions doi:10.5194/essd-2025-797. preprint, in review.

Güntner, A., Sharifi, E., Haas, J., Boergens, E., Dahle, C., Dobslaw, H., Dorigo, W., Dussailant, I., Flechtner, F., Jäggi, A., Kosmale, M., Luojus, K., Mayer-Gürr, T., Meyer, U., Preimesberger, W., Ruz Vargas, C., Zemp, M., 2024. Global Gravity-based Groundwater Product (G3P) V.1.12. GFZ Data Services doi:10.5880/g3p.2024.001.

Haacker, E.M., Kendall, A.D., Hyndman, D.W., 2016. Water level declines in the High Plains Aquifer: Predevelopment to resource senescence. Groundwater 54, 231–242. doi:https://doi.org/10.1111/gwat.12350.

Hamdi, M., Goïta, K., 2023. Analysis of groundwater depletion in the saskatchewan river basin in Canada from coupled SWAT-MODFLOW and satellite gravimetry. Hydrology 10, 188.

Hamlington, B.D., Reager, J.T., Chandanpurkar, H.A., Kim, K.Y., 2019. Amplitude modulation of seasonal variability in terrestrial water storage. Geophysical Research Letters 46, 4404–4412. doi:10.1029/2019GL082272.

Hasselmann, K., 1997. Multi-pattern fingerprint method for detection and attribution of climate change. Climate dynamics 13, 601–611.

Hernández, A., García-Sanz, I., Heine-Fuster, I., Luque, J.A., Aránguiz-Acuña, A., Parra, P., Pedreros-Guarda, P., Pérez-Martínez, C., 2021. Limnological response from high-altitude wetlands to the water supply in the Andean Altiplano. Scientific Reports 11, 7681. doi:10.1038/s41598-021-87162-6.

Hirschi, M., Stradiotti, P., Crezee, B., Dorigo, W., Seneviratne, S.I., 2025. Potential of long-term satellite observations and reanalysis products for characterising soil drying: trends and drought events. Hydrology and Earth System Sciences 29, 397–425.

Hoell, A., Gaughan, A.E., Shukla, S., Magadzire, T., 2017. The hydrologic effects of synchronous El Niño–Southern oscillation and subtropical Indian ocean dipole events over Southern Africa. Journal of Hydrometeorology 18, 2407–2424.

Hohensinn, R., Ruttner, P., Bock, Y., 2024. Sensitivity of GNSS to vertical land motion over Europe: effects of geophysical loadings and common-mode errors. Journal of Geodesy 98, 68.

Huang, J., Halpenny, J., Van Der Wal, W., Klatt, C., James, T., Rivera, A., 2012. Detectability of groundwater storage change within the great lakes water basin using GRACE. Journal of Geophysical Research: Solid Earth 117.

Huang, Q., Wang, P., Wang, R., Yu, J., Frolova, N.L., Pozdniakov, S.P., 2025. Differential decline in terrestrial water storage across major permafrost-dominated Arctic River basins during the rapid warming period from 1981 to 2020. Journal of Geophysical Research: Atmospheres 130, e2024JD042978.

Huggins, X., Gleeson, T., Kummu, M., Zipper, S.C., Wada, Y., Troy, T.J., Famiglietti, J.S., 2022. Hotspots for social and ecological impacts from freshwater stress and storage loss. Nature Communications 13, 439.

Humphrey, V., Gudmundsson, L., 2019. GRACE-REC: a reconstruction of climate-driven water storage changes over the last century. Earth System Science Data 11, 1153–1170. doi:https://doi.org/10.5194/essd-11-1153-2019.

Humphrey, V., Gudmundsson, L., Seneviratne, S.I., 2016. Assessing global water storage variability from GRACE: Trends, seasonal cycle, subseasonal anomalies and extremes. Surveys in geophysics 37, 357–395. doi:https://doi.org/10.1007/s10712-016-9367-1.

Humphrey, V., Gudmundsson, L., Seneviratne, S.I., 2017. A global reconstruction of climate-driven subdecadal water storage variability. Geophysical Research Letters 44, 2300–2309. doi:10.1002/2017GL072564.

Humphrey, V., Rodell, M., Eicker, A., 2023. Using satellite-based terrestrial water storage data: a review. Surveys in Geophysics 44, 1489–1517.

Jackson, C.R., Bloomfield, J.P., Mackay, J.D., 2015. Evidence for changes in historic and future groundwater levels in the UK. Progress in Physical Geography 39, 49–67.

Jacob, T., Wahr, J., Pfeffer, W.T., Swenson, S., 2012. Recent contributions of glaciers and ice caps to sea level rise. Nature 482, 514–518.

Jäggi, A., Meyer, U., Lasser, M., Jenny, B., Lopez, T., Flechtner, F., Dahle, C., Förste, C., Mayer-Gürr, T., Kvas, A., Lemoine, J.M., Bourgogne, S., Weigelt, M., Groh, A., 2020. International combination service for time-variable gravity fields (COST-G) - start of operational phase and future perspectives. International Association of Geodesy Symposia 152, 57–65. doi:10.1007/1345_2020_109.

Jarugula, S., McPhaden, M.J., 2023. Indian ocean dipole affects eastern tropical Atlantic salinity through Congo River Basin hydrology. Communications Earth & Environment 4, 366.

Jasechko, S., Seybold, H., Perrone, D., Fan, Y., Shamsudduha, M., Taylor, R.G., Fallatah, O., Kirchner, J.W., 2024. Rapid groundwater decline and some cases of recovery in aquifers globally. Nature 625, 715–721.

Jensen, L., Eicker, A., Dobslaw, H., Pail, R., 2020. Emerging changes in terrestrial water storage variability as a target for future satellite gravity missions. Remote Sensing 12, 3898. doi:10.3390/rs12233898.

Jensen, L., Eicker, A., Dobslaw, H., Stacke, T., Humphrey, V., 2019. Long-term wetting and drying trends in land water storage derived from GRACE and CMIP5 models. Journal of Geophysical Research: Atmospheres 124, 9808–9823.

Jiang, Y., Zhou, L., Roundy, P.E., Hua, W., Raghavendra, A., 2021. Increasing influence of Indian Ocean dipole on precipitation over central equatorial Africa. Geophysical Research Letters 48, e2020GL092370.

Joodaki, G., Wahr, J., Swenson, S., 2014. Estimating the human contribution to groundwater depletion in the Middle East, from GRACE data, land surface models, and well observations. Water Resources Research 50, 2679–2692.

Kayastha, M.B., Ye, X., Huang, C., Xue, P., 2022. Future rise of the Great Lakes water levels under climate change. Journal of Hydrology 612, 128205. doi:10.1016/j.jhydrol.2022.128205.

Kirshen, A.B., Moran, B.J., Munk, L.A., Russo, A.A., McKnight, S.V., Jenckes, J., Corkran, D.B., Bresee, M., Boutt, D.F., 2025. Freshwater inflows to closed basins of the Andean plateau in Chile, Argentina, and Bolivia. Communications Earth & Environment 6, 177.

Klos, A., Hunegnaw, A., Teferle, F.N., Abraha, K.E., Ahmed, F., Bogusz, J., 2018. Statistical significance of trends in zenith wet delay from re-processed GPS solutions. GPS Solutions 22, 51.

Knief, U., Forstmeier, W., 2021. Violating the normality assumption may be the lesser of two evils. Behavior Research Methods 53, 2576–2590.

Konikow, L.F., 2015. Long-term groundwater depletion in the United States. Groundwater 53, 2–9. doi:https://doi.org/10.1111/gwat.12306.

Koscielny-Bunde, E., Kantelhardt, J.W., Braun, P., Bunde, A., Havlin, S., 2006. Long-term persistence and multifractality of river runoff records: Detrended fluctuation studies. Journal of Hydrology 322, 120–137. doi:10.1016/j.jhydrol.2005.03.004.

Koutsoyiannis, D., 2003. Climate change, the hurst phenomenon, and hydrological statistics. Hydrological Sciences Journal 48, 3–24.

Kvas, A., Boergens, E., Dobslaw, H., Eicker, A., Mayer-Guerr, T., Güntner, A., 2024. Evaluating long-term water storage trends in small catchments and aquifers from a joint inversion of 20 years of GRACE/GRACE-FO mission data. Geophysical Journal International 236, 1002–1012.

Lai, E.N., Wang-Erlandsson, L., Virkki, V., Porkka, M., Van Der Ent, R.J., 2023. Root zone soil moisture in over 25% of global land permanently beyond pre-industrial variability as early as 2050 without climate policy. Hydrology and Earth System Sciences 27, 3999–4018.

Landerer, F.W., Flechtner, F.M., Save, H., Webb, F.H., Bandikova, T., Bertiger, W.I., Bettadpur, S.V., Byun, S.H., Dahle, C., Dobslaw, H., et al., 2020. Extending the global mass change data record: GRACE follow-on instrument and science data performance. Geophysical Research Letters 47, e2020GL088306.

Leduc, C., Favreau, G., Schroeter, P., 2001. Long-term rise in a Sahelian water-table: The continental terminal in south-west Niger. Journal of hydrology 243, 43–54.

Lewkowicz, A.G., Way, R.G., 2019. Extremes of summer climate trigger thousands of thermokarst landslides in a high Arctic environment. Nature Communications 10, 1329. doi:10.1038/s41467-019-09314-7.

Li, B., Rodell, M., 2024. Terrestrial water storage in 2023. Nature Reviews Earth & Environment 5, 247–249.

Li, J., Wang, S., 2022. Seasonal variations and long-term trends of groundwater over the Canadian landmass. Hydrogeology Journal 30, 401–415. doi:10.1007/s10040-022-02460-1.

Li, J., Wang, S., Zhou, F., 2016. Time series analysis of long-term terrestrial water storage over Canada from GRACE satellites using principal component analysis. Canadian Journal of Remote Sensing 42, 161–170. doi:10.1080/07038992.2016.1166042.

Li, Z., Zhang, Y.K., 2007. Quantifying fractal dynamics of groundwater systems with detrended fluctuation analysis. Journal of hydrology 336, 139–146.

Lin, H., Cheng, X., Zheng, L., Peng, X., Feng, W., Peng, F., 2022. Recent changes in groundwater and surface water in large pan-arctic river basins. Remote Sensing 14, 607.

Little, M.A., Bloomfield, J.P., 2010. Robust evidence for random fractal scaling of groundwater levels in unconfined aquifers. Journal of hydrology 393, 362–369.

Lu, J., Kong, D., Zhang, Y., Xie, Y., Gu, X., Gulakhmadov, A., 2025. Hotspots of global water resource changes and their causes. Earth's Future 13, e2024EF005461. doi:https://doi.org/10.1029/2024EF005461.

Lucas, M.C., Kublik, N., Rodrigues, D.B.B., Meira Neto, A.A., Almagro, A., de Melo, D.C.D., Zipper, S.C., de Oliveira, P.T.S., 2021. Significant baseflow reduction in the São Francisco River Basin. Water 13. doi:10.3390/w13010002. published 22 December 2020.

Luojus, K., Pulliainen, J., Takala, M., Lemmetyinen, J., Mortimer, C., Derksen, C., Mudryk, L., Moisander, M., Hiltunen, M., Smolander, T., Ikonen, J., Cohen, J., Salminen, M., Norberg, J., Veijola, K., Venäläinen, P., 2021. GlobSnow v3.0 northern hemisphere snow water equivalent dataset. Scientific Data 8. doi:10.1038/s41597-021-00939-2.

MacDonald, A.M., Bonsor, H.C., Dochartaigh, B.É.Ó., Taylor, R.G., 2012. Quantitative maps of groundwater resources in Africa. Environmental Research Letters 7, 024009. doi:https://doi.org/10.1088/1748-9326/7/2/024009.

MacQueen, J., 1967. Some methods for classification and analysis of multivariate observations, in: Proceedings of the Fifth Berkeley Symposium on Mathematical Statistics and Probability, Volume 1: Statistics, University of California press. pp. 281–298.

Mandelbrot, B.B., Wallis, J.R., 1969. Some long-run properties of geophysical records. Water resources research 5, 321–340.

de Melo, D.C.D., Wendland, E., 2020. Using GRACE to quantify the depletion of terrestrial water storage in northeastern Brazil: The Urucuia aquifer system. Science of The Total Environment 705, 135828. doi:10.1016/j.scitotenv.2019.135828.

Merchant, C.J., Paul, F., Popp, T., Ablain, M., Bontemps, S., Defourny, P., Hollmann, R., Lavergne, T., Laeng, A., De Leeuw, G., et al., 2017. Uncertainty information in climate data records from Earth observation. Earth System Science Data 9, 511–527.

Merchant, C.J., Woolliams, E.R., Dorigo, W., Bulgin, C.E., Gobron, K., Hohensinn, R., Loizeau, X., Tynan, C.P., 2026. Stability specifications for climate data records: their meaning and application in evaluating geophysical trend uncertainty. Surveys in Geophysics , 1–16.

Meyer, U., Lasser, M., Dahle, C., Förste, C., Behzadpour, S., Koch, Jäggi, A., 2024. Combined monthly GRACE-FO gravity fields for a global gravity-based groundwater product. Geophysical Journal International 236, 456–469. doi:10.1093/gji/ggad437.

Micklin, P., 2016. The future Aral Sea: hope and despair. Journal of Environmental Geography 9, 1–15. doi:10.1515/jengeo-2016-0001.

Moihamette, F., Pokam, W.M., Diallo, I., Washington, R., 2024. Response of regional circulation features to the Indian Ocean dipole and influence on Central Africa climate. Climate Dynamics 62, 1–21.

Montillet, J.P., Bos, M.S., 2019. Geodetic time series analysis in earth sciences. Springer.

Mudelsee, M., 2010. Climate Time Series Analysis: Classical Statistical and Bootstrap Methods. Springer, Dordrecht, Netherlands. doi:10.1007/978-90-481-9482-7.

Mudelsee, M., 2019. Trend analysis of climate time series: A review of methods. Earth-Science Reviews 190, 310–322. URL: https://www.sciencedirect.com/science/article/pii/S0012825218303726, doi:https://doi.org/10.1016/j.earscirev.2018.12.005.

Muskett, R.R., Romanovsky, V.E., 2011. Alaskan permafrost groundwater storage changes derived from GRACE and ground measurements. Remote Sensing 3, 378–397. doi:10.3390/rs3020378.

Naumann, G., Cammalleri, C., Mentaschi, L., Vogt, J., 2022. Extreme and Long-Term Drought in the La Plata Basin: Event Evolution and Impact Assessment until September 2022. Technical Report JRC132245. Joint Research Centre (JRC), European Commission. Luxembourg. URL: https://publications.jrc.ec.europa.eu/repository/handle/JRC132245.

Ni, S., Chen, J., Wilson, C.R., Li, J., Hu, X., Fu, R., 2018. Global terrestrial water storage changes and connections to ENSO events. Surveys in Geophysics 39, 1–22.

Nikraftar, Z., Parizi, E., Saber, M., Hosseini, S.M., Ataie-Ashtiani, B., Simmons, C.T., 2024. Groundwater sustainability assessment in the Middle East using GRACE/GRACE-FO data. Hydrogeology Journal 32, 321–337.

Noël, B., van de Berg, W.J., Machguth, H., Lhermitte, S., Howat, I., Fettweis, X., van den Broeke, M.R., 2018. Six decades of glacial mass loss in the Canadian Arctic Archipelago. Journal of Geophysical Research: Earth Surface 123, 1430–1449. doi:10.1029/2017JF004304.

Orth, R., Seneviratne, S.I., 2012. Analysis of soil moisture memory from observations in europe. Journal of Geophysical Research: Atmospheres 117, D15115. doi:10.1029/2011JD017366.

Orth, R., Staudinger, M., Seneviratne, S.I., 2013. Inferring soil moisture memory from streamflow observations using a simple water balance model. Journal of Hydrometeorology 14, 1773–1790. doi:10.1175/JHM-D-12-099.1.

Otosaka, I.N., Shepherd, A., Ivins, E.R., Schlegel, N.J., Amory, C., van den Broeke, M.R., Horwath, M., Joughin, I., King, M.D., Krinner, G., et al., 2023. Mass balance of the greenland and antarctic ice sheets from 1992 to 2020. Earth System Science Data 15, 1597–1616. doi:10.5194/essd-15-1597-2023.

Pasik, A., Gruber, A., Preimesberger, W., De Santis, D., Dorigo, W., 2023. Uncertainty estimation for a new exponential-filter-based long-term root-zone soil moisture dataset from Copernicus Climate Change Service (C3S) surface observations. Geoscientific Model Development 16, 4957–4976. doi:10.5194/gmd-16-4957-2023.

Patterson, H.D., Thompson, R., 1971. Recovery of inter-block information when block sizes are unequal. Biometrika 58, 545–554.

Pfeffer, J., Cazenave, A., Barnoud, A., 2022. Analysis of the interannual variability in satellite gravity solutions: detection of climate modes fingerprints in water mass displacements across continents and oceans. Climate Dynamics 58, 1065–1084.

Piao, S., Wang, X., Park, T., Chen, C., Lian, X., He, Y., Bjerke, J.W., Chen, A., Ciais, P., Tømmervik, H., Nemani, R.R., Myneni, R.B., 2020. Characteristics, drivers and feedbacks of global greening. Nature Reviews Earth & Environment 1, 14–27. doi:10.1038/s43017-019-0001-x.

Pokhrel, Y., Felfelani, F., Satoh, Y., Boulange, J., Burek, P., Gädeke, A., Gerten, D., Gosling, S.N., Grillakis, M., Gudmundsson, L., et al., 2021. Global terrestrial water storage and drought severity under climate change. Nature Climate Change 11, 226–233. doi:https://doi.org/10.1038/s41558-020-00972-w.

Preimesberger, W., Stradiotti, P., Dorigo, W., 2025. ESA CCI soil moisture gapfilled: an independent global gap-free satellite climate data record with uncertainty estimates. Earth System Science Data 17, 4305–4329.

Richey, A.S., Thomas, B.F., Lo, M.H., Reager, J.T., Famiglietti, J.S., Voss, K., Swenson, S., Rodell, M., 2015. Quantifying renewable groundwater stress with GRACE. Water Resources Research 51, 5217–5238. doi:10.1002/2015WR017349.

Riva, R.E., Bamber, J.L., Lavallée, D.A., Wouters, B., 2010. Sea-level fingerprint of continental water and ice mass change from GRACE. Geophysical Research Letters 37. doi:https://doi.org/10.1029/2010GL044770.

Rodell, M., Famiglietti, J.S., Wiese, D.N., Reager, J., Beaudoing, H.K., Landerer, F.W., Lo, M.H., 2018. Emerging trends in global freshwater availability. Nature 557, 651–659.

Rodell, M., Velicogna, I., Famiglietti, J.S., 2009. Satellite-based estimates of groundwater depletion in India. Nature 460, 999–1002. doi:https://doi.org/10.1038/nature08238.

Roe, G.H., 2011. What do glaciers tell us about climate variability and climate change? Journal of Glaciology 57, 567–578. doi:10.3189/002214311796905640.

Saito, Y.K., Justino, F., Gurjão, C.D., Zita, L., Paixão, P., Ramiro, Í., 2025. Soil moisture dynamics in South America: A multi-dataset analysis from 1990 to 2020. International Journal of Climatology , e70047.

Satizábal-Alarcón, D.A., Suhogusoff, A., Ferrari, L.C., 2024. Characterization of groundwater storage changes in the Amazon river basin based on downscaling of GRACE/GRACE-FO data with machine learning models. Science of The Total Environment 912, 168958.

Scanlon, B.R., Faunt, C.C., Longuevergne, L., Reedy, R.C., Alley, W.M., McGuire, V.L., McMahon, P.B., 2012. Groundwater depletion and sustainability of irrigation in the US High Plains and Central Valley. Proceedings of the national academy of sciences 109, 9320–9325. doi:https://doi.org/10.1073/pnas.1200311109.

Scanlon, B.R., Zhang, Z., Save, H., Sun, A.Y., Müller Schmied, H., Van Beek, L.P., Wiese, D.N., Wada, Y., Long, D., Reedy, R.C., et al., 2018. Global models underestimate large decadal declining and rising water storage trends relative to GRACE satellite data. Proceedings of the National Academy of Sciences 115, E1080–E1089. doi:https://doi.org/10.1073/pnas.1704665115.

Scanlon, B.R., Zhang, Z., Save, H., Wiese, D.N., Landerer, F.W., Long, D., Longuevergne, L., Chen, J., 2016. Global evaluation of new GRACE mascon products for hydrologic applications. Water Resources Research 52, 9412–9429. doi:https://doi.org/10.1002/2016WR019494.

Schilling, J., Hertig, E., Tramblay, Y., Scheffran, J., 2020. Climate change vulnerability, water resources and social implications in North Africa. Regional Environmental Change 20, 15.

Seo, K.W., Ryu, D., Jeon, T., Youm, K., Kim, J.S., Oh, E.H., Chen, J., Famiglietti, J.S., Wilson, C.R., 2025. Abrupt sea level rise and Earth's gradual pole shift reveal permanent hydrological regime changes in the 21st century. Science 387, 1408–1413. doi:https://doi.org/10.1126/science.adq6529.

Shahgedanova, M., Afzal, M., Hagg, W., Kapitsa, V., Kasatkin, N., Mayr, E., Rybak, O., Saidaliyeva, Z., Severskiy, I., Usmanova, Z., Wade, A., Yaitskaya, N., Zhumabayev, D., 2020. Emptying water towers? Impacts of future climate and glacier change on river discharge in the Northern Tien Shan, Central Asia. Water 12, 627. doi:10.3390/w12030627.

Shalby, A., Emara, S.R., Metwally, M.I., Armanuos, A.M., El-Agha, D.E., Negm, A.M., Gado, T.A., 2023. Satellite-based estimates of groundwater storage depletion over Egypt. Environmental Monitoring and Assessment 195, 594.

Sharifi, E., Haas, J., Boergens, E., Dobslaw, H., Güntner, A., 2025. GRACE-compatible filtering of water storage data sets via spatial autocorrelation analysis. Hydrology and Earth System Sciences 29, 6985–6998.

Shrestha, R.R., Dibike, Y.B., Prowse, T.D., 2012. Modelling of climate-induced hydrologic changes in the lake winnipeg watershed. Journal of Great Lakes Research 38, 83–94.

Singh, A., Seitz, F., Schwatke, C., 2012. Inter-annual water storage changes in the Aral Sea from multi-mission satellite altimetry, optical remote sensing, and GRACE satellite gravimetry. Remote Sensing of Environment 123, 187–195. doi:10.1016/j.rse.2012.01.001.

Sospedra-Alfonso, R., Merryfield, W.J., Kharin, V.V., 2016. Representation of snow in the Canadian seasonal to interannual prediction system. part ii: Potential predictability and hindcast skill. Journal of Hydrometeorology 17, 2511–2535. doi:10.1175/JHM-D-16-0027.1.

Spinoni, J., Naumann, G., Carrao, H., Barbosa, P., Vogt, J., et al., 2014. World drought frequency, duration, and severity for 1951–2010. Int. J. Climatol 34, 2792–2804.

Spinoni, J., Naumann, G., Vogt, J., Barbosa, P., 2016. Meteorological droughts in Europe: events and impacts-past trends and future projections. Publications Office of the European Union.

Springer, A., Lopez, T., Owor, M., Frappart, F., Stieglitz, T., 2023. The role of space-based observations for groundwater resource monitoring over Africa. Surveys in Geophysics 44, 123–172. doi:https://doi.org/10.1007/s10712-022-09759-4.

Steffen, H., Petrovic, S., Müller, J., Schmidt, R., Wünsch, J., Barthelmes, F., Kusche, J., 2009. Significance of secular trends of mass variations determined from GRACE solutions. Journal of Geodynamics 48, 157–165. URL: https://www.sciencedirect.com/science/article/pii/S0264370709000969, doi:https://doi.org/10.1016/j.jog.2009.09.029. new Challenges in Earth's Dynamics - Proceedings of the 16th International Symposium on Earth Tides.

Tang, J., Cheng, H., Liu, L., 2014. Assessing the recent droughts in southwestern China using satellite gravimetry. Water Resources Research 50, 3030–3038.

Tangdamrongsub, N., Steele-Dunne, S.C., Gunter, B.C., Ditmar, P.G., Sutanudjaja, E.H., Sun, Y., Xia, T., Wang, Z., 2017. Improving estimates of water resources in a semi-arid region by assimilating GRACE data into the PCR-GLOBWB hydrological model. Hydrology and Earth System Sciences 21, 2053–2074.

Tapley, B.D., Bettadpur, S., Ries, J.C., Thompson, P.F., Watkins, M.M., 2004. GRACE measurements of mass variability in the earth system. science 305, 503–505.

Tapley, B.D., Watkins, M.M., Flechtner, F., Reigber, C., Bettadpur, S., Rodell, M., Sasgen, I., Famiglietti, J.S., Landerer, F.W., Chambers, D.P., et al., 2019. Contributions of GRACE to understanding climate change. Nature climate change 9, 358–369. doi:https://doi.org/10.1038/s41558-019-0456-2.

Thomas, B.F., Famiglietti, J.S., Landerer, F.W., Wiese, D.N., Molotch, N.P., Argus, D.F., 2017. GRACE groundwater drought index: Evaluation of California central valley groundwater drought. Remote Sensing of Environment 198, 384–392. doi:10.1016/j.rse.2017.06.026.

Thomson, D.J., 1982. Spectrum estimation and harmonic analysis. Proceedings of the IEEE 70, 1055–1096. doi:10.1109/PROC.1982.12433.

Van Der Knijff, J., Younis, J., De Roo, A., 2010. LISFLOOD: a GIS-based distributed model for river basin scale water balance and flood simulation. International Journal of Geographical Information Science 24, 189–212.

Velicogna, I., 2009. Increasing rates of ice mass loss from the greenland and antarctic ice sheets revealed by GRACE. Geophysical Research Letters 36.

Vishwakarma, B.D., Bates, P., Sneeuw, N., Westaway, R.M., Bamber, J.L., 2021. Re-assessing global water storage trends from GRACE time series. Environmental Research Letters 16, 034005. doi:https://doi.org/10.1088/1748-9326/abd4a9.

Wada, Y., van Beek, L.P., Bierkens, M.F., 2012. Nonsustainable groundwater sustaining irrigation: A global assessment. Water Resources Research 48. doi:10.1029/2011WR010562.

Wada, Y., Reager, J.T., Chao, B.F., Wang, J., Lo, M.H., Song, C., Li, Y., Gardner, A.S., 2017. Recent changes in land water storage and its contribution to sea level variations. Surveys in Geophysics 38, 131–152.

Walvoord, M.A., Voss, C.I., Wellman, T.P., 2012. Influence of permafrost distribution on groundwater flow in the context of climate-driven permafrost thaw: Example from Yukon Flats Basin, Alaska, United States. Water Resources Research 48, W07524. doi:10.1029/2011WR011595.

Wang, H., Jia, L., Steffen, H., Wu, P., Jiang, L., Hsu, H., Xiang, L., Wang, Z., Hu, B., 2013. Increased water storage in North America and Scandinavia from GRACE gravity data. Nature Geoscience 6, 38–42.

Wang, J., Song, C., Reager, J.T., Yao, F., Famiglietti, J.S., Sheng, Y., MacDonald, G.M., Brun, F., Schmied, H.M., Marston, R.A., et al., 2018. Recent global decline in endorheic basin water storages. Nature geoscience 11, 926–932.

Wang, S., Zhou, F., Fatolazadeh, F., Russell, H.A.J., Bunn, M., 2025. Accelerated water loss over canada's landmass in 2002–2024. Research Square doi:10.21203/rs.3.rs-6253460/v1. preprint.

Wang, X., de Linage, C., Famiglietti, J., Zender, C.S., 2011. Gravity Recovery and Climate Experiment (GRACE) detection of water storage changes in the Three Gorges Reservoir of China and comparison with in situ measurements. Water Resources Research 47. doi:https://doi.org/10.1029/2011WR010534.

Werth, S., White, D., Bliss, D., 2017. GRACE detected rise of groundwater in the Sahelian Niger River basin. Journal of Geophysical Research: Solid Earth 122, 10–459.

World Meteorological Organization, 2022. The 2022 GCOS ECVs Requirements. Technical Report GCOS-245. Global Climate Observing System. Geneva, Switzerland.

Wouters, B., Gardner, A.S., Moholdt, G., 2019. Global glacier mass loss during the GRACE satellite mission (2002-2016). Frontiers in earth science 7, 96.

Wright, S.N., Thompson, L.M., Olefeldt, D., Connon, R.F., Carpino, O.A., Beel, C.R., Quinton, W.L., 2022. Thaw-induced impacts on land and water in discontinuous permafrost: A review of the Taiga Plains and Taiga Shield, northwestern Canada. Earth-Science Reviews 232, 104104.

Xanke, J., Liesch, T., 2022. Quantification and possible causes of declining groundwater resources in the Euro-Mediterranean region from 2003 to 2020. Hydrogeology Journal 30, 379–400.

Yang, X., Tian, S., Feng, W., Ran, J., You, W., Jiang, Z., Gong, X., 2020. Spatio-temporal evaluation of water storage trends from hydrological models over australia using GRACE mascon solutions. Remote Sensing 12, 3578.

Yang, Y., Long, D., Guan, H., Scanlon, B.R., Simmons, C.T., Jiang, L., Xu, X., 2014. GRACE satellite observed hydrological controls on interannual and seasonal variability in surface greenness over mainland australia. Journal of Geophysical Research: Biogeosciences 119, 2245–2260.

Yao, C., Luo, Z., Wang, H., Li, Q., Zhou, H., 2016. GRACE-derived terrestrial water storage changes in the inter-basin region and its possible influencing factors: A case study of the Sichuan Basin, China. Remote Sensing 8, 444.

Zemp, M., Huss, M., Thibert, E., Eckert, N., McNabb, R., Huber, J., Barandun, M., Machguth, H., Nussbaumer, S.U., Gärtner-Roer, I., et al., 2019. Global glacier mass changes and their contributions to sea-level rise from 1961 to 2016. Nature 568, 382–386.

Zemp, M., Welty, E., 2023. Temporal downscaling of glaciological mass balance using seasonal observations. Journal of Glaciology doi:10.1017/jog.2023.66.

Zhao, K., Li, X., 2017. Estimating terrestrial water storage changes in the tarim river basin using GRACE data. Geophysical Journal International 211, 1449–1460.

Zhao, Q., Zhang, B., Yao, Y., Wu, W., Meng, G., Chen, Q., 2019. Geodetic and hydrological measurements reveal the recent acceleration of groundwater depletion in North China Plain. Journal of Hydrology 575, 1065–1072. doi:10.1016/j.jhydrol.2019.06.016.

Zhong, Y., Bai, H., Feng, W., Lu, J., Humphrey, V., 2023. Separating the precipitation- and non-precipitation-driven water storage trends in china. Water Resources Research 59, e2022WR033261.